Nanofabrication methods for improved bone implants

Maciej Domański

Ph.D. dissertation committee:

Chairman and Secretary

prof. dr. G. van der Steenhoven	University of Twente, Netherlands

Promotor

prof. dr. J.G.E. Gardeniers	University of Twente, Netherlands

Assistant promotor

dr. R. Luttge	University of Twente, Netherlands

Referent

dr. A.J.A. Winnubst	University of Twente, Netherlands

Members

prof. dr. ir. A.J. Huis in 't Veld	University of Twente, Netherlands
prof. dr. ir. J. Huskens	University of Twente, Netherlands
prof. dr. J.A. Jansen	Radboud University Nijmegen, Netherlands
prof. dr. ir. R.G.H. Lammertink	University of Twente, Netherlands

This research was supported by the Dutch Technology Foundation STW, which is part of the Netherlands Organization for Scientific Research (NWO) and partly funded by the Ministry of Economic Affairs, Agriculture and Innovation (project # 07621).

NANOFABRICATION METHODS FOR IMPROVED BONE IMPLANTS

DISSERTATION

to obtain
the degree of doctor at the University of Twente,
on the authority of the rector magnificus,
prof. dr. H. Brinksma,
on account of the decision of the graduation committee,
to be publicly defended
on Friday 2nd of September 2011 at 12.45 hrs

by

Maciej Domański

born on 10 March 1982
in Częstochowa, Poland

This dissertation has been approved by:

prof. dr. J.G.E. Gardeniers (promotor)
dr. R. Luttge (assistant promotor)
dr. A.J.A Winnubst (referent)

1.

INTRODUCTION

Abstract

In this chapter a general introduction is given into the topic of the relevance of implant surface properties for biomedical applications. The topics to be discussed are the interactions between implant and human body, which lead to osseointegration, and the implant parameters that have an influence on this phenomenon. The second part of this chapter will discuss micro- and nanopatterning methods and their implementation in recent research in the field of biomaterial surface modification.

1.1. Fundamentals of biomaterial-biosystem interactions

The introduction of implants or prostheses into a living organism causes specific reactions of the biological environment. The bio-molecules and cells together with the intrinsic properties of the used biomaterials determine the biocompatibility and longevity of implants [1-4]. Since the interaction of bio-molecules and cells with the biomaterial surface is a vital element in evaluating the suitability of a biomaterial for its intended function, every attempt towards avoiding undesired or enhancing desired responses to implants or prostheses is of utmost importance.

The successful outcome of any implantation procedure depends on the interrelationship of the various involved components [5]:

1. Biocompatibility of the implant material;
2. Macroscopic and microscopic nature of the implant surface;
3. The status of the implant bed in both health-related (non-infected) and morphological (bone quality) context;
4. The surgical technique;
5. The undisturbed healing phase;
6. The subsequent prosthetic design and long-term loading phase. This reconciles considerations of design, materials, location of implants, and anticipated loading, together with hygienic and cosmetic considerations.

Out of these components, surface modification can influence at least three, which may be applied to provide better implants. Currently used implant materials can be divided as follows, according to their performance upon implantation [6]:

a) bioinert, not bioactive implants (i.e. titanium);
b) bioactive, integrating with tissue in regeneration;
   - resorbable (e.g. polylactic acid)
   - non-resorbable (e.g. hydroxyapatite)
c) third generation - bioactive materials alleviating self-healing of the body.

1.1.1. Recognition of implant

In every case the first reaction of the organism on newly implanted material is an inflammatory reaction, which may lead either to further implantation site healing with osseointegration or to the unwanted effect of build-up of a layer of connective tissue in the surroundings of the implant (so called fibro-integration) [7,8].

If the organism accepts the implant, the osseointegration of the implant gives a strong bond between graft and bone with only a few nanometers of organic layer adjacent to the implant surface, which is an ultimately favored result of implantation surgery. The tissue integration might however be hindered by microorganisms. Biomaterial associated infections occur in 6 % of the cases [9,10] and strongly depend on implantation site. They more often occur in case of trauma revision surgery [11].

1.1.2. Cascade of reactions upon implantation

After the creation of an interface between the implant and the bone in surgery, a cascade of reactions leading to wound healing takes place [12-14]. First the surface of the implanted material is exposed to a bioliquid containing water, solvated ions and biomolecules. In the first moments after implantation, ions adsorb to the surface, and this process is followed by protein adsorption. As a next step hemostasis and clot formation takes place, followed by formation of loose connective tissue stroma which later will support rebuilding of the bone. Subsequently a process of neovascularization takes place, followed by recruitment of osteoblasts from either marrow stem cells or precursor osteoblast cells. At that moment the inflammatory response of the host's immune system is defining whether the implant is accepted or rejected, via various mediators [15,16]. When a well-vascularized connective tissue is established at the interface, osteogenesis continues by means of the action of osteoblasts, which secrete a collagenous matrix and contribute to mineralization. Finally, the matrix surrounds the osteoblasts and the so-called *woven bone* (primary bone) is

completed. The next important step of osseointegration is the transformation of woven bone into lamellar bone (secondary bone) which occurs under mechanical strain. The bone continues to remodel enhancing its stability and adaptation to the implant [17,18].

1.1.3. Importance of protein adsorption

On the surface of the implanted material both organic and inorganic constituents of the surrounding liquid rapidly adsorb both under *in vitro* and *in vivo* conditions [19]. The main driving force behind protein adsorption is secondary bond formation via hydrogen bonds, while the strength of the protein-surface bound furthermore depends on material chemistry and entropic effects. The adsorbed protein layer being built-up at the moment of implantation is an important mediator in cell adhesion. The adsorbed proteins also act as a trigger for the biological cascade, described in the previous section. The binding regions of adsorbed proteins are responsible for control of cell function via cellular membrane bound proteins and receptor groups called integrins, which are responsible for binding of the cell to surface-adsorbed proteins [20-22]. Upon adsorption on the implant surface, proteins may change their conformation, therewith exposing integrin-binding active regions. Among other discovered active regions in primary protein structure, the Arginine–glycine–aspartic acid (RGD) peptide region in protein plays a dominant role in protein-mediated cell adhesion [23,24].

Protein adsorption on biomaterial surfaces is considered to be virtually irreversible, however, since the interface between graft and body is a dynamic system in time, and its composition is constantly changing in complex biological liquids, proteins can be exchanged with sugars or with proteins of different function, the so-called Vroman effect [25]. This effect, which is known to occur for blood serum proteins adsorbing to a surface, consists in the initial adsorption of high-mobility protein, which are later replaced by proteins, which are less mobile but have a higher affinity for the surface.

1.1.4. Influence of physicochemical parameters on implant fidelity

The route in which an organism recognizes an implanted material depends on parameters like surface chemistry, charge, and wettability, adsorbed molecules, dissolution products, material porosity and roughness, the curvature of surface features [14,26,27]. Of particular interest to this thesis is modification at the nanoscale of implant surfaces, which has been shown to lead to superior properties [28].

Titanium, the material used in this work, is an important common material for dental implantations. Unique physicochemical characteristics and superb performance in contact with the bio environment have made it become the material of choice for the majority of chirurgical interventions in oral and maxillofacial surgeries. The unique characteristic of titanium is an inherent ability for osseointegration. This phenomenon can be explained by the fact that a clean titanium surface spontaneously oxidizes in air, creating a mostly amorphous TiO_2 surface layer of low inherent toxicity, which under human body conditions is close to its isoelectric point (pI~6) so that it becomes a weakly negatively charged oxide of low solubility in body liquids [29]. The low release of ions, the close-to-neutral charge and the hydrophilic oxidized surface are the main reasons for the stability of titanium as an implant material.

1.2. Response of biomoieties to surface features

Many of the biological processes occurring around an implant, like protein adsorption, cell adhesion, differentiation and proliferation, matrix production and calcification, are influenced by changes in the nanotopography of the implant. Through the introduction of surface features in the size range of common biomoieties, the surface interaction of the latter can be altered. The following distinction regarding range and type of the interaction in liquid environment can be made [30-33]:

1. Van der Waals forces existing at distances up to 10 nm;

2. Electrostatic interactions in the range of 1 to 100 nm;
3. Steric hindrance of adsorbed molecules at distances up to 100 nm;
4. Solvation forces acting up to a distance of 10 nm;
5. Capillary forces between the particles.

These forces depend on characteristics of the molecules and the surface (surface charge, active surface groups) as well as the liquid in which the interactions take place (ionic strength, polarity, pH and dissolved gases). Under living body conditions, the range of these interactions can be as large as a few tens of nanometers, which makes that interactions between surfaces structured with such dimensions effect adhesion of biomoieties.

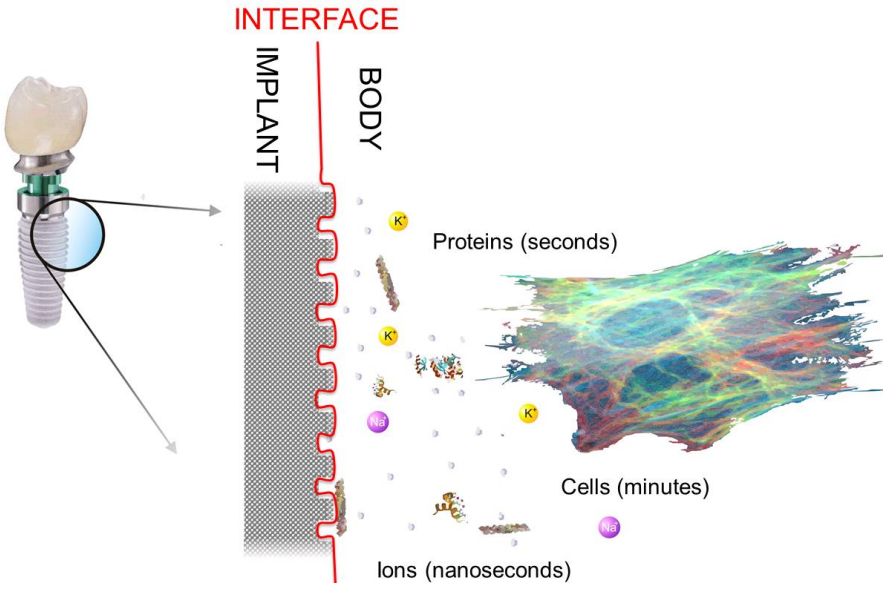

Figure 1. Artistic impression of interface (red line) between the nanostructured surface of implant and bio environment. Different types of moieties approach the surface of the implanted device at different time scales. The first process occurring at the surface is water binding, which happens within nanoseconds and has a distinct crystalline-like structure. Next, ions will build up electric double layers the thickness of which depends of ionic strength. Subsequently, at the seconds time scale, proteins adsorb to the surface creating a bio-layer and screening the surface from the environment. Finally, cells which recognize

the surface by filopodia sensing attach to the surface via characteristic interactions between cell membrane integrins and adsorbed proteins.

1.2.1. Cells

The *in vitro* interaction of various types of cells, including fibroblasts, osteoblasts, mesenchymal stem cells, and neuronal cells [34], with nanostructured biomaterials has been studied. The resulting effects depend on the cell type and may be of morphological and/or functional origin. The following mechanisms can be altered when cells become in contact with a surface nanostructure: initial cell adhesion, gene expression, protein translation, cell spreading or membrane integrin expression, and biomineralization [35-38]. Also an increase in migration and motility, stimulated by micro- and nano-fibers or microtubules, was observed [39,40]. The presence of a nanostructure on the surface changes the molecular interaction between the surface and cells [41]. Depending on cell type, cells sense nanofeatures down to 35 nm [42], 27 nm [43] or even down to as small as 13 nm [44]. The threshold of nanostructure-cell influence is not a fixed value, since different types of reactions to nanostructure were quantified in the aforementioned research. Cell responses to a surface are also influenced by the introduction of strain on the surface [45,46]. A consequence of cell seeding on topographically modified biomaterials is indeed a change in the strain in the cellular membrane, induced by the contact with a nanostructure.

1.2.2. Proteins

Nanotopography on an implant surface in the size range of solvated proteins can influence protein-surface interactions. As said above, the first reaction to the introduction of a nanostructured surface into the body is a change in water and ion layer structure [47], which is sensed by proteins [48]. This is very much related to the observation that surface wettability has a strong influence on protein adsorption, proteins respond to hydrophobic or hydrophilic surfaces by changing functionality and conformation upon adsorption [49,50]. Nanoscale curvature may also change the conformation of an adsorbed protein and

stimulates it to expose regions, which can act as primary binding sites for integrins. Certain kinds of nanostructures cause proteins to absorb beyond what would be expected based on a change in available surface area, which proves the very specific nanostructure-protein interaction [51].

Protein layers adsorbed on bio-surfaces have been studied with many different techniques. Surface coverage can be quantified with methods like quartz crystal microbalance (QCM), surface plasmon resonance (SPR), fluorescence detection, impedance spectroscopy, x-ray photoelectron spectroscopy (XPS), Fourier transform infrared spectroscopy (FTIR), attenuated total reflection IR spectroscopy (ATR), and small-angle X-ray scattering (SAXS). The morphology and localization of adsorbed proteins may be studied with atomic force microscopy (AFM), Helium Ion scanning Microscopy (HIM), high resolution scanning or transmission electron microscopies (HRSEM or HRTEM), nuclear magnetic resonance NMR or X-ray diffraction methods (XRD) [52-55].

1.3. Biomaterials micro- and nanopatterning methods

Many comprehensive reviews exist which provide an overview of methods for nanopatterning a surface and of the results obtained from utilizing them in *in vitro* or *in vivo* experiments [30,31,56]. In the following subchapters the history, trends and methods of surface modifications for biomedical applications are briefly described with a particular focus on *regular* nanofabricated surface features.

1.3.1. Stochastic methods - grit blasting, roughening etc.

Historically implanted materials had a surface finish that is characteristic for standard machining processes, namely a stochastically distributed micro or nanotopography. The surface finish was qualified by roughness or machining lay (surface pattern obtained after tooling). Further developments have led to

the employment of surface finishing methods like polishing, grit blasting or a specific coating, e.g. a ceramic deposit.

For surface modification of biomaterials, advanced methods originating from the semiconductor manufacturing field have been applied recently. Plasma treatments and the deposition of coatings by plasma sputtering, pulsed laser deposition (PLD), sol-gel procedures, electrodeposition and methods like anodization through porous anodic alumina mask [57-59].

For titanium based materials the most common stochastic methods (i.e. methods giving a random nanotopography) are titanium plasma spraying, acid etching, anodization and grit blasting, laser modification and polishing [60-62]. Additional treatments like straining or pulling of the bulk material may also be used to create discrete micro- or nanotopography on the titanium or titanium alloy surface [63]. It is though that these stochastic patterning methods might lead to better initial material fixation as well as changes in cellular reactions due to introduction of changes in surface energy, wettability or presence of functional groups [64,65]. Recently more emphasis is put on cell response driven by a *combination of nano*- and *microstructures*, with very promising results [66,67]. Dental implant companies currently explore above-mentioned methods and have employed them with success in final implantation products [68,69].

1.3.2. Microfabrication (1-100 micron)

It has for long been recognized that substrate topography can affect cell morphology and cell behavior. Early research on so-called contact guidance dates back to 1945 and showed cells aligning and migrating along fibers or grooves [70,71]. This guidance was interpreted as caused by molecular orientation of the substrate, however later work in 1964 demonstrated that cells are more likely responding to topographical features [72], in which the dictated orientation of focal adhesions has a considerable contribution [73,74].

When micromachining techniques became accessible to biological research teams, new investigations were pursued regarding cell culturing on

micromachined substrates, by the groups of Brunette et al. and Dunn et al. [75,76]. These works has brought a significant contribution to our understanding of cell guidance phenomena and the influence of parallel microgrooves on cell behavior. The following subchapters describe more recent surface modification methods utilized for surface modification on biomaterials.

1.3.3. Nanofabrication (<1 micron)

Nanofabrication approaches employed to modify biomaterial surfaces can be divided in two types: *parallel* methods, in which a larger area, of a few cm^2, is patterned in one cycle that lasts seconds to minutes, and *serial* methods, in which the pattern is build up by repeated actions at different locations, lasting tens of minutes to hours. Parallel methods are more effective in delivering reasonable sample quantities for statistical biological studies and possibly preferred from the perspective of cost-efficiency. Table 1 below gives an overview of nanopatterning methods and their characteristic advantages and disadvantages for applications in the field of biomaterials.

Table 1. Summary of nanopatterning methods employed for surface modification of biomaterials.

Method name	Description	Advantages	Disadvantages
Focused Ion Beam Lithography Critical dimensions: Down to 10 nm [77]	Gallium ions are accelerated to an energy of 5-50 keV and then focused onto the sample by electrostatic lenses. The beam sputters the material, therewith facilitating remodeling of the surface. FIB can also be used to deposit material via ion beam induced deposition.	+ direct patterning , single process, micromachining tool; + can be used to deliver molds for nanoimprint methods; + virtually full freedom in the surface structure.	- surface damage by redeposition (FIB inducted damage); - implantation of gallium ions (and also other impurity ions from vacuum environment); - amorphisation of material; - parallel method.
Colloidal lithography nanopatterning. Critical dimensions: Down to 70 nm	Colloidal lithography uses a 2D array of particles as a shadow mask or the interstices between the particles as open windows for reactive ions to create patterned bumps or pores on a substrate. This method allows a considerable	+ parallel method of large area surface patterning + pattern size adjustment by particle size + regular and	- pattern shapes restricted to island-like or well-like patterns - long range ordered structures are hard to achieve

[78,79]	freedom to control both the feature dimensions by varying the particle size and the shape of nanopores by using multilayered particle arrays or angle resolved etching techniques.	oriented patterns can be obtained + fair control of critical dimension dispersion	
Polymer demixing Critical dimensions: Down to 6 nm [80,81]	Spin-coating a film of highly immiscible polymers from a common solvent can yield to lateral domains that exhibit a well-defined topographical structure with sharp edges.	+ parallel method of large area surface patterning + easy to produce various dimensions by adjusting parameters of the polymers used	- only islands and plateau shapes possible, with irregular borders - lack of long range order of the obtained structure - large spread of critical dimensions
Electron beam lithography Critical dimensions: Down to 20 nm, virtually down to few nm [82,83]	Electron beam lithography is a serial lithographic method. Photoresist sensitive to short wavelength of 10-50 keV electrons is irradiated with electron beams in a writing process. Latter structure is developed and the remaining resist is used as a transfer mask for the structure.	+ full control on desired layout of the created pattern; + surface under resist is not affected by e-beam writing + very high resolution	- resist swelling causing loss of resolution - electron scattering causing re-exposure in case of certain (dense) design patterns - slow, high cost serial method - limited to certain material types (high vacuum compatible)
Nanoimprint lithography Critical dimensions: Sub 25 nm [84,85]	This method creates patterns by mechanical deformation of imprint resist using prefabricated mask. Subsequent etching processes transfer the imprinted pattern in a material. The imprint resist is typically a polymer formulation that is developed by heat or UV light during the imprinting. Single imprint step that allows to transform sub 25 nm patterns onto various types of substrates	+ parallel method of large area surface patterning + low cost, high throughput and high resolution + non flat substrates can be patterned using roller nanoimprint lithography + resolution virtually limited by resolution of stamp	- hard to obtain defect-free large area imprints (release problem) - feature proximity effect in dense patterned structures, caused by displacement of molded polymer resist - limited types of materials can be patterned in this method (UV or heat compatible)
SAM`s (molecular self-assembling matrices) Often with Dip-Pen lithographies where single molecules can be manipulated Critical	Biomolecule–material interaction is accomplished via molecular specificity, leading to the formation of controlled structures and functions at all scales of dimensional hierarchy. This method can be used for e.g. protein-guided ceramic formulation. Further manipulation of molecule	+ parallel method of large area surface patterning + spontaneous, energy minimum driven self-organization of molecules + a route to obtain	- good quality of pattern is hard to obtain due to thermodynamically guided reactions and local energy fluctuations. - troubles in transferring the pattern of the assembled layer of molecules into the

dimensions: molecule size [86-88]	location can be adjusted by scanning probe interactions like in AFM.	nanostructured pattern on curved substrates without guidance or management from an outside source	biomaterial
Laser light interference lithography. Critical dimensions: Down to 10 nm [89-93]	An interference pattern between two or more coherent light waves is used to expose a photosensitive resist layer. The obtained pattern is an intensity minima-maxima record in the photoresist. The latter structure is developed and used as pattern transfer mask. High energy infrared lasers can be used to directly pattern metal surfaces.	+ possibility to obtain large areas with fairly small patterns size and long range order on large areas + mask less system not requiring complex optical setups	- optical phenomena limited resolution - ultra smooth and flat substrate is required - pattern type limited to simple geometrical arrangements (fringes or pits/wells)
Other methods employed less often but with success: Langmuir-Blodgett monolayer deposition. microcontact printing.			

1.3.4. Review of fabrication methods for well-defined features on titanium

Titanium is a material widely used in microtechnology as thin layers [94], mostly for its high etch resistance and physicochemical stability provided by the native surface oxide, and good adhesion properties to other materials. Paradoxically, the first property is also rendering titanium a hard to micromachine material, requiring robust microfabrication masks and sophisticated etching chemistries. Titanium creates volatile compounds only with very few plasma etching chemistries and even then only at elevated temperatures. As a substrate, bulk titanium was used for the microfabrication of devices requiring high mechanical stability. Table 2 gives a summary of research on micro- and nanofabrication of titanium bulk materials and thin layers, for various applications.

Table 2. Brief summary of research conducted on titanium micro- and nano-fabrication using reactive ion etching techniques.

Title	Substrate material	Resist/masking material	RIE parameters	Minimal lateral critical dimension (CD)	Application	Selectivity/ etch rate
Chapter 4 in this thesis	Bulk titanium: grade 2 unanneal-ed titanium	Imprinted thermo moldable resist, thickness up to ~600 nm	$Cl_2/CF_4/O_2/Ar$ plasma with ICP source	~150 nm	*In vivo* studies of nano-structure–tissue interactions	PR:Ti=1:0.6 Etch rate 0.5 µm min^{-1}
Inductively coupled plasma reactive ion etching of titanium thin films using a Cl_2/Ar gas [95]	Ti thin films	patterned with the photoresist masks	Cl_2/Ar gas mix with ICP plasma source	>2 µm	Effects of the coil RF power, dc-bias voltage and gas pressure on the etch rate and etch profile were investigated.	PR:Ti=1:0.2 Etch rate 90 nm min^{-1}
Wafer level bulk titanium ICP etching using SU8 as an etching mask [96,97]	Bulk titanium: 99.99 % annealed titanium	20 µm SU8 layer patterned with UV lithography	Cl_2 plasma with ICP source	2 µm	High aspect ratio titanium micromachining	Etch rate 1 µm min^{-1} PR:Ti=1:2
Development of a titanium plasma etch process for uncooled titanium nanobolometer fabrication [98]	Thin layer: PVD deposited Ti on SiO_2	EBL written positive resist (ZEP-520)	BCl_3/Cl_2 gas plasma.	<100 nm	Nanobolome-ter fabrication	PR:Ti= 1:1.7
High-aspect-ratio bulk micromachining of titanium [99-101]	Bulk titanium: Grade 1 or titanium thin foils 99.6 % annealed. CMP polished prior to processing.	1.25 µm TiO_2 deposited with reactive sputtering from O_2/Ar plasma and further patterned with UV lithography and TiO_2 etching step.	Etching in Cl_2/Ar plasma with ICP source and quartz electrode.	~2 µm	Investigation of influence of: pressure, gas composition, RF and ICP sources power on Ti etching in Cl_2/Ar plasma. TIDE (Titanium ICP Deep Etching) process development;	TiO_2:Ti=1:40 Etch rate up to 2 µm min^{-1}

					Metal anisotropic reactive ion etching with oxidation process development (MARI)	
Chemistry of Titanium Dry Etching in Fluorinated and Chlorinated Gases [102]	Not stated	None	Etching in fluorinated and chlorinated plasmas	Not investigated	Investigation of reaction of titanium with fluoride and chloride and influence of oxide layer on thus	Not investigated
Investigations of the altered surface formed during the ion-assisted etching of titanium [103]	Monocrystal of titanium, 3 types of samples with different surface modifications	None	Ion beam etching (Ar 1000eV) and exposure to gaseous chlorine	Not investigated	Investigation of thermal dynamics of gaseous products during exposition of titanium to chlorine	Not investigated
Plasma Etching of Titanium for Application to the Patterning of Ti-Pd-Au Metallization.[104]	Thin layer: Filament evaporation of titanium on Si nitride wafer	MOS devices processed up to Ti etch step	CF_4, $CClF_3$, $CBrF_3$ with He, O_2 plasma chemistries. Parallel plate etcher with Pyrex enclosure	Above micron	Selectivity of plasma composition towards elements of MOS devices against titanium	Up to 280 nm min^{-1}
Scanning electron microscopic, transmission electron microscopic, and confocal laser scanning microscopic observation of fibroblasts cultured on microgrooved surfaces of bulk titanium substrata [105]	Bulk cpTi	Chromium mask evaporated by e-gun evaporation on polished surface of titanium	SF_6/O_2 Plasma in RIE etcher	Grooves of 1.0, 2.1, 5.0 and 9.2 µm	Culturing of fibroblasts and their observation with microscopy techniques	Not measured

PR = photoresist

1.4. The Importance of the project

1.4.1. Biological response to systematic features

A very specific cell response to regular nanofeatures was found in our research as well as that of other groups, from which the following conclusive observations were derived: cells align to the long axis of a regular nanostructure; cells migration is stimulated by nanostructure; up regulation or down regulation of certain enzymatic pathways occurs when the cell is in contact with the nanostructure. It was also observed that the precipitation of an inorganic phase by bone-building cells is aligned to the orientation of the long axis of nanoridges (chapter 6 in this thesis). Symmetry and regularity of the nanostructure also seems to play an important role in cellular response [106].

1.4.2. The idea of nanoridges

In biomaterials research it is desirable to have a well-defined but preferably simple model to study material-biosystem interaction. Nanoridges and grooves provide a simple geometrical system the size of which can easily be controlled and defined by a limited set of parameters, as ridge width, groove width and height of ridge (depth of groove). Excellent control and the possibility to adjust only one parameter at the time is essential for a thorough understanding of the interaction of cells with topography, and this in our view is achievable with the nanofabrication techniques proposed in this thesis.

As a result of the research conducted in this work a new type of bioactive biomaterial surface carrying nanoridges with scalable dimensions was fabricated. The nanoridges were fabricated in both silicon for *in vitro* studies and titanium for *in vivo* studies in a controlled manner applying novel fabrication routes consisting of laser interference lithography, replication by nanoimprint lithography and multiple reactive ion etching steps on silicon and medical grade titanium.

1.5. Thesis outline

Chapter 1.

A general introduction is given, including a review of research conducted on the topic of biofunctionality in relation to state of the art micro- and nanofeatures on biomedical surfaces.

Chapter 2.

A process scheme based on laser interference lithography and reactive ion etching to create nanostructures in a silicon substrate is introduced. Later chapters will apply these silicon structures for replication in a biologically relevant material, and subsequent bio-activity studies. This chapter describes the adaptation of micro- and nanomachining techniques for the fabrication and evaluation of the nanostructures studied in this thesis. An outline of the fabrication process is sketched and the important parameters influencing the fabrication result are discussed. Finally, results of a preliminary study of fibroblast alignment on tissue culture polystyrene replicas obtained from the silicon molds are presented as an example of nanostructure-cell interaction.

Chapter 3.

In this chapter the fabrication of a microstructured ceramic material is described. The fabrication is conducted with the micromachined silicon molds carrying micro-and nano structures which were introduced in chapter 2. These structures are replicated by micromolding applying tape casting. The study concentrates on finding the tape casting slurry of industrially used compositions which is the most suitable for a feasibility study. Two types of ceramics and three types of slurries are investigated. Finally, fibroblast cells are cultured on the surfaces and their morphology is investigated with SEM.

Chapter 4.

This chapter deals with process optimization for nanostructuring titanium surfaces. The molds described in chapter 2 are used as stamps for nanoimprint lithography and the structure is subsequently transferred into titanium using reactive ion etching. The implants are prepared for *in vivo* studies. The uniformity and chemical homogeneity of implantation samples is studied and a cell viability assay is performed to proof biocompatibility of the nanostructured surfaces.

Chapter 5.

In this chapter we observe interactions between proteins and created nanostructures in silicon. Several types of ECM proteins were adsorbed on dimensionally distinct nanofabricated silicon surfaces. Influence on quantity and morphology of adsorbed protein was evaluated.

Chapter 6.

This chapter describes biological *in vitro* studies on structures obtained in chapter 2. The study aims at a better understanding of the phenomena taking place between regular ridge-groove nanostructures and osteoblasts under *in vitro* conditions. Cell parameters like the interface between the nanostructures and the cell, specific gene expression and changes in cell morphology and focal adhesions are discussed.

1 Hook, F., Kasemo, B., Grunze, M. & Zauscher, S. Quantitative Biological Surface Science: Challenges and Recent Advances. Acs Nano **2**, 2428-2436 (2008).

2 Kasemo, B. Biological surface science. Surf Sci **500**, 656-677 (2002).

3 Hench, L. L. & Polak, J. M. Third-generation biomedical materials. Science **295**, 1016-1017 (2002).

4 Hutmacher, D. W. Scaffolds in tissue engineering bone and cartilage. Biomaterials **21**, 2529-2543 (2000).

5 Albrektsson, T., Zarb, G., Worthington, P. & Eriksson, A. R. The long-term efficacy of currently used dental implants: a review and proposed criteria of success. The International journal of oral & maxillofacial implants **1**, 11-25 (1986).

6 Binyamin, G., Shafi, B. M. & Mery, C. M. Biomaterials: A primer for surgeons. Seminars in Pediatric Surgery **15**, 276-283, (2006).

7 Sieminski, A. L. & Gooch, K. J. Biomaterial-microvasculature interactions. Biomaterials **21**, 2233-2241 (2000).

8 Khouw, I. M., van Wachem, P. B., Molema, G., Plantinga, J. A., de Leij, L. F. & van Luyn, M. J. The foreign body reaction to a biodegradable biomaterial differs between rats and mice. Journal of Biomedical Materials Research **52**, 439-446 (2000).

9 Campoccia, D., Montanaro, L. & Arciola, C. R. The significance of infection related to orthopedic devices and issues of antibiotic resistance. Biomaterials **27**, 2331-2339 (2006).

10 Trampuz, A. & Zimmerli, W. New strategies for the treatment of infections associated with prosthetic joints. Curr Opin Investig Drugs **6**, 185-190 (2005).

11 Darouiche, R. O. Treatment of infections associated with surgical implants. N Engl J Med **350**, 1422-1429 (2004).

12 Cooper, L. F. Biologic determinants of bone formation for osseointegration: Clues for future clinical improvements. J Prosthet Dent **80**, 439-449 (1998).

13 Olszta, M. J., Cheng, X. G., Jee, S. S., Kumar, R., Kim, Y. Y., Kaufman, M. J., Douglas, E. P. & Gower, L. B. Bone structure and formation: A new perspective. Mat Sci Eng R **58**, 77-116 (2007).

14 Kasemo, B. & Gold, J. Implant surfaces and interface processes. Advances in dental research **13**, 8-20 (1999).

15 Weryha, G. & Leclere, J. Paracrine Regulation of Bone Remodeling. Horm Res **43**, 69-75 (1995).

16 Gross, U. M. Biocompatibility--the interaction of biomaterials and host response. J Dent Educ **52**, 798-803 (1988).

17 Roberts, W. E., Helm, F. R., Marshall, K. J. & Gongloff, R. K. Rigid endosseous implants for orthodontic and orthopedic anchorage. The Angle orthodontist **59**, 247-256 (1989).

18 Lanyon, L. E. Functional strain in bone tissue as an objective, and controlling stimulus for adaptive bone remodelling. J Biomech **20**, 1083-1093 (1987).

19 Burgos-Asperilla, L., Garcia-Alonso, M. C., Escudero, M. L. & Alonso, C. Study of the interaction of inorganic and organic compounds of cell culture medium with a Ti surface. Acta Biomater **6**, 652-661 (2010).

20 Chen, Q., Kinch, M. S., Lin, T. H., Burridge, K. & Juliano, R. L. Integrin-mediated cell adhesion activates mitogen-activated protein kinases. Journal of Biological Chemistry **269**, 26602-26605 (1994).

21 Ruoslahti, E. Vol. **12** 697-715 (1996).

22 Hynes, R. O. Integrins: A family of cell surface receptors. Cell **48**, 549-554 (1987).

23 Rezania, A. & Healy, K. E. Biomimetic peptide surfaces that regulate adhesion, spreading, cytoskeletal organization, and mineralization of the matrix deposited by osteoblast-like cells. Biotechnol Prog **15**, 19-32 (1999).

24 Healy, K. E., Rezania, A. & Stile, R. A. Designing biomaterials to direct biological responses. Ann N Y Acad Sci **875**, 24-35 (1999).

25 Noh, H. & Vogler, E. A. Volumetric interpretation of protein adsorption: competition from mixtures and the Vroman effect. Biomaterials **28**, 405-422, (2007).

26 Meyer, U., Buchter, A., Wiesmann, H. P., Joos, U. & Jones, D. B. Basic reactions of osteoblasts on structured material surfaces. Eur Cell Mater **9**, 39-49 (2005).

27 Wilson, C. J., Clegg, R. E., Leavesley, D. I. & Pearcy, M. J. Mediation of biomaterial-cell interactions by adsorbed proteins: a review. Tissue Eng **11**, 1-18, (2005).

28 Tran, N. & Webster, T. J. Nanotechnology for bone materials. Wiley Interdiscip Rev Nanomed Nanobiotechnol **1**, 336-351 (2009).

29 Tengvall, P. & Lundström, I. Physico-chemical considerations of titanium as a biomaterial. Clinical Materials **9**, 115-134 (1992).

30 Martinez, E., Engel, E., Planell, J. A. & Samitier, J. Effects of artificial micro- and nano-structured surfaces on cell behaviour. Ann Anat **191**, 126-135 (2009).

31 Flemming, R. G., Murphy, C. J., Abrams, G. A., Goodman, S. L. & Nealey, P. F. Effects of synthetic micro- and nano-structured surfaces on cell behavior. Biomaterials **20**, 573-588 (1999).

32 Kriparamanan, R., Aswath, P., Zhou, A., Tang, L. & Nguyen, K. T. Nanotopography: cellular responses to nanostructured materials. J Nanosci Nanotechno **6**, 1905-1919 (2006).

33 Kieswetter, K., Schwartz, Z., Dean, D. D. & Boyan, B. D. The role of implant surface characteristics in the healing of bone. Crit Rev Oral Biol Med **7**, 329-345 (1996).

34 Mohammed, J. S., DeCoster, M. A. & McShane, M. J. Micropatterning of nanoengineered surfaces to study neuronal cell attachment in vitro. Biomacromolecules **5**, 1745-1755 (2004).

35 ter Brugge, P. J. & Jansen, J. A. Initial interaction of rat bone marrow cells with non-coated and calcium phosphate coated titanium substrates. Biomaterials **23**, 3269-3277 (2002).

36 Matsuzaka, K., Walboomers, X. F., de Ruijter, J. E. & Jansen, J. A. The effect of poly-L-lactic acid with parallel surface micro groove on osteoblast-like cells in vitro. Biomaterials **20**, 1293-1301 (1999).

37 Dalby, M. J., Riehle, M. O., Yarwood, S. J., Wilkinson, C. D. & Curtis, A. S. Nucleus alignment and cell signaling in fibroblasts: response to a micro-grooved topography. Exp Cell Res 284, 274-282 (2003).

38 Andersson, A. S., Brink, J., Lidberg, U. & Sutherland, D. S. Influence of systematically varied nanoscale topography on the morphology of epithelial cells. IEEE Trans Nanobioscience **2**, 49-57 (2003).

39 Liu, Y., Franco, A., Huang, L., Gersappe, D., Clark, R. A. & Rafailovich, M. H. Control of cell migration in two and three dimensions using substrate morphology. Exp Cell Res **315**, 2544-2557 (2009).

40 Small, J. V., Geiger, B., Kaverina, I. & Bershadsky, A. How do microtubules guide migrating cells? Nat Rev Mol Cell Biol **3**, 957-964 (2002).

41 Gumbiner, B. M. Cell adhesion: The molecular basis of tissue architecture and morphogenesis. Cell **84**, 345-357 (1996).

42 Dalby, M. J., Gadegaard, N., Riehle, M. O., Wilkinson, C. D. & Curtis, A. S. Investigating filopodia sensing using arrays of defined nano-pits down to 35 nm diameter in size. Int J Biochem Cell Biol **36**, 2005-2015 (2004).

43 Dalby, M. J., Giannaras, D., Riehle, M. O., Gadegaard, N., Affrossman, S. & Curtis, A. S. G. Rapid fibroblast adhesion to 27 nm high polymer demixed nano-topography. Biomaterials **25**, 77-83 (2004).

44 Dalby, M. J., Yarwood, S. J., Riehle, M. O., Johnstone, H. J., Affrossman, S. & Curtis, A. S. Increasing fibroblast response to materials using nanotopography: morphological and genetic measurements of cell response to 13-nm-high polymer demixed islands. Exp Cell Res **276**, 1-9 (2002).

45 Leon, A. M., Carreras, A., Barroso, J. B., Palma, J. M., Gomez, M., del Rio, L. A. & Corpas, F. J. Enzymatic nitric oxide production in pea plants and modulation under stress conditions. Free Radical Bio Med **36**, S136-S136 (2004).

46 Prodanov, L., te Riet, J., Lamers, E., Domanski, M., Luttge, R., van Loon, J. J. W. A., Jansen, J. A. & Walboomers, X. F. The interaction between nanoscale surface features and mechanical loading and its effect on osteoblast-like cells behavior. Biomaterials **31**, 7758-7765 (2010).

47 Vogler, E. A. Structure and reactivity of water at biomaterial surfaces. Adv Colloid Interface Sci **74**, 69-117 (1998).

48 Galli, C., Coen, M. C., Hauert, R., Katanaev, V. L., Groning, P. & Schlapbach, L. Creation of nanostructures to study the topographical dependency of protein adsorption. Colloid Surface B **26**, 255-267 (2002).

49 Koc, Y., de Mello, A. J., McHale, G., Newton, M. I., Roach, P. & Shirtcliffe, N. J. Nano-scale superhydrophobicity: suppression of protein adsorption and promotion of flow-induced detachment. Lab Chip **8**, 582-586 (2008).

50 Gelse, K., Poschl, E. & Aigner, T. Collagens - structure, function, and biosynthesis. Adv Drug Deliver Rev **55**, 1531-1546 (2003).

51 Rechendorff, K., Hovgaard, M. B., Foss, M., Zhdanov, V. P. & Besenbacher, F. Enhancement of protein adsorption induced by surface roughness. Langmuir : the ACS journal of surfaces and colloids **22**, 10885-10888 (2006).

52 Laricchia-Robbio, L. & Revoltella, R. P. Comparison between the surface plasmon resonance (SPR) and the quartz crystal microbalance (QCM) method in a structural analysis of human endothelin-1. Biosensors and Bioelectronics **19**, 1753-1758 (2004).

53 Go, K., Horikawa, Y., Garcia, R. & Villarreal, F. J. Fluorescent method for detection of cleaved collagens using O-phthaldialdehyde (OPA). J Biochem Biophys Methods **70**, 878-882 (2008).

54 Krahn, K. N., Bouten, C. V., van Tuijl, S., van Zandvoort, M. A. & Merkx, M. Fluorescently labeled collagen binding proteins allow specific visualization of collagen in tissues and live cell culture. Anal Biochem **350**, 177-185 (2006).

55 Staszyk, C. & Gasse, H. A simple fluorescence labeling method to visualize the three-dimensional arrangement of collagen fibers in the equine periodontal ligament. Ann Anat **186**, 149-152 (2004).

56 Yim, E. K. F. & Leong, K. W. Significance of synthetic nanostructures in dictating cellular response. Nanomedicine: Nanotechnology, Biology and Medicine **1**, 10-21 (2005).

57 Sjostrom, T., Dalby, M. J., Hart, A., Tare, R., Oreffo, R. O. C. & Su, B. Fabrication of pillar-like titania nanostructures on titanium and their interactions with human skeletal stem cells. Acta Biomater **5**, 1433-1441 (2009).

58 Adamopoulos, O. & Papadopoulos, T. Nanostructured bioceramics for maxillofacial applications. J Mater Sci Mater Med **18**, 1587-1597 (2007).

59 Best, S. M., Porter, A. E., Thian, E. S. & Huang, J. Bioceramics: Past, present and for the future. J Eur Ceram Soc **28**, 1319-1327 (2008).

60 Le Guehennec, L., Soueidan, A., Layrolle, P. & Amouriq, Y. Surface treatments of titanium dental implants for rapid osseointegration. Dent Mater **23**, 844-854 (2007).

61 Jayaraman, M., Meyer, U., Buhner, M., Joos, U. & Wiesmann, H. P. Influence of titanium surfaces on attachment of osteoblast-like cells in vitro. Biomaterials **25**, 625-631 (2004).

62 Fu, J., Hu, Y. Y., Guo, Z., Zhang, Y. Q., Hao, Y. L. & Li, S. J. Effect of surface micro-topography of titanium material on the behaviors of rabbit osteoblast in vitro. Appl Surf Sci **255**, 286-289 (2008).

63 Faghihi, S., Azari, F., Zhilyaev, A. P., Szpunar, J. A., Vali, H. & Tabrizian, M. Cellular and molecular interactions between MC3T3-E1 pre-osteoblasts and nanostructured titanium produced by high-pressure torsion. Biomaterials **28**, 3887-3895 (2007).

64 Olivares-Navarrete, R., Hyzy, S. L., Hutton, D. L., Erdman, C. P., Wieland, M., Boyan, B. D. & Schwartz, Z. Direct and indirect effects of microstructured titanium substrates on the induction of mesenchymal stem cell differentiation towards the osteoblast lineage. Biomaterials **31**, 2728-2735 (2010).

65 Sardella, E., Favia, P., Gristina, R., Nardulli, M. & d'Agostino, R. Plasma-aided micro- and nanopatterning processes for biomedical applications. Plasma Process Polym **3**, 456-469 (2006).

66 Zinger, O., Anselme, K., Denzer, A., Habersetzer, P., Wieland, M., Jeanfils, J., Hardouin, P. & Landolt, D. Time-dependent morphology and adhesion of osteoblastic cells on titanium model surfaces featuring scale-resolved topography. Biomaterials **25**, 2695-2711 (2004).

67 Puckett, S., Pareta, R. & Webster, T. J. Nano rough micron patterned titanium for directing osteoblast morphology and adhesion. Int J Nanomedicine **3**, 229-241 (2008).

68 Kang, B. S., Sul, Y. T., Oh, S. J., Lee, H. J. & Albrektsson, T. XPS, AES and SEM analysis of recent dental implants. Acta Biomater **5**, 2222-2229 (2009).

69 Fandridis, J. & Papadopoulos, T. Surface characterization of three titanium dental implants. Implant Dent **17**, 91-99 (2008).

70 Weiss, P. Experiments on cell and axon orientation in vitro; the role of colloidal exudates in tissue organization. J Exp Zool **100**, 353-386 (1945).

71 Weiss, P. Cell Contact. Int Rev Cytol **7**, 391-423 (1958).

72 Curtis, A. S. G. & Varde, M. Control of Cell Behavior - Topological Factors. J Natl Cancer I **33**, 15-& (1964).

73 Buck, R. C. Contact Guidance in the Sub-Endothelial Space - Repair of Rat Aorta In vitro. Exp Mol Pathol **31**, 275-283 (1979).

74 Ohara, P. T. & Buck, R. C. Contact Guidance In vitro - Light, Transmission, and Scanning Electron-Microscopic Study. Exp Cell Res **121**, 235-249 (1979).

75 Brunette, D. M. Fibroblasts on Micromachined Substrata Orient Hierarchically to Grooves of Different Dimensions. Exp Cell Res **164**, 11-26 (1986).

76 Dunn, G. A. & Brown, A. F. Alignment of Fibroblasts on Grooved Surfaces Described by a Simple Geometric Transformation. J Cell Sci **83**, 313-340 (1986).

77 Langford, R. M., Nellen, P. M., Gierak, J. & Fu, Y. Q. Focused ion beam micro- and nanoengineering. Mrs Bull **32**, 417-423 (2007).

78 Hanarp, P., Sutherland, D., Gold, J. & Kasemo, B. Nanostructured model biomaterial surfaces prepared by colloidal lithography. Nanostruct Mater **12**, 429-432 (1999).

79 Choi, D. G., Yu, H. K., Jang, S. G. & Yang, S. M. Colloidal lithographic nanopatterning via reactive ion etching. J Am Chem Soc **126**, 7019-7025 (2004).

80 Walheim, S., Boltau, M., Mlynek, J., Krausch, G. & Steiner, U. Structure formation via polymer demixing in spin-cast films. Macromolecules **30**, 4995-5003 (1997).

81 Minelli, C., Geissbuehler, I., Eckert, R., Vogel, H., Heinzelmann, H. & Liley, M. Organization of nanoscale objects via polymer demixing. Colloid Polym Sci **282**, 1274-1278 (2004).

82 Liddle, J. A., Gallatin, G. M., Ocola, L. E., Division, E. F., LBNL & Center, I. T. J. W. R. Resist requirements and limitations for nanoscale electron-beam patterning. Mat. Res. Soc. Symp. Proc **739**, 19-30 (2003).

83 Vieu, C., Carcenac, F., Pepin, A., Chen, Y., Mejias, M., Lebib, A., Manin-Ferlazzo, L., Couraud, L. & Launois, H. Electron beam lithography: resolution limits and applications. Appl Surf Sci **164**, 111-117 (2000).

84 Chou, S. Y., Krauss, P. R. & Renstrom, P. J. Nanoimprint lithography. J Vac Sci Technol B 14, 4129-4133 (1996).

85 Schift, H. Nanoimprint lithography: An old story in modern times? A review. Journal of Vacuum Science and Technology B: Microelectronics and Nanometer Structures **26**, 458-480 (2008).

86 Zhang, S. Fabrication of novel biomaterials through molecular self-assembly. Nat Biotechnol **21**, 1171-1178 (2003).

87 Tamerler, C. & Sarikaya, M. Molecular biomimetics: utilizing nature's molecular ways in practical engineering. Acta Biomater **3**, 289-299 (2007).

88 Piner, R. D., Zhu, J., Xu, F., Hong, S. & Mirkin, C. A. 'Dip-pen' nanolithography. Science **283**, 661-663 (1999).

89 Hong, M. H., Huang, S. M., Luk'yanchuk, B. S. & Chong, T. C. Laser assisted surface nanopatterning. Sensor Actuat a-Phys **108**, 69-74 (2003).

90 Brueck, S. R. J. Optical and interferometric lithography -nanotechnology enablers. Proceedings of the IEEE **93**, 1704-1721 (2005).

91 Lamers, E., Frank Walboomers, X., Domanski, M., te Riet, J., van Delft, F. C. M. J. M., Luttge, R., Winnubst, L. A. J. A., Gardeniers, H. J. G. E. & Jansen, J. A. The influence of nanoscale grooved substrates on osteoblast behavior and extracellular matrix deposition. Biomaterials **31**, 3307-3316 (2010).

92 Luttge, R., Van Wolferen, H. A. G. M. & Abelmann, L. Laser interferometric nanolithography using a new positive chemical amplified resist. Journal of Vacuum Science and Technology B: Microelectronics and Nanometer Structures **25**, 2476-2480 (2007).

93 Mücklich, F., Lasagni, A. & Daniel, C. Laser interference metallurgy - Periodic surface patterning and formation of intermetallics. Intermetallics **13**, 437-442 (2005).

94 O'Mahony, C., Hill, M., Hughes, P. J. & Lane, W. A. Titanium as a micromechanical material. J Micromech Microeng **12**, 438-443 (2002).

95 Xiao, Y. B., Kim, E. H., Kong, S. M., Park, J. H., Min, B. C. & Chung, C. W. Inductively coupled plasma reactive ion etching of titanium thin films using a Cl2/Ar gas. Vacuum **85**, 434-438 (2010).

96 Zhao, G., Shu, Q., Tian, Y., Zhang, Y. M. & Chen, J. Wafer level bulk titanium ICP etching using SU8 as an etching mask. J Micromech Microeng **19**, 095006 (2009).

97 Zhao, G., Tian, Y., Shu, Q. & Chen, J. Evalution of Bulk Titanium DRIE Using SU-8 As Soft Mask. 2009 4th Ieee International Conference on Nano/Micro Engineered and Molecular Systems, Vols **1** and **2**, 514-517 (2009).

98 Gilmartin, S. F., Arshak, K., Bain, D., Lane, W. A., Collins, D., Arshak, A., McCarthy, B., Newcomb, S. B. & Walsh, M. Development of a titanium plasma etch process for uncooled titanium nanobolometer fabrication. Microelectron Eng **86**, 971-975 (2009).

99 Aimi, M. F., Rao, M. P., Macdonald, N. C., Zuruzi, A. S. & Bothman, D. P. High-aspect-ratio bulk micromachining of titanium. Nat Mater **3**, 103-105 (2004).

100 Parker, E. R., Thibeault, B. J., Aimi, M. F., Rao, M. P. & MacDonald, N. C. Inductively coupled plasma etching of bulk titanium for MEMS applications. J Electrochem Soc **152**, C675-C683 (2005).

101 Parker, E. R., Rao, M. P., Turner, K. L., Meinhart, C. D. & MacDonald, N. C. Bulk micromachined titanium microneedles. J Microelectromech S **16**, 289-295 (2007).

102 Fracassi, F. & Dagostino, R. Chemistry of Titanium Dry Etching in Fluorinated and Chlorinated Gases. Pure Appl Chem **64**, 703-707 (1992).

103 O'Brien, W. L. & Rhodin, T. N. JVST B: Microelectronics and nanostructures **7**, 1244-1251 (1989).

104 Mogab, C. J. & Shankoff, T. A. Plasma Etching of Titanium for Application to the Patterning of Ti-Pd-Au Metallization. J Electrochem Soc **124**, 1766-1771 (1977).

105 Den Braber, E. T., Jansen, H. V., De Boer, M. J., Croes, H. J. E., Elwenspoek, M., Ginsel, L. A. & Jansen, J. A. Scanning electron microscopic, transmission electron microscopic, and confocal laser scanning microscopic observation of fibroblasts cultured on microgrooved surfaces of bulk titanium substrata. Journal of Biomedical Materials Research **40**, 425-433 (1998).

106 Curtis, A. S., Casey, B., Gallagher, J. O., Pasqui, D., Wood, M. A. & Wilkinson, C. D. Substratum nanotopography and the adhesion of biological cells. Are symmetry or regularity of nanotopography important? Biophys Chem **94**, 275-283 (2001).

2.

SILICON NANOFABRICATION APPLIED IN THE MANUFACTURING OF LARGE AREA REPLICATION MOLDS

Abstract

In this chapter a new approach for the fabrication of large-area nanostructured bioactive surfaces containing ridge-groove features with an optimized ridge-to-groove ratio control and scalable pattern periods is presented. Scalability of nanostructures is achieved in all 3 dimensions by introducing a complex multi-step fabrication process. Silicon molds with a period in the range of 150 up to 1000 nm were used for the replication of nanostructures into polymeric biomaterial of a specific biocompatibility. Subsequently, these nanostructured polymer slabs were applied in a fibroblast cytotoxicity *in vitro* model. The nanofabrication method optimized in this study provides an essential experimental platform for the study of cell behavior.

2.1. Introduction

Nanoscale topography is recognized as an important parameter guiding biochemical and cell reactions at the interface between a tissue and an implanted material [1-3]. It is therefore expected that artificially created nanostructures on biomaterials may complement the naturally existing nano- and micro- environment of the implant, for example, during osseointegration of bone implants [4,5]. In order to study the influence of nanotopography, appropriate substrata are required. The optimization of nanomachining processes leading to the production on such nanostructured substrates for *in vitro* biological evaluation is the main objective of the work conducted here. We communicate a new approach to optimize and characterize silicon molds for the fabrication of large-area nanostructured bioactive surfaces with a controlled pitch, ridge-to-groove ratio, and depth. In literature various methods to generate nanotopology have been described, such as top-down methods like electron beam lithography (EBL) with subsequent etching or bottom-up techniques like polymer demixing and colloidal lithography. Although EBL provides a large variety of shapes, the throughput of this method for dense, large-area (i.e. a few cm^2) patterning is restricted [3,7,10]. And although very recently significant progress was reported in achieving long-range order in self-organized systems, the scalability of this method (in terms of variation in feature size) is typically limited to particle-specific symmetry and range of interactions, so that systematic scaling studies are not yet possible [11, 12].

On the contrary, established Laser Interference Lithography (LIL) and Reactive Ion Etching (RIE) methods give the opportunity to create regular, scalable nanofabricated features. By the very nature of the interference principle, LIL works on large areas by which property both the cost and time of template fabrication with sub micrometer features is significantly reduced. Using LIL for the patterning of areas larger than 4 cm^2 has previously been reported for silicon photonic crystals and magnetic media patterning [13,15]. Recently, also biological applications of the method were studied, e.g., Choi et al. presented a study of

cell response to a highly regular nanoarray of sharp tips with a period of 230 nm on 2 × 2 cm^2 silicon substrates delivered using LIL and Deep Reactive Ion Etching [16]. We also investigated the influence of nanogrooves and nanoridges on cell behavior, however up to now the investigated field size was restricted to an area of 500 × 500 μm^2 based on the employed EBL-assisted template manufacture [17]. In this previous study it was found that larger pattern areas are required to support statistically relevant and quantitative biological data collection. Utilizing LIL and RIE silicon nanomachining, the current chapter introduces a new approach for the optimization and characterization of such large-area silicon molds leading to the replication of nanostructured bioactive surfaces, while allowing varying systematically the pattern period in the range from 1 μm down to 150 nm and the height of the nanostructure at a controlled ridge-to-groove ratio.

2.2. Materials and Methods

Control of lithographic dimensions in a pattern transfer process is a multiparameter problem and must be carefully investigated for a given application. For our purpose, generating scalable nanostructures to investigate their bioactivity, the dimensions of the nanostructures were mainly controlled by lithographic exposure time and a series of coupled etching steps used to fabricate a silicon mold. Figure 2 shows a schematic drawing of the desired geometry aiming for a defined set of parameters, which can be systematically changed in our fabrication method. Two types of photoresist and two routes of fabrication were used for creating nanopatterns with distinct Pitch, Height, Ridge and Groove (P, H, R and G respectively). The low aspect ratio (AR=H/R) structures were created with positive tone photoresist, and the high AR structures were created using negative tone photoresist. In the following sections details of the used materials and methods are described. Figure 3 and Figure 4 are schematically showing the essential steps of both used process flows.

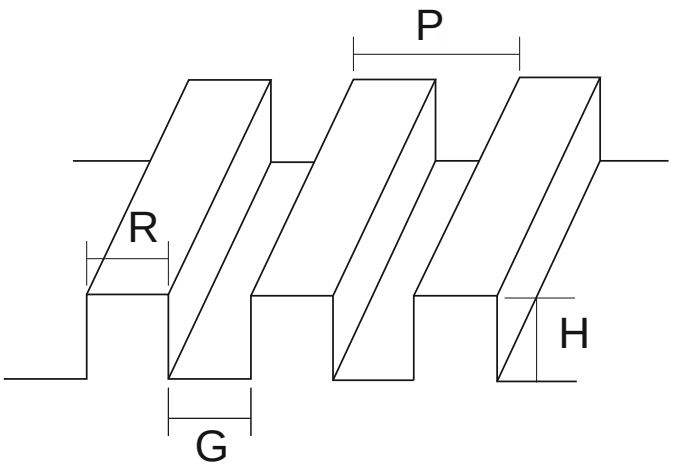

Figure 2. Geometry of nanostructure with set of parameters used to describe it: P) period of structure; R) ridge width; G) groove width; H) structure height; also two more parameters to describe the structure were introduced, aspect ratio (AR=H/R) and ridge-to-groove ratio $R_{R/G}$.

The fabrication of the nanostructures consisted of three main steps. In the first step LIL was used in order to create a regular pattern in either positive or negative tone photoresist spin-coated on a silicon wafer. The second step was the combined reactive ion etching steps to transfer the pattern from the resist layer into silicon. Finally masters were replicated from selected samples on polystyrene substrates for cell studies by solvent casting. Details of the process steps are described in the following subchapters.

2.2.1. Substrate preparation

Single-side polished 4 inch {100} silicon wafers were selected for the fabrication of molds. Spin-coating of a resist stack was performed on OPTIcoat ST22+ (Sister Semiconductor Equipment). A tri-layer resist system was applied (Figure 3 A and Figure 4 A). The stack consisted of: a DUV30-J6 bottom antireflective coating (BARC, Brewer Science), either positive or negative photoresist (PEK-500 or MaN-2403 respectively, Sumitomo Chemical, Microresist GmbH) and an Aquatar-6A top antireflective coating, (TARC,

Brewer Science). The two distinct photoresist tones were used as follows: for the low aspect ratio structures, a PEK-500 positive resist was used and for the high aspect ratio structures a negative MaN-2403 was used. It was found that configuration of layers of 13 nm BARC for positive and 38 nm BARC for negative resist, 140 nm photo resist, and approximately 5 nm TARC gives optimum stability under ambient conditions, and a high structural resolution. In the lithographic step, a fourth harmonic continuous-wave yttrium aluminum garnet laser MBD 266 system (Coherent Inc., USA) with a wavelength of 266 nm was used as the coherent light source. A Lloyd's mirror interference setup was utilized as an interference pattern generator. The defining value for pattern pitch is the angle of incidence in the interference setup. The angle (θ) defines the period of structure (P) according to the formula $P = \lambda \times (2 \sin \theta)^{-1}$, where λ is the wavelength of the used light source (266 nm). Angles (θ) were set to 7.64°, 12.80°, 26.32°, 41.68° and 62.45° to give periods of: 1000 nm, 600 nm, 300 nm 200 nm and 150 nm, respectively. All exposures on positive resist were done with a dose of 4.5 mJ cm^{-2}, for negative tone resist doses depending on the desired resist R:G ratio were varied between 3.5 to 9 mJ cm^{-2}. The applied exposure dose together with parallel plate plasma etching define the R:G ratio for structures based on negative resist. A post-exposure bake was performed for 90 s at 105°C for positive resist, whereas negative resist did not require post-exposure bake. After lithography, latent resist patterns were manually developed in 75 % v/v OPD4262 in water (Fuji-film Electronic Materials) for a time between 30 to 40 seconds depending on structure pitch, yielding a resist pattern according to the schematic drawing given in Figure 3 B for positive resist and Figure 4 B for negative resist.

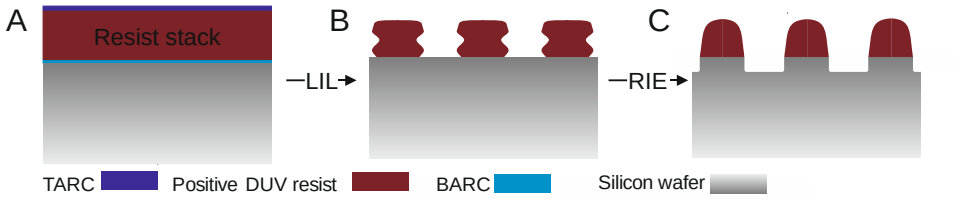

Figure 3. Schematic of the route used for preparation of nanofabricated molds with positive PEK-500 resist. The route consist of three steps: (A) substrate preparation by cleaning and spinning of trilayer resist stack; (B) laser interference lithography (LIL); (C) pattern transfer by Reactive Ion Etch (RIE) processes into the silicon substrate.

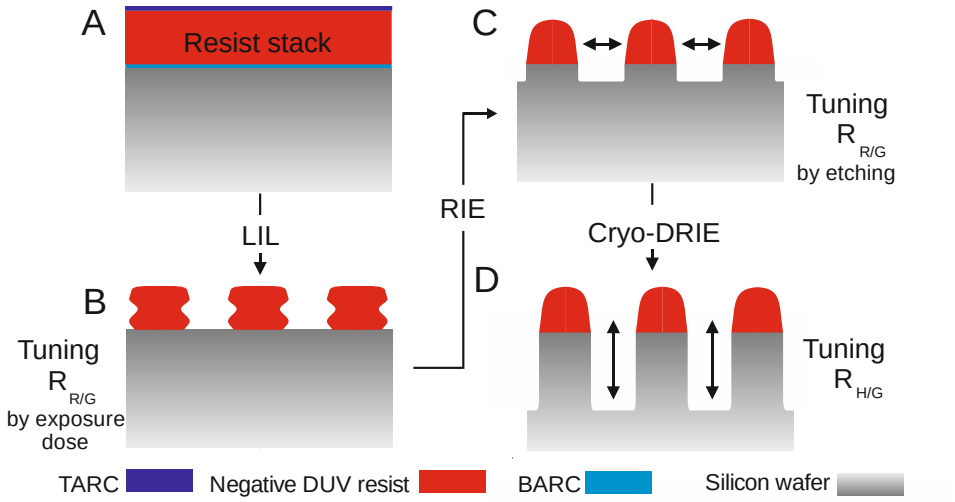

Figure 4. Schematic of optimized LIL-RIE route conducted with negative tone MaN-2403 photoresist. Specific dimensions of nanostructures can be realized by a combination of two RIE steps; first using a variable LIL exposure dose and parallel plate reactor (C) to tune the ridge-to-groove ratio ($R_{R/G}$) and subsequently adjusting the height-to-groove width ratio ($R_{H/G}$) by cryogenic deep reactive ion etching in an inductively coupled plasma RIE (D).

2.2.2. Pattern transfer using silicon reactive ion etching

After lithography, the first etching step removes the BARC and was common for both tones of photoresist. This etch-through was conducted in an oxygen plasma applying 280 W power, 1 Pa pressure 8 sccm O_2 gas flow, and 18 s etching time for all pitch sizes. Initial silicon etching experiments with positive resist wafers were carried out transferring the pattern in a PlasmaTherm 790 (Unaxis) parallel plate etcher. After oxygen plasma the system was switched to an SF_6:O_2 containing plasma composition and the silicon etching process starts in standard RIE mode. All parallel plate RIE process steps for positive resist were carried out at 10°C using substrate stage water cooling. For the negative resist pattern process samples were pre-etched in a parallel plate etcher with SF_6:O_2 plasma at 15°C to tune the R:G ratio followed by etching in a cryogenic Deep RIE process to obtain the desired depth. The optimization studies of deep etching were carried out in an Adixen AMS 100SE Inductively Coupled Reactive Ion Etcher (Alcatel) at -120°C utilizing alternating SF_6 and C_4F_8 plasma chemistry (so-called "Bosch process"). Details of the etching recipes are given below in the discussion of the respective results.

2.2.3. Dimensional analysis and preparation of reference surfaces

To characterize the silicon nanostructures micrographs were obtained using a High Resolution Scanning Electron Microscope (HRSEM) LEO 1550 (Carl Zeiss SMT Inc.). In addition Atomic Force Microscopy (AFM) scans of low aspect ratio structures were performed on a Digital Instruments Nanoscope III AFM in TappingMode™ with high frequency SiN AFM tip (Nanosensors), image analysis was done with ImageJ software for both AFM and HRSEM [19]. AFM image analysis was carried out in several steps in order to obtain lateral dimensions of the structures of LIL based silicon patterns obtained with positive resist. In the first step a line was drawn connecting both edges of the AFM scan field perpendicular to the line-pattern orientation and a gray scale intensity plot of pixels along this line was produced. The obtained plot was differentiated with respect to position, in order to visualize the maximum change of surface

topography, which corresponds to the slope of the nanostructures (the slope is caused by the finite dimensions of the AFM tip). In order to obtain information about the uniformity of positive and negative resist based structures on the scale of the 4 inch wafer, a SEM scan of the molds with a pattern period of 200 nm were obtained. For etched positive resist wafers, cross-sectional micrographs were taken across the wafer diameter at positions 1 cm apart from each other over a total distance of 6 cm starting from the very edge of the exposure area. The feature sizes deducted using ImageJ analyses are plotted in Figure 5. Error bars are the standard deviations in the data derived from the image analysis. The surface areas are relative to a flat surface ($Area_{flat}/Area_{nanostructured}$) using the idealized rectangular profile of a nanostructure with the specified values for height, ridge and groove width. To benchmark the values of the increase in surface area, they were compared with the values obtained for two commonly used non-lithographic surface treatments. Thus, to increase surface roughness, medical grade titanium specimens were exposed either to a self-built powder blast jet of Al_2O_3 particles of 20 μm diameter or to a 1 % aqueous solution of hydrofluoric acid for 5 min. Both surfaces were scanned with AFM and the increase of surface area was compared to the idealized flat surface, using Nanoscope software.

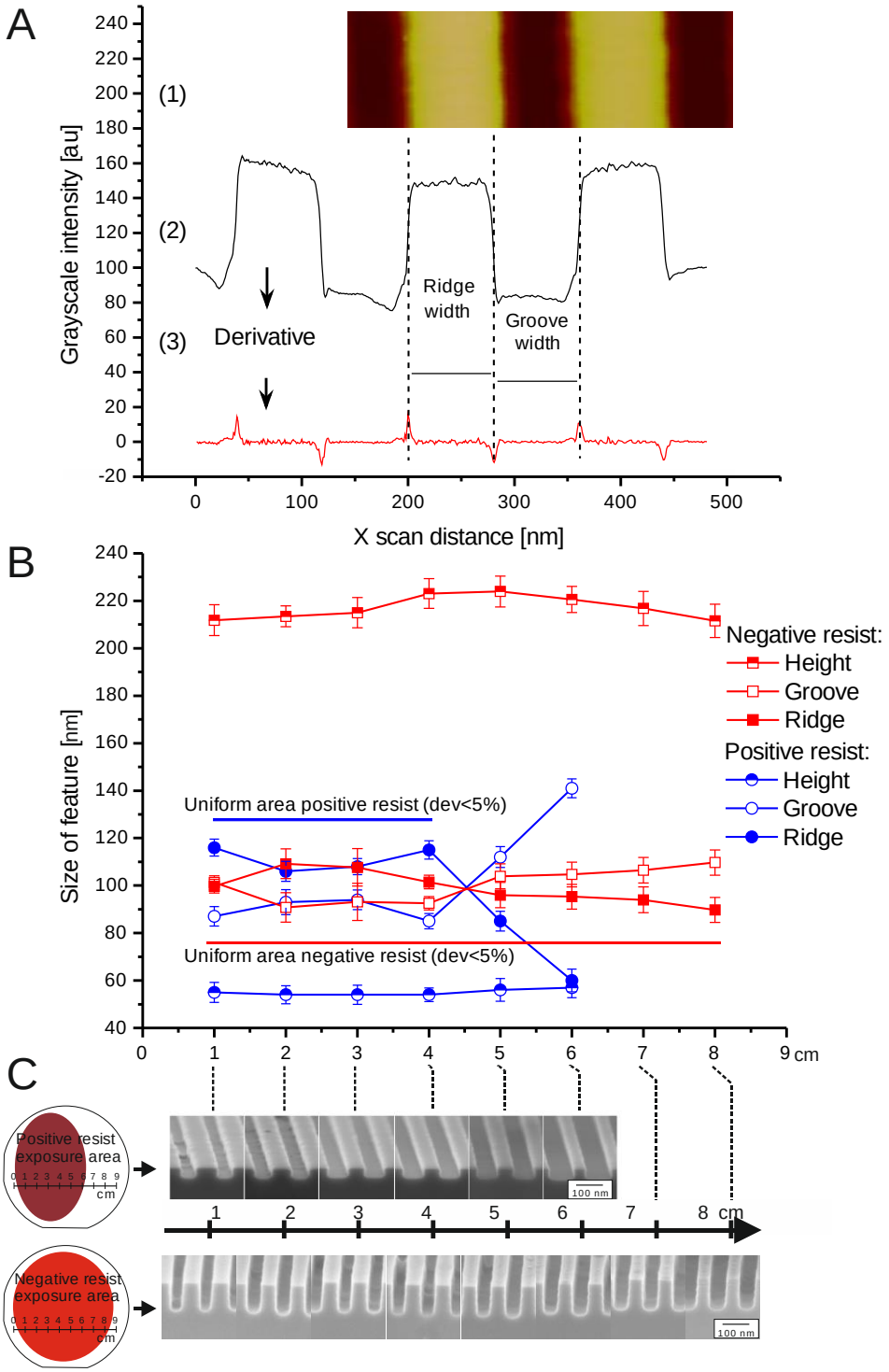
A
(1)
(2)
(3)
Derivative
Ridge width
Groove width
Grayscale intensity [au]
X scan distance [nm]
B
Size of feature [nm]
Uniform area positive resist (dev<5%)
Uniform area negative resist (dev<5%)
Negative resist:
Height
Groove
Ridge
Positive resist:
Height
Groove
Ridge
cm
C
Positive resist exposure area
Negative resist exposure area
100 nm
cm

Figure 5. Overview of measurement method and graphical representation of uniformity for wafers based with positive resist. A) Representation of the method used for measuring the dimensions of the low aspect ratio structures with AFM. The method consists of three steps: 1) Taking an AFM scan of a specific area on the substrate, 2) line plot from the AFM scan, which represents an outline of a cross-section of the surface (depicted by line A-A on the AFM scan) and 3) differentiating the line plot and measuring the distance between maxima/minima of the obtained derivative. B) Characterization of the uniformity of the exposure area with values obtained from HRSEM micrographs for both negative and positive resist C) Cross-sectional scanning electron micrographs of positive and negative resist based nanostructures with a 200 nm period at various positions across the wafer. Every micrograph was taken at a distance of 1 cm from the previous one starting from the very edge of the exposed area. At the left side the total exposure area is depicted relative to the full size of the silicon wafer.

2.2.4. Preparation of cell culturing substrates

For a fabrication technology to become applicable to medical implant problems, it is important that first proof is provided of the biocompatibility of the obtained materials. We selected the standard fibroblast *in vitro* cell culturing model for the evaluation of bioactivity of nanostructured surfaces based on the novel fabrication process presented here. The following sections describe the experimental method and conditions of such an *in vitro* cell test.

2.2.4.1. Preparation of replicas from the molds and preparationof culture dishes

The polymer slabs for cellular assay were replicated by solvent casting from the low aspect ratio positive resist based silicon molds. A Teflon® ring was pressed to the surface of the silicon mold using a rubber ring as a sealing. Culture-grade polystyrene, PS (Acros Organics), which was dissolved in chloroform (Aldrich) in a ratio of 25g/150ml, was poured into the ring on the mold. The chloroform was evaporated overnight. In this way, identical multiple copies were obtained. To create culture dishes, 2 cm diameter and 1 cm high PS rings were glued on the surface of the PS nanostructured slabs, using a small amount of casting

solution. The dishes were treated by a radiofrequency glow-discharge (RFGD) argon plasma for 5 minutes at 10 Pa for sterilization and to enhance cell adhesion.

2.2.4.2. Fibroblast culture on nanopatterned substrates

Rat dermal fibroblasts (RDF) were obtained from the ventral skin of male Wistar rats as described by Freshny [6]. Cells were cultured in minimum essential medium alpha (α-MEM) (Invitrogen) supplemented with 10 % Fetal Calf serum (FCS) and gentamicin (50 μg ml^{-1}). Cell culture experiments on the substrates were performed at 6^{th} culture passage. Prior to transferring the cells to the substrates, cells were detached using trypsin/EDTA (0.25 % w/v trypsin/0.02 % EDTA) (Invitrogen) and concentrated by centrifugation at 1500 rpm for 5 minutes. Subsequently cells were resuspended in culture medium, quantified using a Coulter® counter (Beckman Coulter Inc., Fullerton, CA, USA) and seeded at a density of 10000 cells cm^{-2}. Fibroblasts were cultured for 24 hours on the nanostructured substrates and thereafter fixed in 2 % glutaric aldehyde in 0.1M sodium cacodylate, dehydrated in a graded series of ethanol (from 70 % up to 100 %), and dried to air after final immersion in tetramethylsilane. The substrates were sputter coated with gold and observed using a Jeol 6310 SEM.

2.3. Results and discussion

The theoretical limit of structural resolution of the LIL method in the present work is a period of 133 nm which originates from the wavelength of the light source used in the lithography step (266 nm). This feature size is in the range of dimensions that are thought to be relevant for biological processes, where cells interact with surfaces. It is known that optical pattern transfer with a Lloyd's mirror setup may suffer from various aberrations that may reduce pattern uniformity. Therefore it is important to determine the uniform part of the patterned area after the completed pattern transfer process, especially because a high uniformity of the nanostructures over a large area forms the basis of the

mold fabrication process. It was found that both positive and negative resist derived surfaces give satisfying surfaces for biological studies, however control of the lateral dimensions in the LIL process and uniformity of delivered pattern are more satisfying for the negative resist system.

2.3.1. Optimizing anisotropy in pattern transfer using Si RIE

We first optimized the silicon etching profiles in the parallel plate RIE process by starting with the selection of two etching times 18 s and 60 s for a given set of etching conditions (50 sccm SF_6, 7 sccm O_2, 2.7 Pa, 0.4 W cm^{-2} power density). From these two extremes of the process window, we observed that an increase of the power density while at the same time decreasing the gas flows and the total chamber pressure leads to an increase in etching anisotropy. Thus, we yielded vertical side wall profiles at a power density of 0.61 W cm^{-2} with a gas mixture of 30 sccm of SF_6 and 5 sccm of O_2 at a process pressure of 2 Pa. Ideally, in lithography processing the resist pattern defines the lateral dimensions of the desired features. The LIL process for positive resist unfortunately does not allow this level of pattern flexibility. Utilizing a parallel plate etcher, however, the etching conditions can be optimized to maintain the ridge-to-groove width ratio at 1:1 throughout the scaling of the pattern period for all fabricated molds. For negative resist system, scalability of ridge-to-groove ratio can be achieved already at the LIL exposure level with changing the radiation dose and subsequently fine-tuning the $R_{R/G}$ with a parallel plate etching step (Figure 6). Consequently, this process is limited in controlling the etched depth (height of nanostructures) at the same time.

The resulting profiles for five low aspect ratio silicon templates obtained using positive resist are shown in Figure 6 A-E, whereas the optimized etching times to achieve a ridge-to-groove width ratio of 1:1 are 54 s for a 1000 nm (Figure 6 A); 40 s for a 600 nm (Figure 6 B), 21 s for a 300 nm (Figure 6 C), 18 s for a 200 nm (Figure 6 D), and 14 s for a 150 nm period (Figure 6 E), respectively. Although these molds are already very useful for initial biological studies we wanted to increase the overall control of the ridge to groove ratios and their

lateral uniformity, therefore we optimized the process using negative tone resist. This allows us to tune the ridge-to-groove ($R_{R/G}$) ratio already at the lithography step (Figure 7) and height-to-groove width ratio in the RIE and cryo-DRIE etching steps ($R_{H/G}$). For these experiments we first evaluated the etching performance for pattern transfer from the LIL resist into the silicon using a cryo-DRIE process employing an inductively coupled plasma source, and fixed exposure dose of 4.5 mJ cm^{-2} only. The etching parameters of this standard alternating cryogenic ICP-RIE step are: 50 sccm SF_6 for 3 s and 40 sccm C_4F_8 for 1 s at an RF power of 500 W, and LF power of 80 W at a substrate to source distance of 200 mm. Despite the very high aspect ratio of up to 25, which can be generated for the grooves, e.g., at the nanoscale dimensions of a 600 nm pattern period with an etching time of 240 s (Figure 9 (top)), it is difficult to control $R_{R/G}$ in the range where $R_{R/G} < 1$ directly, since this value is derived by the definition of the resist pattern using LIL only and the exposure dose cannot be lowered below a certain threshold (~3.5 mJ cm^2) without loss of pattern uniformity. The value for the aspect ratio (AR=25) is deducted by taking the average of the dimensions of the ten grooves shown in Figure 9 (top). Because we wanted the possibility to tune both ratios independently, we combined the cryo-DRIE etching step with the parallel plate etching step, tuning $R_{R/G}$ towards 1:1, into one processing route for scalable silicon molds. Figure 4 gives a schematic overview of all the steps that can be applied to independently control $R_{R/G}$ and $R_{H/G}$, as is demonstrated in Figure 9 (bottom) in a comparison to the result achieved by cryo-DRIE as the only etching step. In the combined process first LIL was performed with an exposure dose of 4.5 mJ cm^{-2}, followed by RIE for the BARC etch-through and tuning of $R_{R/G}$ at an etching time of 17 s. Subsequently the sample is transferred to the cryo-DRIE process and exposed to alternating plasma chemistry for an etching time of 44 s. The etching times of both RIE steps have to be optimized for the various pattern periods. Figure 8 shows the results of all five silicon molds given for the various pattern periods according to this combined process strategy. If the exposure parameters in LIL were further changed, freedom of controlling $R_{R/G}$ would be more pronounced,

like it is shown in Figure 7. Although further dimensional tuning maybe required for the biological studies, we have herewith developed a stable and versatile platform, utilizing negative resist LIL, and combined reactive ion etching processes to provide molds with scalable dimensions for the fabrication of bio-active substrates.

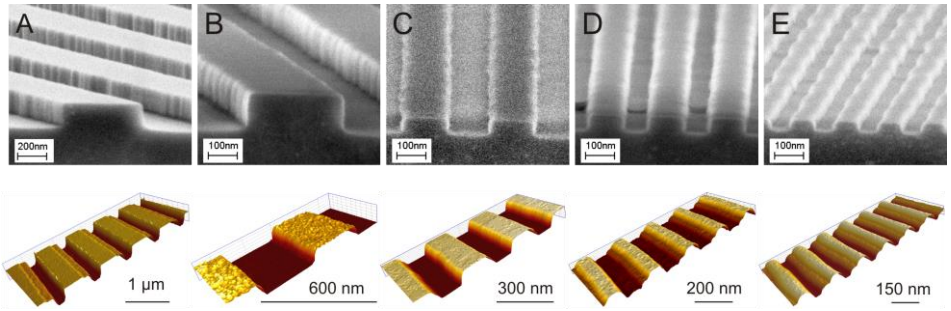

Figure 6. Overview of silicon nanostructures created by positive resist LIL and RIE only. Patterns with periods from 1 µm down to 150 nm were optimized at a ridge-to-groove width ratio of 1:1. The smallest lateral size of the ridge realized in this experiment was 71 nm. Note that during scaling of the pattern period the height-to-groove width ratio varies for the different dimensions. The different pattern periods emerged from the angle of exposure in the experiment. Exposure parameters in LIL and RIE etching times are: A) exposure at 7.6°, etching time: 54 s; B) exposure at 12.8°, etching time: 40 s; C) exposure at 26.3°, etching time: 21 s; D) exposure at 41.6°, etching time: 18 s; E) exposure at 62.4°, etching time: 14 s.

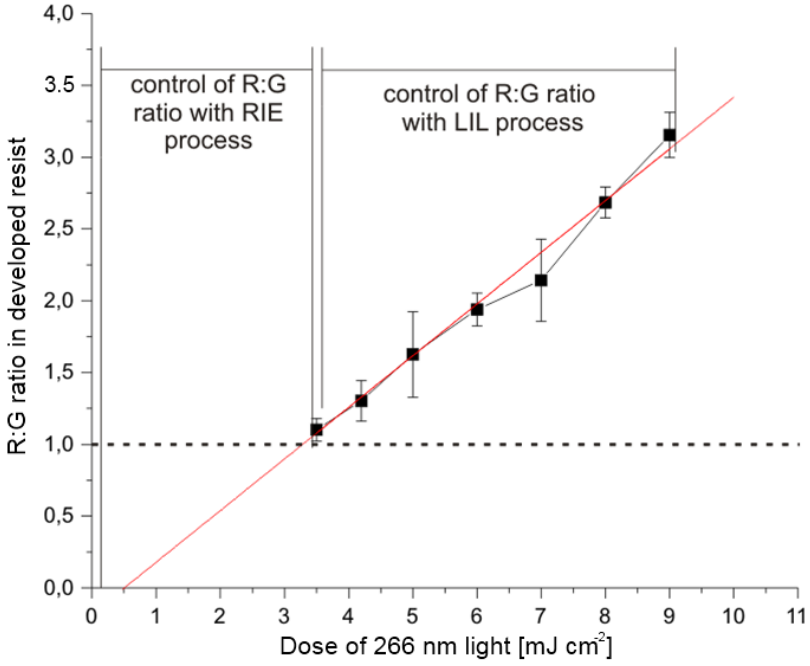

Figure 7. Influence of dose on $R_{R/G}$ in negative photoresist. The red line is a linear fit to the obtained points. Measurement points were obtained from analysis of SEM micrographs of developed resist of the same pitch when different radiation doses were used. The figure suggests that $R_{R/G}$ can be controlled in two ways: by dose and by RIE.

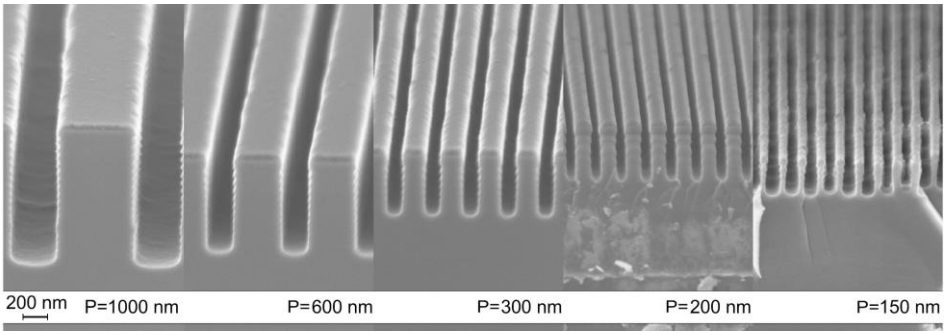

Figure 8. Overview of silicon nanostructures created using negative photoresist and a combined etching method. Scaling of the pattern period from 1 μm down to 150 nm. Here, aspect ratio ($R_{H/G}$) is 4.24 ± 0.92 across the different periods, the values are estimated from

the micrographs. As described previously the various pattern periods emerged from the angle of exposure in the experiment. Exposure parameters in LIL and etching times for RIE as well as cryo-DRIE, respectively are A) exposure at 7.6°, RIE: 21 s, cryo-DRIE: 72 s ; B) exposure at 12.8°, RIE: 17 s, cryo-DRIE: 44 s ; C) exposure at 26.3°, RIE: 14 s, cryo-DRIE: 30 s ; D) exposure at 41.6°, RIE: 12 s, cryo-DRIE: 15 s ; E) exposure at 62.4°, RIE: 10 s, cryo-DRIE: 14 s. The exposure dose was 4.5 mJ cm^{-2} for all structures.

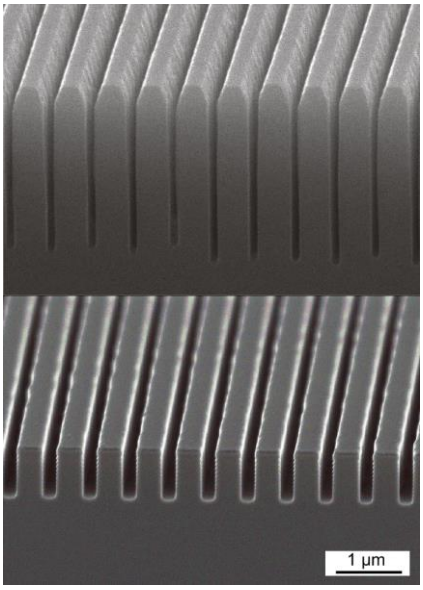

Figure 9. Micrograph showing result of tuning the ridge-to-groove aspect ratio. The upper structure was etched using cryogenic deep reactive ion etching only, resulting in a high aspect ratio of 25 for the trenches. The lower structure was etched with a combination of parallel plate RIE and a subsequent cryogenic deep reactive ion etching step in order to tune the ridge-to-groove width ratio ($R_{R/G}$) and the height-to-groove width ratio ($R_{H/G}$) independently, here, yielding an $R_{R/G}$ value of approximately 3.6 estimated from the figure

2.3.2. Characterization of the nanostructure uniformity

To investigate the influence of the pattern on cellular behavior, it is essential to guarantee uniform nanostructures homogeneously filling the complete bottom of the used culture dish with structure. The findings of this study provide such structures, hence facilitating both qualitative and quantitative cellular studies.

The lateral sizes of the structures were measured using a graphical analysis of the Atomic Force Microscope (AFM) scans. Although the AFM plot intensity generally correlates with the structure height, accurate height parameters were obtained by a graphical analysis of the calibrated High Resolution Scanning Electron Micrographs (HRSEM), due to the fact that the AFM tip cannot reach the bottom of the nanogrooves. In all AFM investigations the derivative function method was used (see experimental section for details). This method is based on an analysis of the grayscale intensity of the image (Figure 5 A). For the five molds produced by RIE only (Figure 6) the measured dimensional parameters are summarized in Table 3.

Table 3. Overview of produced structure sizes and parameters. All dimensions were obtained using AFM or HRSEM picture analysis; surface area increase was calculated for ideal mathematical model with assumptions that structure is created of planes.

Nanostructure pitch[nm] (convention)	Ridge [nm]	Groove [nm]	Height [nm]	Surface area increase (calculated)
150	71 ± 5	77 ± 6	32,7 ± 2	44 %
200	135 ± 3	82 ± 3	52 ± 3	48 %
300	175 ± 5	130 ± 8	49 ± 2	32 %
600	318 ± 16	305 ± 8	122 ± 10	39 %
1000	536 ± 10	453 ± 17	158 ± 10	32 %

The relative increase of surface area resulting from the introduction of the nanostructure was calculated against an idealized flat surface. Also the values for the increase of the surface area for a titanium surface treated with methods commonly used in the preparation of implants, i.e. etching and powder blasting, were contemplated by AFM yielding an increase of 38 % for powder blasted surfaces and 32 % for chemically etched surfaces [1, 21]. With the selected process, here, the uniformity of the structure, defined by the width of the ridge being accurate within an error of less than 5 % for positive resist is preserved over a

distance of more than 4 cm from the wafer edge (Figure 5 B). For negative resist the uniformity is higher and is preserved within an error of 6 % over a distance of more than 8 cm from the wafer edge for the same structure pitch. The fluctuations in lateral size are caused by a spatial variation of intensity in exposure during the LIL process, for which positive resist is intrinsically more sensitive than negative tone resist. Other influential parameters might be: spatially non-uniform light source, small defects in the reflecting mirror in the Lloyd's interference setup, or air turbulence during exposure or mechanical vibrations. Figure 5 B and C depict data from a nanostructure with a 200 nm period measured after the RIE process (see for reference of the process step Figure 3 C). For the other periods derived with positive resist, the usable uniform area varies slightly but in all cases it is above a value of 10 cm^2. Using the positive resist as a mask in SF_6:O_2 plasma chemistry only, $R_{H/G}$ varies with etching time and in terms of measurements of bioactivity, this parameter may be important. One can introduce the ratio of height-to-groove width either as a constant or as a variable parameter during biological studies. Here, we aimed at a constant ridge-to-groove width ratio of 1:1, realizing $R_{R/G}$ equal to 1.23 ± 0.29 while initially accepting that the selected etching process delivers variations in height for the five molds with an average height-to-groove width ratio of 0.43 ± 0.11. Of course, an increase in height will also increase the height-to-groove width ratio and consequently will lead to an increase in surface area, too. From the scanning electron micrographs in Figure 8for the structures derived from the high aspect ratio negative resist and a combined etching process R, G and H can be estimated. From the obtained values is is concluded that the combination of RIE and cryo-DRIE results in an approximately 10-fold increase of the $R_{H/G}$ value. The value increases from 0.43 for RIE only to 4.24 in the combined RIE-cryo-DRIE process with $R_{R/G}$ yielding an average value of 1.63 ± 0.26 for the different periods. This deviates from our intended ridge-to-groove width of 1:1. So far, it is not known, up to which maximum aspect ratio or minimal lateral features size it will be still possible to replicate the silicon features into PS by simple casting. These dimensions, however, will require

further fine-tuning during the biological response studies. In addition to replication by casting, the same dimensionally controlled molds can be utilized for nanoimprint lithography in the patterning process by direct etching of alternative bio-substrates (chapter: Titanium nanofabrication).

2.3.3. Evaluation of nanostructure bioactivity

The combined etching process allows further optimization of geometrical dimensions. Biological studies that evaluate if and how these geometrical parameters are linked to a specific biological response are reported by our group elsewhere [12]. To establish this bio-test platform technology, we demonstrate here, a fibroblast cytotoxicity model. From the first series of well characterized silicon molds (Figure 6) nanostructured PS slabs were replicated by solvent casting. These slabs were subsequently exposed to fibroblasts (for details see experimental section). The nanostructured slabs are evaluated in reference to flat tissue culture PS slabs. Both types of PS show proliferation of cells. During cell proliferation on nanostructured PS the fibroblasts stretch along the ridge-groove pattern (Figure 10) demonstrating bioactivity of the artificially generated features. The cell-nanostructure alignment decreases with decreasing pattern period. Despite being stretched, cells cultured on substrates with a period smaller than 300 nm (Figure 10 C) did not show a significant alignment to the grooves. These observations confirm the investigations on small nanostructure field sizes previously obtained by our group [12]. A separate study utilizing the large-area nanostructured silicon templates to investigate osteoblast behavior including morphology and gene expression is beyond this work, which is mainly concerned with the fabrication technology of molds. Further bio-related results are presented in chapter 6 of this thesis.

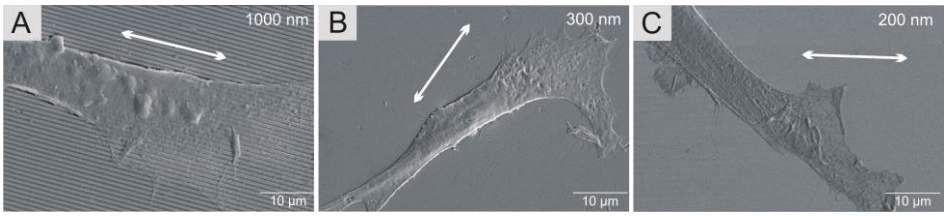

Figure 10. Micrographs of fibroblasts cultured on nanostructured PS obtained by polymer replication from the silicon molds (low aspect ratio) fabricated in this study with a pattern period of: A) 1000 nm, B) 300 nm, and C) 200 nm period. Arrows indicate the groove direction. At a pattern period of 200 nm and below the fibroblast alignment to the grooves becomes less dominant.

2.4. Conclusion

In summary, to understand the nature of enhanced bioactivity due to topology it is required to perform systematic, parameterized and statistical biological studies on large area, uniform substrates. Silicon nanomachining based on established LIL and RIE provides a method by means of which highly uniform molds for the repetitive fabrication of large area nanostructured bioactive surfaces can be guaranteed. The process optimization here led to control of ridge-to-groove width ratio and scaling the pattern period down from 1000 nm to 150 nm with a minimal ridge size of 71 ± 5 nm at a period of 150 nm at a relatively low aspect ratio of approximately 0.4. It has been demonstrated that fibroblasts show alignment to this topology along the direction of the ridge-groove pattern with a cut-off at a period of 300 nm. Below this period, no specific orientation of cells is observed. Optimizing the sequence of the fabrication process led to a method involving negative resist LIL and combination of RIE and cryo-DRIE towards independently scalable dimensions of the nanostructure geometry as suggested Figure 2 mainly with the gain to increase AR=H/G by a factor of ca. 10. These molds are now available to continue systematic investigations exploring different cell lines. To unravel the real driving force behind bioactivity it is important to collect next to the

morphological data also gene/protein expression data and other cellular biofunctioning indicators for which this mold fabrication technology provides an essential experimental platform.

1 Agheli H and Sutherland D S Nanofabrication of polymer surfaces utilizing colloidal lithography and ion etching *IEEE Transactions on Nanobioscience* **5,** 9-14 (2006)

2 Braceras I, Alava J I, Goikoetxea L, de Maeztu M A and Onate J I Interaction of engineered surfaces with the living world: Ion implantation vs. osseointegration *Surface and Coatings Technology* **201,** 8091-8 (2007)

3 Choi C H, Hagvall S H, Wu B M, Dunn J C Y, Beygui R E and Kim C J Cell interaction with three-dimensional sharp-tip nanotopography *Biomaterials* **28,** 1672-9 (2007)

4 Cochran D L, Nummikoski P V, Higginbottom F L, Hermann J S, Makins S R and Buser D Evaluation of an endosseous titanium implant with a sandblasted and acid-etched surface in the canine mandible: Radiographic results *Clinical Oral Implants Research* **7,** 240-52 (1996)

5 Cooper L F Biologic determinants of bone formation for osseointegration: Clues for future clinical improvements *The Journal of Prosthetic Dentistry* **80,** 439-49 (1998)

6 Curtis A S, Dalby M and Gadegaard N Cell signaling arising from nanotopography: implications for nanomedical devices *Nanomedicine (London, England)* **1,** 67-72 (2006)

7 Curtis A S G, Casey B, Gallagher J O, Pasqui D, Wood M A and Wilkinson C D W Substratum nanotopography and the adhesion of biological cells. Are symmetry or regularity of nanotopography important? *Biophysical Chemistry* **94,** 275-83 (2001)

8 Dalby M J, Giannaras D, Riehle M O, Gadegaard N, Affrossman S and Curtis A S G Rapid fibroblast adhesion to 27 nm high polymer demixed nano-topography *Biomaterials* **25,** 77-83 (2004)

9 Flemming R G, Murphy C J, Abrams G A, Goodman S L and Nealey P F 1999 Effects of synthetic micro- and nano-structured surfaces on cell behavior *Biomaterials* **20** 573-88

10 Freshney R *Culture of animal cells: a multimedia guide.* New York, USA.: Wiley-Liss inc. (2000)

11 Fu J, Hu Y, Guo Z, Zhang Y, Hao Y and Li S Effect of surface micro-topography of titanium material on the behaviors of rabbit osteoblast in vitro *Applied Surface Science* **255,** 286-9 (2008)

12 Lamers E, Domanski M, te Riet J, McKerr G, O'Hagan B M, Barnes C A, Peto L, van Delft F C M J M, Luttge R., Winnubst A J A, Gardeniers J G E, Jansen J A and Walboomers X F 2009 Nanogrooved substrates influence osteoblast-like cell behavior and extracellular matrix deposition, *Nano Letters in submission*

13 Loesberg W A, te Riet J, van Delft F C M J M, Schon P, Figdor C G, Speller S, van Loon J J W A, Walboomers X F and Jansen J A The threshold at which substrate nanogroove dimensions may influence fibroblast alignment and adhesion *Biomaterials* **28,** 3944-51 (2007)

14 Martínez E, Engel E, Planell J A and Samitier J Effects of artificial micro- and nano-structured surfaces on cell behaviour *Annals of Anatom* **191**, 126-135 (2009)

15 Meredith D O, Riehle M O, Curtis A S G and Richards R G Is surface chemical composition important for orthopaedic implant materials? *Journal of Materials Science: Materials in Medicine* **18,** 405-413 (2007)

16 Murillo R, van Wolferen H A, Abelmann L and Lodder J C Fabrication of patterned magnetic nanodots by laser interference lithography *Microelectronic Engineering* **78-79,** 260-5 (2005)

17 Prodan L, Euser T G, Wolferen H A G M v, Bostan C, Ridder R M d, Beigang R, Boller K J and Kuipers L Large-area two-dimensional silicon photonic crystals for infrared light fabricated with laser interference lithography *Nanotechnology* 639 (2004)

18 Rasband W S R, ImageJ, U.S. National Institutes of Health, Bethesda, MD, USA (2007) http://rsb.info.nih.gov/ij/index.html (Accessed June 2011).

19 Stanford C M Surface modifications of dental implants *Australian Dental Journal* **53,** (2008)

20 Van Soest F J, Van Wolferen H A G M, Hoekstra H J W M, De Ridder R M, Worhoff K and Lambeck P V Laser interference lithography with highly accurate interferometric alignment *Japanese Journal of Applied Physics, Part 1: Regular Papers and Short Notes and Review Papers* **44,** 6568-70 (2005)

21 Yim E K F and Leong K W Significance of synthetic nanostructures in dictating cellular response *Nanomedicine: Nanotechnology, Biology and Medicine* **1,** 10-21 (2005)

3.

CERAMIC MICROMOLDING USING MICROFABRICATED SILICON MOLDS

Abstract

A process of micromolding delivering micro- and nanopatterned ceramic surfaces was investigated in this work. To create the desired structures, tape casting of a ceramic slurry on microfabricated silicon mold masters with anti-sticking layers was used. Several tape casting ceramic slurry compositions were tested to evaluate the feasibility of transferring micro- and nanofeatures. Used ceramics were alpha alumina (α-Al_2O_3) and yttria stabilized zirconia (YSZ). Three types of polymeric binders for the green tape (PVB, PES, PVP) were investigated using three different solvents (ethanol, n-methyl-pyrrolidone, water). Well-defined features in shapes of wells with diameters down to 2.4 μm and a depth of 10 μm and pillars with diameters down to 1.7 μm and a height of 3 μm were obtained. Morphology, grain size and porosity of the sintered bodies were characterized. Finally, fibroblast cells were cultured on the surfaces in order to observe their growth morphology under influence of the microstructures.[1]

[1] *Part of this chapter was used for filing patent "Integrated microneedle array and method for manufacturing thereof"*

3.1. Introduction

Historically, ceramic biomaterials were anticipated to function as an inert material in the body. Nowadays the emphasis is more on applying these materials to create a bioactive scaffold that stimulates the construction of a well-functioning bone-implant interface [1-7]. A specific combination of micro- and nanotopography might be required to stimulate osteoinduction or to cause mechanisms like interlocking in the body by mechanical anchoring and stimulating cells to produce a higher density of focal adhesions [8-10]. Naturally occurring nanometer range stochastic surface features emerge from the intrinsic grain nature of the material. In addition to the natural nanostructure, in this study we will define micro-pillars or micro-wells at the green tape level by using microfabricated silicon as casting mold. Ceramic materials used here are yttria stabilized zirconia (YSZ) and alpha alumina (α-Al_2O_3), which have a long history as implant materials, both as a bulk material and as a coating [11,12]. Such inert oxide ceramics are generally used in applications where good mechanical and tribological, characteristics, which are unique for this group of materials, are required [8,9,11,13,14].

The applied method of tape casting gives the possibility to create an implant surface carrying a combination of micro- and nanofeatures. By tuning the slurry parameters, it also allows us to obtain the desired product morphology in terms of porosity and mechanical strength [15-19]. We evaluated three types of casting slurries, with different binders and solvents, and five types of microfabricated silicon mold masters with different feature sizes (10, 5, 2, and 0.5 μm). The slurries were adapted directly from either tape casting methodology [15], hollow porous fibers fabrication [20] or porous membrane support fabrication method [19]. The microfeatures in silicon mold masters consisted of pillar- or well-like structures arranged in a trigonal lattice. To evaluate the dimensional limits of pattern transfer, casting was also performed on submicrometer silicon features with ridge and groove shapes. After casting, the green tapes were either air-dried or the solvent was exchanged with non-solvent. Although our research

focused on YSZ and α-Al_2O_3, we would like to stress though that any type of ceramic material can be structured utilizing the versatile method presented in this work. The resulting green tapes were sintered and characterized with SEM and densitometry. Finally, the produced size-resolved surface topographies were used in biological experiments, from which it was concluded that fibroblast cells respond to surface topography by altering their morphology.

3.2. Materials and methods

3.2.1. Mold masters for tape casting

Masters were microfabricated using UV lithography for feature dimensions of 10, 5, 2 μm or Laser Interference Lithography (LIL) for 0.5 μm features (for a detailed description of the LIL process see chapter 2 of this thesis). Subsequently the pattern was transferred into silicon using reactive ion etching. In brief the fabrication of mold masters was conducted as follows: a 100 mm, standard {100}, p-type, one side polished silicon wafer (Okmetic, Finland) was spin-coated with positive i-line photo resist (OiR 907/17, Fujifilm) and subsequently exposed through a prefabricated chromium-on-glass mask using UV optical lithography. The latent structure was developed in OPD developer (Fujifilm). RIE etching with a Bosch-type process (Adixen AMS100SE, Alcatel) was conducted, followed by standard cleaning in fuming nitric acid for 10 min. Two types of anti-adhesion procedures were followed. Molds, used for water or ethanol based slurries, were sputtered with a thin layer of gold (~200 nm) using an argon plasma sputtering system (Sputterke, TCO). For the phase inversion system, utilizing NMP-based slurries, a thin layer of carbon fluorides was deposited using plasma enhanced chemical vapor deposition (PECVD) using C_4F_8 (Adixen 100 SE, Alcatel).

3.2.2. Preparation of ceramic slurries

The starting ceramic powders were either α-Al_2O_3 (Sumitomo AKP 30, particle size range 0.3-0.5 μm, surface area typically 5-10 $m^2\ g^{-1}$) or yttria stabilized

zirconia (Tosoh Zirconia, TZ-8YS, particle size range 0.05-0.08 μm, surface area typically 5-9 $m^2 g^{-1}$). Three types of tape casting slurries were prepared: water based (referred to as PVP-H_2O), ethanol based (referred to as PVB-EtOH) and n-methylpyrrolidone based (referred to as PES-NMP). The slurry compositions are summarized in Table 4.

Table 4. Composition of the tape casting slurries used for micromolding [weight %]

Composition	PVB - Ethanol based slurry (PVB-EtOH)		PVP-Water based slurry (PVP-H_2O)		PES –n-methyl-pyrrolidone based slurry (PES-NMP)	
Viscosity of slurry	~2500 mPa		~6000 mPa		~9500 mPa	
Ceramic powder	α-Al_2O_3	42.9 %	α-Al_2O_3	46.3 %	8mol% Y_2O_3 stabilized ZrO_2	50.7 %
Binder	polyvinyl butyral, PVB [b]	6.4 %	polyvinylpyrrolidone (PVP)	4.5 %	polyethersulfone PES [b]	4.9 %
Solvent	Ethanol	46.6 %	0.02 M Nitric acid in H_2O	46.2 %	n-methyl-2-pyrrolidone	44.4 %
Dispersant	Solsperse 20000 [a]	0.8 %	Disperbyk 194 [c]	3 %		
Plasticizer	butyl benzyl phthalate [b]	2.8 %				
Dispersant	Menhaden fish oil [a]	0.5 %				

[a] The Lubrizol Corporation, USA [b] Richard E. Mistler, Inc., USA [c] BYK-Chemie GmbH, Germany

3.2.2.1. Organic solvent based slurries

For preparation of ethanol and NMP based tape casting slurries two types of polymeric binders were used: PVB and PES respectively (polyvinyl butyral, Tapecasting Warehouse INC. and polyethersulfone, Goodfellow Cambridge Limited). Slurry preparation consisted of dissolving an oven-dried polymer (50°C / 24h) in solvent. For PVB and for PES 99.9 % ethanol (Sigma Aldrich) and 99.9 % n-methylpyrrolidone (Sigma Aldrich) were used, respectively. The polymer-solvent mixtures were stirred on a roller bench for mixing during 3

hours using 1 cm diameter alumina balls. Next, the amounts of tape casting additives as given in Table 4 were added. Additives used in PVB-EtOH based slurry were: Menhaden Fish Oil, Butyl Benzyl Phthalate as a plasticizer (Richard E. Mistler, Inc.) and Solsperse 20000 as a dispersant (The Lubrizol Corporation). For the PES-NMP based slurry no dispersing or plasticizing additives were used. The solutions were mixed for one more hour. Oven dried (60°C, 24h) alumina or zirconia powders were added to the polymer-solvent solutions and the slurries were mixed on a roller bench for another 24 hours. Finally, slurries were degassed in an ultrasonic bath for 20 minutes. The composition of the slurries in weight percentages can be found in Table 4.

3.2.2.2. Water based slurry

To create the water-based slurry, the alumina ceramic powder was dispersed in 0.02 M aqueous nitric acid solution. The ratio powder to water was 1:1 (w/w). Next, the suspension was sonicated using a horn sonicator for 7 minutes (S-250, Branson Ultrasonic). Finally polyvinylpyrrolidone polymer (PVP, Aldrich, M_w=1300000) and dispersant Disperbyk-194 (BYK-Chemie GmbH) were added and the suspension was mixed for 4 hours on a roller bench.

3.2.3. Tape casting on silicon masters and sintering

A thin (1-3 mm) layer of ceramic slurry was deposited on the silicon master by using a doctor's blade. Next, depending on the slurry type, green tapes were slowly air dried in ethanol-vapour rich environment (for PVB-Ethanol based slurry) or in moist air (for PVP-water slurry). A solvent-rich environment or moist environment was obtained by closing the sample together with a Petri dish filled with either ethanol or water in a $10 \times 10 \times 5$ cm^3 plastic box with a 0.5×0.5 cm^2 hole that causes slow diffusion-driven air-solvent exchange. After drying, the green tapes were manually separated from the masters. The PES-NMP based green tape was prepared using a phase inversion method. The slurry was casted on the mold master and subsequently immersed in water to cause liquid-solid phase separation. This solvent / non-solvent exchange in the slurry

causes solidification of PES [29, 30]. Finally, the samples were manually removed from the master, and dried for 72 h. The dried green tapes were cut in 5 × 5 mm^2 pieces and sintered in a tube furnace (Vectstar, type 6Z) at 1500°C. Sintering profiles were designed as follows: heating at 1°C per minute to 400°C, binder burn-out at 400°C for 1 hour, heating up to 1500°C, sintering for 4 hours, and finally cooling down to room temperature at 3°C per minute.

3.2.4. Density and grain size measurement

For the sintered ceramics grain size analysis was performed, utilizing the line intercept method for analysis of SEM scans [20]. Sintered specimens were polished using diamond polishing media (Cameo method, LamPlan). Next specimens were thermally etched in a tube furnace by heating up to 1230°C and keeping the specimens at that temperature for 45 min in order to reveal the grains. After this treatment both zirconia and alumina specimen were sputter coated with a thin gold layer and investigated by scanning electron microscopy (SEM). Image analysis utilizing ImageJ software was used to measure the average grain size with line intercept method (Mendelsohn method).

Density was measured with the Archimedes' method in mercury using a laboratory scale [21].

The detailed morphology was investigated with SEM. All SEM scans included in this work were made on Jeol JSM-5610LV, Jeol 6310 SEM or Philips XL 30 ESEM-FEG electron microscopes.

3.2.5. Cell culture

Rat dermal fibroblasts (RDF) were obtained from the ventral skin of male Wistar rats as described by Freshney [22]. Cells were cultured in an α-MEM medium (Invitrogen) supplemented with 10 % Fetal Calf serum (FCS) and gentamicin (50 μg ml^{-1}). Cell culture experiments were performed at the 6^{th} or 7^{th} culture passage. Before transferring the cells to the substrates, cells were detached from the culture flask using trypsin/EDTA (0.25 % w/v trypsin/0.02 % EDTA) (Invitrogen) and concentrated by centrifugation at 1500 rpm for 5

minutes. Subsequently, cells were resuspended in the culture medium, quantified using a Coulter® counter (Beckman Coulter Inc., Fullerton, CA, USA) and seeded at a density of 1×10^4 cells cm^{-2}. Rat dermal fibroblast (RDF) cell culture assays were performed on well- and pillar-like structures of α-alumina substrates acquired from PVB-EtOH slurries in the time of 2 days of seeding. Thereafter cells were fixed in 2 % (w/v) glutaraldehyde in 0.1 M sodium-cacodylate, dehydrated in a graded series of ethanol (from 70 % up to 100 %), and dried to air in tetramethylsilane. The substrates were sputter coated with gold and observed using a Jeol 6310 SEM.

3.3. Results

3.3.1. Silicon mold masters

It is clearly visible that uniform patterns can be obtained with the microfabrication techniques used in this work. SEM micrographs of representative samples of silicon mold masters with features of well- and pillar-like structures delivered by UV lithography and ridge-groove type of structures delivered by LIL are presented in Figure 11.

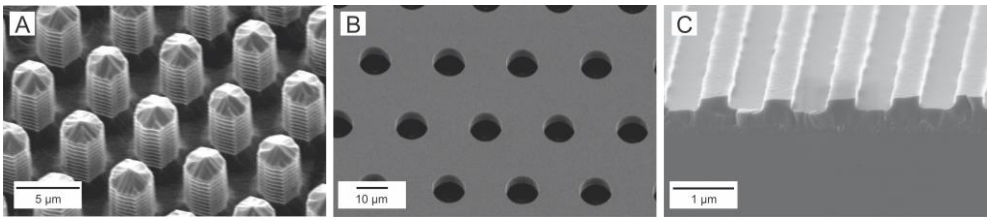

Figure 11. Scanning electron micrographs of silicon mold masters fabricated with UV lithography (A, B), LIL (C) lithography and subsequent RIE: A) 2 μm pillar structure in silicon; B) 10 μm well structure etched in silicon; C) 0.5 μm ridges in silicon.

3.3.2. Micromolded ceramics

3.3.2.1. Morphology

After tape casting the green tapes were examined with SEM in the secondary electron imaging mode. In the acquired micrographs the dispersed particles of ceramics suspended in the polymer matrix could be observed (Figure 12). No large agglomerates of ceramic particles were observed for all green tapes. This suggests that the dispersion stabilization by either polymer additives or pH is successful.. The PVB-EtOH and PES-NMP based slurries gave robust easy to handle green tapes, facilitating further shaping (i.e. in implant shape) whereas PVP-H_2O based slurry gave mechanically brittle green tapes.

After sintering, the smallest transferred features were approximately 1.7 μm diameter pillars (master dimension 1.9 μm), and 2.4 μm-diameter wells (master dimension 2.1 μm). The features were obtained from all three tape-cast slurries.

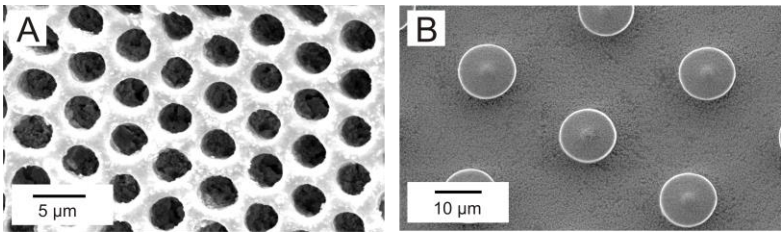

Figure 12. Green tapes with visible polymer-ceramic composite before sintering A) 2 μm well structure created in ZrO_2 with PES-NMP slurry; B) 10 μm pillar structure created in Al_2O_3 with PVP-H_2O slurry.

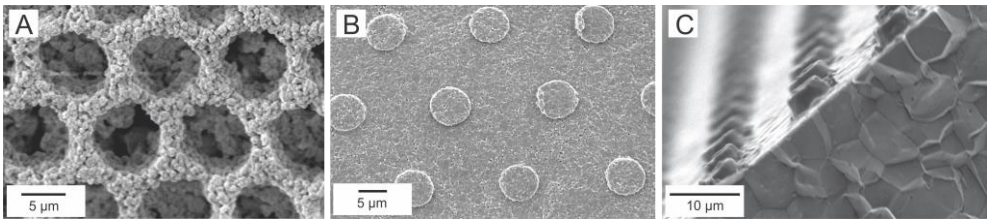

Figure 13. Sintered in 1500°C ceramic bodies. A) 6 µm well structure created in ZrO2 with PES-NMP slurry; B) 8 µm well structure created in Al2O3 with PVB-EtOH slurry. C) Al2O3 ¬PVP-H2O slurry delivered structures.

3.3.2.2. Density

After sintering, the ceramic bodies were again observed with SEM (Figure 13). Both, for Al_2O_3 and ZrO_2 (PVB-EtOH and PES-NMP respectively) based ceramics the grain structure is visible. In case of alumina specimens, this structure can only be observed in bulk material (after cross sectioning) and cannot be seen on the surface of sintered material which appears a non-porous structure (Figure 13 B). In case of the Al_2O_3 PVP-H_2O based slurry, sintering of green tape resulted in a dense virtually non-porous body. The porosity of sintered bodies was measured with the Archimedes' method and ranged from the lowest density for the NMP-PES derived system (88 % theoretical) via PVB-EtOH derived (96 % theoretical) to the high-density PVP-H_2O-derived system (99 % of theoretical density values of alumina and zirconia of 3.97 g cm^{-3} and 5.68 g cm^{-3}, respectively).

3.3.2.3. Grain Size

For the PVB-EtOH and PVP-H_2O derived alumina ceramics significant grain growth can be observed, where the largest grains were obtained for the PVP-H_2O based slurry. The initial Al_2O_3 powder had a grain size of 0.3 - 0.5 µm. In the sintered body grains have grown to approximately 2.4 µm in diameter for the PVP-H_2O slurry and 1.3 µm in the green tapes obtained with the PVB-EtOH slurry. Morphology measurements are summarized in Table 5.

In case of zirconia powder the growth was also significant, the measured grain size in the sintered body was 0.48 μm (0.05-0.08 μm initially). Grain growth during sintering occurred to be the main limiting factor for copying structures with critical dimensions smaller than $6\times D_{grain}$ (Figure 14).

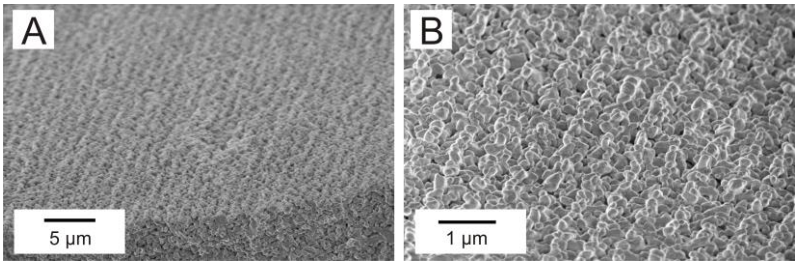

Figure 14. Surface of nanopatterned sintered zirconia shaped with 0.5 μm silicon mold master, barely visible ridges diminish due to the grain size.

Table 5. Parameters of green tape and sintered ceramics.

Composition	Volume ratios in green state		Porosity of sintered body	Grain size in sintered body	Shrinkage of sintered ceramic ($D_{mold}/D_{ceramics}$)
	Ceramics	Binder			
Al_2O_3 PVB – EtOH	70.4 %	29.6 %	96 %	1.3 μm	0.92
Al_2O_3 PVP – H_2O	76.9 %	23.0 %	99 %	2.4 μm	0.77
ZrO_2 PES – n-methyl-pyrrolidone	69.4 %	30.6 %	88 %	0.48 μm	0.66

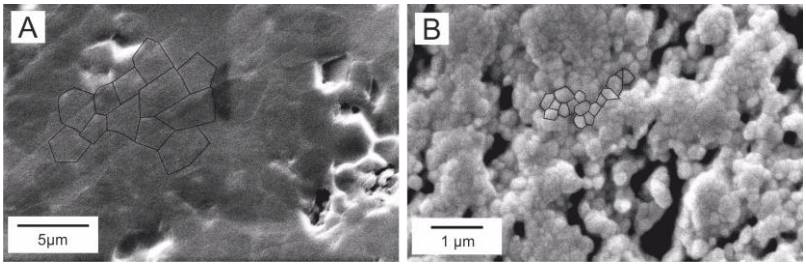

Figure 15. The ceramic samples after sintering. Polishing and temperature etching were used to unveil grain boundaries. A) surface with outlined grain of alumina; B) surface with outlined grain of zirconia.

3.3.3. Cell culturing tests and results

On flat alumina controls, RDFs were well-spread and formed normal spindle and multipolar cell morphologies with short filopodia. However, in contrast to cells cultured on standard cell culture polystyrene substrates (not shown), many focal contacts were visible at the cell edges (Figure 16 A) specifically adhering to the nanorough features on the substrate surface. RDF cells that had been cultured on the micropillar substrates were stretched in a similar fashion as on the smooth substrates, however filopodias of the cells had tendency to surround the micropillars. These cells also exhibited large extensions. Cell bodies covered the pillars and descended down to the substrate surface around the pillars. The larger cell extensions clearly appeared to be guided by the pillars (Figure 16 B, C). No apparent differences in cell morphology were observed between all structure sizes the cells were cultured on.

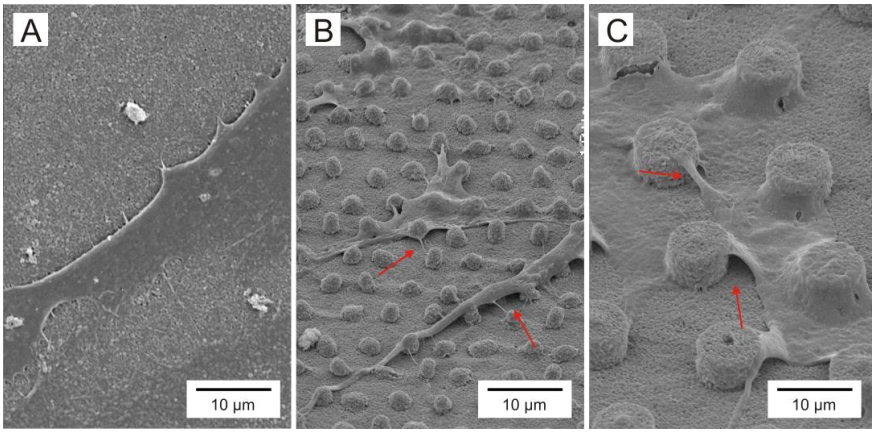

Figure 16. SEM micrographs of fibroblasts (RDF) cultured on micropatterned substrates: A) Flat alumina, B) 1.7 µm pillars; C) 8.6 µm pillars. The red arrows indicate alternations in morphology of fibroblast caused by microstructure.

3.4. Conclusions

In this work pattern, transfer into ceramics was evaluated by tape casting from micromachined silicon molds. Silicon micromachining is based on

photolithography and silicon dry etching. This process provides a large flexibility in the design of microstructural layouts. Here, we have used molds with pillar- and well-like microstructures in a trigonal lattice arrangement as well as submicron nanogrooves. Tape casting of the ceramic slurry on the surface of the silicon mold was used to replicate the silicon patterns in ceramics. It was found that all three investigated slurry systems were able to replicate structures from the mold master down to 2 μm. The sintered ceramics from different casting systems differ in density and definition of microfeatures. Preventing the grain growth during sintering could lead to more uniform and regular shapes and structures smaller than the mentioned limit. Different structural shrinkage occurred with different ceramic formulations. In general, the most useful replication copies were obtained with Al_2O_3 PVB-EtOH slurry. For this formulation, the shrinking during sintering was lowest and the critical dimension of microfeatures changed the least (Table 5). The Al_2O_3 PVP-H_2O slurry gave the ceramic bodies with the highest density and the ZrO_2 NMP-PES gave the structures with the smallest grain size (but note that the initial grain size was also smaller).

Finally, preliminary rat dermal fibroblasts were cultured on the Al_2O_3 PVP-H_2O delivered microstructures. The findings from these cell cultures suggest that cells mainly react to micro pillars by alterations of filopodia sensing. The cells recognize the patterns and respond by adapting a more stretched morphology including the formation of filopodia showing intimate contact with the surface features. The fact that alumina substrates possess an inherent nanoroughness can also influence cell behavior. Osteoblasts and fibroblasts have already been shown to respond to nanoroughness by increased filopodia formation and increased adhesive strength [23-25]. In accordance with these studies, the number of filopodia also appeared to be increased on the currently tested alumina substrates. The observed phenomenon associated with such an event is a localization of F-actin, stress fibers and focal adhesions, marking the site of the discontinuities, edges, underlying the cell. The full effect of this phenomenon

on an individual cell phenotype and differentiation pathway has yet to be deciphered. [22, 23]

1 Balasundaram, G., Sato, M. & Webster, T. J. Using hydroxyapatite nanoparticles and decreased crystallinity to promote osteoblast adhesion similar to functionalizing with RGD. *Biomaterials* **27**, 2798-2805 (2006).

2 Bruckmann, C., Walboomers, X. F., Matsuzaka, K. & Jansen, J. A. Periodontal ligament and gingival fibroblast adhesion to dentin-like textured surfaces. *Biomaterials* **26**, 339-346 (2005).

3 Dalby, M. J., Riehle, M. O., Yarwood, S. J., Wilkinson, C. D. W. & Curtis, A. S. G. Nucleus alignment and cell signaling in fibroblasts: response to a micro-grooved topography. *Experimental Cell Research* **284**, 272-280 (2003).

4 Eisenbarth, E., Meyle, J., Nachtigall, W. & Breme, J. Influence of the surface structure of titanium materials on the adhesion of fibroblasts. *Biomaterials* **17**, 1399-1403 (1996).

5 Heydarkhan-Hagvall, S., Choi, C.-H., Dunn, J., Heydarkhan, S., Schenke-Layland, K., MacLellan, W. R. & Beygui, R. E. Influence of Systematically Varied Nano-Scale Topography on Cell Morphology and Adhesion. *Cell Communication & Adhesion* **14**, 181 - 194 (2007).

6 Parker, J. A. T. C., Walboomers, X. F., Von den Hoff, J. W., Maltha, J. C. & Jansen, J. A. The effect of bone anchoring and micro-grooves on the soft tissue reaction to implants. *Biomaterials* **23**, 3887-3896 (2002).

7 Pfeiffer, F., Herzog, B., Kern, D., Scheideler, L., Geis-Gerstorfer, J. & Wolburg, H. Cell reactions to microstructured implant surfaces. *Microelectronic Engineering* **67-68**, 913-922 (2003).

8 Best, S. M., Porter, A. E., Thian, E. S. & Huang, J. Bioceramics: Past, present and for the future. *Journal of the European Ceramic Society* **28**, 1319-1327 (2008).

9 Larry, L. H. Bioceramics: From Concept to Clinic. *Journal of the American Ceramic Society* **74**, 1487-1510 (1991).

10 Lemons, J. E. Ceramics: Past, present, and future. *Bone* **19**, S121-S128 (1996).

11 Zhou, Y. S., Ikeuchi, K. & Ohashi, M. Comparison of the friction properties of four ceramic materials for joint replacements. *Wear* **210**, 171-177 (1997).

12 Rieu, J. Ceramic formation on metallic surfaces (ceramization) for medical applications. *Clinical Materials* **12**, 227-235 (1993).

13 Kusaka, J., Takashima, K., Yamane, D. & Ikeuchi, K. Fundamental study for all-ceramic artificial hip joint. *Wear* **225-229**, 734-742 (1999).

14 Zhou, Y. S., Ohashi, M. & Ikeuchi, K. Start up and steady state friction of alumina against alumina. *Wear* **210**, 112-119 (1997).

15 Young, A. C., Jane-Chyi, L., Tsung-Shou, Y. & Chian-Lii, C. Characteristics of tape casting slurries containing forsterite, PVB and organic solvent. *Materials Chemistry and Physics* **34**, 147-153 (1993).

16 Hu, J. M., Beck, R. G., Deng, T., Westervelt, R. M., Maranowski, K. D., Gossard, A. C. & Whitesides, G. M. Using soft lithography to fabricate GaAs/AlGaAs heterostructure field effect transistors. *Appl. Phys. Lett.* **71**, 2020-2022 (1997).

17 Schonholzer, U. P., Stutzmann, N., Tervoort, T. A., Smith, P. & Gauckler, L. J. Micropatterned ceramics by casting into polymer molds. *Journal of the American Ceramic Society* **85**, 1885-1887 (2002).

18 Treccani, L., Maiwald, M., Zöllmer, V., Busse, M., Grathwohl, G. & Rezwan, K. Antibacterial and Abrasion-Resistant Alumina Micropatterns. *Advanced Engineering Materials* **11**, B61-B66, (2009).

19 Lin, Y.-S. & Burggraaf, A. J. Preparation and Characterization of High-Temperature Thermally Stable Alumina Composite Membrane. *Journal of the American Ceramic Society* **74**, 2721-2721, (1991).

20 Liu, Y., Chen, O. Y., Wei, C. C. & Li, K. Preparation of yttria-stabilised zirconia (YSZ) hollow fibre membranes. *Desalination* **199**, 360-362, (2006).

21 Kwan, Y.-B. P. & Alcock, J. R. The impact of water impregnation method on the accuracy of open porosity measurements. *Journal of Materials Science* **37**, 2557-2561 (2002).

22 Freshney, R. (Wiley-Liss inc. , New York, USA, 2000).

23 Dalby, M. J., Berry, C. C., Riehle, M. O., Sutherland, D. S., Agheli, H. & Curtis, A. S. G. Attempted endocytosis of nano-environment produced by colloidal lithography by human fibroblasts. *Exp Cell Res* **295**, 387-394 (2004).

24 Mustafa, K., Oden, A., Wennerberg, A., Hultenby, K. & Arvidson, K. The influence of surface topography of ceramic abutments on the attachment and proliferation of human oral fibroblasts. *Biomaterials* **26**, 373-381 (2005).

25 Loesberg, W. A., te Riet, J., van Delft, F. C. M. J. M., Schön, P., Figdor, C. G., Speller, S., van Loon, J. J. W. A., Walboomers, X. F. & Jansen, J. A. The threshold at which substrate nanogroove dimensions may influence fibroblast alignment and adhesion. *Biomaterials* **28**, 3944-3951 (2007).

4.

NANOPATTERNING OF BULK TITANIUM BY NANOIMPRINT LITHOGRAPHY AND REACTIVE ION ETCHING

Abstract

Nanopatterns on titanium may enhance endosseous implant biofunctionality. To enable biological studies to proof this hypothesis, we developed a scalable method of fabricating nanogrooved titanium substrates. We define nanogrooves by nanoimprint lithography (NIL) and a subsequent pattern transfer to the surface of ASTM grade 2 bulk titanium applying a soft-mask for chlorine-based reactive ion etching (RIE). With respect to direct write lithographic techniques the method introduced here is fast and capable of delivering uniformly patterned areas at least 4 cm^2. A dedicated silicon stamp process has been designed to generate the required thickness of the soft-mask for the NIL-RIE pattern transfer. Stamps with pitch sizes from 1000 nm down to 300 nm were fabricated using laser interference lithography (LIL) and deep cryogenic silicon RIE. Although silicon nanomachining was proven to produce smaller pitch sizes of 200 nm and 150 nm, respectively, successful pattern transfer to titanium was only possible down to a pitch of 300 nm. Hence, the smallest nanogrooves have a width of 140 nm. An x-ray photoelectron spectroscopy study (XPS) showed that only very few contaminations arise from the fabrication process and a

cytotoxicity assay on the nanopatterned surfaces confirmed that the obtained nanogrooved titanium specimens are suitable for *in vivo* studies in implantology research.

4.1. Introduction

Upon the placement of an endosseous implantable biomaterial a wound is created, which can either provoke a wound healing response or a chronic inflammation, the latter leading to the clinical failure of an implant. In order to improve implant success rates much effort is placed in optimizing implants by changing the surface characteristics, most importantly the topography [1]. Recently, several groups have started to study the effects of nanoscale topographical surface characteristics to osteoblast-cells [2-4]. The rationale behind this is that it is thought to be beneficial for implant acceptance, if the implant surface mimics the natural extracellular matrix of bone, which is highly organized at the nanometric scale. Collagen-I, for example, is organized in a groove-like fibrillar structure with a spacing of 68 nm and 35 nm depth [5]. Bone crystals are embedded inside these structures forming a highly organized bone matrix. Following the above rationale, we recently studied the osteoblast response to nanoscale grooves and demonstrated that such topography promotes osteoblast alignment, differentiation and ECM-organization [4]. The previous study, however, was performed on polystyrene (PS) substrates, whereas titanium (Ti) is the commonly used high-load implant biomaterial. Therefore, the aim of the present study is to develop a reproducible fabrication method for nanoscale grooves in bulk Ti that is suitable for implantology. Generally well established and explored routes to obtain surface modification of Ti implants are: acid etching, grit blasting, mechanical roughening, plasma spraying, anodization or laser milling [6-12]. These surface treatments create either pore-like or pillar-like short range ordered surface structures. Figure 17 A-C illustrates these micro- and nanostructures with dimensions of a randomized distribution. The evaluation of surface roughness and the determination of the average

dimensions of these pores, pillars or grain diameters can be used to quantify and consequently compare the characteristic features from one surface preparation method to another. Relying on these types of randomly arranged nanostructures, however, it is difficult to distinguish unique geometrical stimuli for cell biology studies.

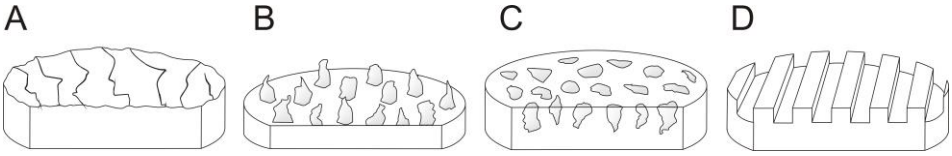

Figure 17. Schematic representation of possible nanometric topographical surface modifications; A) unmodified, naturally rough surface; B) surface with protrusions; C) pitted surface; D) surface with systematic topography alternations, as discussed in this study.

According to the potential that our previous experimental results on nanostructured polystyrene substrates showed, a nanogroove pattern (Figure 17 D) is selected for the modification of the Ti surfaces [4]. In previous studies elsewhere, it was demonstrated that Ti micromachining can be performed by using chlorinated plasma RIE techniques [13-17]. Reactively sputtered TiO_2 and thick layer photoresist (> 20 μm) were explored as masking materials in most of these cases. The nanopatterning of Ti has also been demonstrated by local anodic oxidation utilizing a scanning probe technique [18]. At the current state-of-the-art, the latter cannot be considered feasible for the fabrication of large-area samples required for biological studies. To obtain large-area samples fully covered with nanogrooves of systematically scalable dimensions, here, we describe the nanopatterning of ASTM grade 2 bulk Ti surfaces performed by thermal nanoimprint lithography (NIL) and reactive ion etching (RIE). The specific novelty in this work is the proof of concept that advanced scalable silicon nanomachining can be utilized to prepare NIL-stamps that allow an efficient route to create soft-masks by NIL for the pattern transfer to Ti by chlorine-based RIE. Furthermore, this route allows the facile and reproducible

production of an elevated number of Ti samples for the preparation of a relevant biological *in vivo* experiment. Since it has been reported that contaminations due to RIE may occur [19, 20], we have characterized the nanogrooved surfaces by X-ray photoelectron spectroscopy (XPS) and a commonly applied live/dead cytotoxicity assay. Figure 18 depicts an overview of the set of parameters defined in the stamp and being transferred to the Ti surface. Note that for the accuracy of the lateral dimension during pattern transfer R_{Stamp} compares to $g_{implant}$. Please further note that our previous publication refers to an R:G ratio with respect to the structure exposed to the cell-culture, here, that is equivalent to $r_{implant}$:$g_{implant}$ [4]. In this work we describe an in-house nanofabrication process for silicon stamps, the preparation of bulk Ti substrates for NIL and the parameters of the nanopattern transfer into the medical-grade Ti by RIE. Finally, we will discuss the results of this study with respect to our aim of using this new nanofabrication method for the preparation of Ti samples in an implantology experiment with scalable nanogroove dimensions.

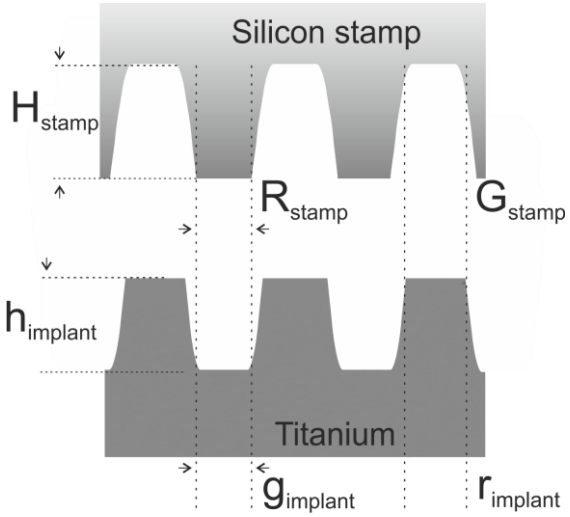

Figure 18. Set of dimensional parameters defined for: mold fabrication (uppercase symbols) and for nanopatterned Ti (lowercase symbols).

4.2. Materials and methods

4.2.1. Ti substrate preparation

ASTM grade 2 bulk Ti discs of a diameter of 100 mm and a thickness of 0.8 mm were used (Bimo Metals, Poland). The supplied Ti had a surface roughness of R_a = 670 nm at a scan length of 33 mm, which was measured with a Dektak 8 profilometer (Veeco, USA). Chemical Mechanical Polishing (CMP) was performed in-house using a Mecapol E460 system (Presi, France), an IC1000 pad (Rohm and Haas, USA) and a SemiSperse 25 (Cabot, USA) slurry diluted 3:1 with water. Polishing was conducted for 18 min with a disc back pressure of 1.3 kN cm $^{-2}$. After polishing, the discs were cleaned in DI water in a dedicated Micro Automation model 2006 cleaning station (Micro Automation, USA) and dried at 60°C in air. The mirror-like surface finish had a surface roughness of R_a = 7 ± 3 nm, which was measured across a scan length of 3 mm and is an average of four polished samples.

4.2.2. Nanoimprint lithography

4.2.2.1. Stamps

Figure 19 illustrates the stamp fabrication scheme by laser interference lithography (LIL) and a silicon reactive ion etching (RIE) process consisting of three steps. Single-side polished prime quality 4″ silicon wafers (Okmetic, Finland) were spin-coated with a trilayer resist. This resist stack consists of a 30 nm thick bottom antireflective coating (DUV 30, Brewer Science, USA), a 120 nm thick negative tone deep UV resist (MA-N 2403, Microresist Technology, Germany) and a top antireflective coating (Aquatar, AZ Electronics, Germany) of a thickness less than 10 nm (Figure 19 A). LIL exposure was performed in a home-built Lloyd's mirror interference setup with a laser wavelength of 266 nm, as described in detail previously [21]. Exposures for the three pitches (P) of

1000 nm, 600 nm and 300 nm were realized with a dose of 4 mJ cm^{-2}. All latent resist patterns were subsequently developed by manual immersion in OPD 4262 developer (Fujifilm, Japan) diluted with water to 75 % v/v for 35 s (Figure 19B).

A parallel plate RIE Pre-Etch is conducted for etch-through of the bottom antireflective coating (BARC) and for the tuning of the R:G ratio (Figure 19C) utilizing a PlasmaTherm 790 system (Unaxis, USA). Subsequently, cryo-RIE at a temperature of -120°C was performed in an Adixen AMS100SE ICP-RIE equipment (Alcatel, France). A liquid nitrogen cooled substrate holder with He backflow of 15 sccm was used for temperature control. An ICP power density of 6.3 W cm^{-2} was applied with an alternating plasma chemistry of 50 sccm SF_6 for 3 s (etching) and 40 sccm C_4F_8 for 2 s (passivation). Etching was stopped at a pre-defined etch time selected to yield a nanostructure height (H) as defined in Figure 19 D, which will be suitable for nanoimprinting of a resist on titanium that yields a sufficiently high aspect ratio for the pattern transfer step to Ti. A final Si etch (Post-Etch) was performed to smooth the nanostructure by parallel plate RIE (Figure 19 E). Both parallel plate etching steps were performed at an r.f. power of 0.6 W cm^{-2} with a graphite electrode and a gas flow of 3 sccm O_2 and 30 sccm SF_6 at 4 Pa chamber pressure and a temperature of 15°C. Etch times were selected as follows: Pre-Etch for 16 s, 13 s, and 10 s; cryo-RIE for 45 s, 36 s, and 22 s; and Post-Etch for 60 s, 40 s, 22 s referring to the different pitch sizes (P) of 1000 nm, 600 nm and 300 nm, respectively. After the pattern transfer etch, a final oxygen plasma step was conducted for 10 min in 500 W r.f. plasma with 55 sccm O_2 flow (TePla 300E, PVA, Germany) to remove residues of resist. All silicon NIL-stamps were coated by chemical vapor deposition of (1H,1H,2H,2H)-perfluorodecyltrichlorosilane (FDTS, Sigma Aldrich) used for anti-stiction.

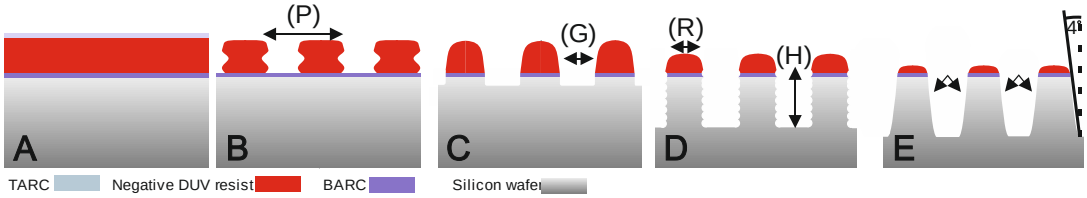

Figure 19. Nanoimprint master fabrication process steps: A) LIL trilayer resist on silicon substrate; B) LIL; C) Resist etch-through into BARC using RIE (Pre-Etch) and subsequently tuning of the lateral dimensions (g to r ratio); D) Cryo-DRIE, tuning the height (h) of the nanostructure; E) RIE, smoothening the nanostructure by RIE (Post-Etch), which results in a slight taper.

4.2.2.2. NIL on Ti-substrates

NIL was carried out on polished Ti discs using thermoplastic resist MR-I 8020 (Microresist, Germany). To realize nanoimprinting with the three different pitch sizes of 1000 nm, 600 nm and 300 nm MR-I 8020 was spin-coated at 1500 rpm, 2000 rpm, and 3000 rpm, which results in a resist thickness of 280 nm, 240 nm and 200 nm, respectively. These values are taken from the spin speed - thickness curve provided by the resist supplier. NIL was performed using an Eitre 6 machine (Obducat, Sweden) at a temperature of 160°C, a pressure of 40 bars and an imprint time of 120 s. Demolding of the imprinted structure was performed at a temperature of 100°C.

4.2.3. Nanogroove pattern transfer to bulk Ti

NIL patterns were transferred to Ti by inductively coupled plasma (ICP) RIE using an Oxford 100 ICP 180 dry etching equipment (Oxford Instruments, UK). We applied a gas composition of 33 sccm Cl_2 , 2.3 sccm CF_4 , 50 sccm Ar, and 2 sccm O_2, an ICP power of 15.3 W cm^{-2} as well as an r.f. power of 0.76 W cm^{-2}. The operating pressure was 3 Pa and the substrate holder temperature was 40°C. The etch times were: 72 s, 47 s, and 35 s for the pitch sizes of 1000 nm, 600 nm and 300 nm, respectively. After the pattern transfer etch, a final oxygen plasma step was conducted for 10 min in 500 W r.f. plasma

with 55 sccm O_2 flow using a TePla 300E apparatus to remove residues of resist (PVA, Germany).

4.2.4. Nanopattern analysis

4.2.4.1. X-ray photoelectron spectroscopy (XPS)

We measured the native Ti as well as the nanostructured Ti surface prior and after additional cleaning by applying XPS analysis (Quantera SXM, Physical Electronics). The radiation was monochromatized Al Kα (1486.6 eV) and the X-ray source was operated at a 25 W emission power and a 15 kV acceleration voltage. A 100 μm diameter beam was used to scan an area of 300 × 300 μm^2. The binding energies for each spectrum were calibrated based on the aliphatic carbon C1s line at 284.8 eV.

4.2.4.2. Topographical characterization

Focused Ion Beam (FIB) Ti cross sections were prepared with a FEI Nova 600 (FEI, USA) dual beam FIB machine with a liquid metal Ga^+ ion source. FIB milling was conducted at beam current of 58 pA with platinum (Pt) as a protective layer. All Ti AFM scans were performed using a Nanoscope III AFM (Digital Instruments), using a high aspect ratio AFM tip in tapping mode (Nanosensors, Switzerland). All SEM images of silicon imprint stamps were taken using a high resolution LEO Gemini 1550 FEG-SEM. Top-down images (not shown) for the evaluation of the uniformity of the lateral dimensions of the nanogrooved Ti were taken by the electron microscope coupled with the FEI Nova 600 dual beam FIB equipment. Subsequently ten measurements of the ridge and groove widths were taken and the average value as well as the standard deviations was calculated.

4.2.5. Sample preparation for implantology protocol

Ti discs of a diameter of 5 mm were cut with electric discharge machining using a 150 μm-diameter cutting wire in DI water (EDM, Charmilles, Switzerland). Petroleum vaseline was used as a protective layer for the nanostructured surface

during cutting. After cutting, the samples were immersed for 2 h in 100 ml of each of the following solvents: chloroform, toluene, acetone and isopropanol (analytical reagent grade, all delivered by Sigma Aldrich), respectively. Finally, the discs were boiled for 10 minutes in 1 L Milli-Q water twice.

4.2.6. Cytotoxicity assay

Rat dermal fibroblasts (RDF) were obtained from the ventral skin of male Wistar rats as described by Freshney (local approval number DEC 2004156) [22]. Cells were cultured in α-MEM medium (Invitrogen) supplemented with 10 % Fetal Calf serum (FCS) and gentamicin (50 μg ml^{-1}). Cell culture experiments on the Ti substrates (cleaned according to the procedure mentioned above) were performed at 6^{th} or 7^{th} culture passage. Prior to transferring the cells to the substrates, cells were detached using trypsin / EDTA (0.25 % w/v trypsin with 0.02 % EDTA, ethylenediaminetetraacetic acid) (Invitrogen) and concentrated by centrifugation at 1500 rpm for 5 minutes. Subsequently cells were resuspended in culture medium, quantified using a Coulter® counter (Beckman Coulter Inc., Fullerton, CA, USA) and seeded at a density of $1^{\bullet}10^4$ cells cm^{-2}. Fibroblasts were cultured for 24 hours on the nanogrooved Ti discs. Subsequently cells were washed 3 times in PBS (phosphate buffered saline) and reagents from the live / dead assay (Invitrogen Corp., Paisley, Scotland) were added to the cells according to the protocol of the manufacturer, which in brief consists of: 2 μL of 2 mM EthD-1 (ethidium homodimer-1) and 1 μL of 4 mM calcein AM solution are added to 5 ml PBS and subsequently incubated for 10 minutes at 37^oC. Next the substrates are washed in PBS and observed using a Zeiss fluorescence microscope (Zeiss MicroImaging, Germany).

4.3. Results

4.3.1. Silicon Nanoimprint Lithography (NIL) stamps

NIL-stamps were defined by laser interference lithography (LIL) and subsequently transferred by reactive ion etching (RIE) to silicon. Figure 20

shows a cross-sectional image of each of the process step by means of example of the smallest pitch P = 300 nm applied for a successful pattern transfer to Ti. Figure 20 A and B depict the resist stack prior and after LIL. Despite using a BARC, here this layer is not optimized to suppress fully the standing wave effect of LIL and the developed resist shows a cross-section with curved side wall profiles (Figure 20 B), whereas the first etch step (Pre-Etch) transfers the LIL resist into the BARC. This etch step is also used to tune the lateral dimensions (G). Figure 20 C shows the result of this first transfer step and indicates that the side wall profiles in the BARC are of sufficiently high quality to perform the nanopattern transfer step to the silicon using the remaining resist/BARC stack as a mask using a process recipe for cryo-deep reactive ion etching (cryo-DRIE). Figure 20 D illustrates the resulting nanostructures with a height (H) of 368 nm. Finally, the side wall roughness of the nanostructures, resulting from the alternating plasma chemistry, is smoothened by a parallel plate RIE Post-Etch. Figure 20 E depicts the final nanostructure of the stamp. The final step results also in a slight tapering of the structure of approximately 4°. Silicon nanostructures with smaller pitch sizes of P = 200 nm and P = 150 nm were realized too, with an aspect ratio of 3.1 and 3.9, respectively. The latter were used in our previous study for replications in polystyrene [4]. However, the smallest pitch size successfully transferred to titanium here, was from a stamp with P = 300 nm and an aspect ratio of 2.5. The values of R, G and H of the three successful utilized stamps are investigated in more detail by SEM and image analysis of which the results are summarized in Table 6.

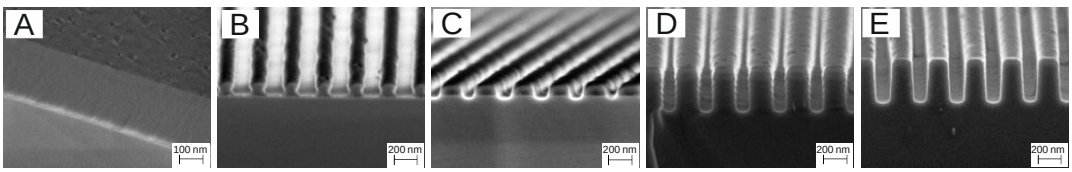

Figure 20. Scanning electron micrographs of a 300 nm pitch nanostructure after each of the five steps of the master fabrication process: A) LIL trilayer resist (for better visibility the

surface contrast in the upper right part was enhanced in the imaging software); B) nanostructure in resist after exposure and development; C) nanostructure in resist after etch-through into BARC; D) resulting nanostructure after Cryo-DRIE in silicon; E) smoothened nanostructure by RIE.

Table 6. Dimensions realized in the silicon stamp and Ti structures created using this stamp.

Pitch size (p)		Dimensions in stamp.			Dimensions in Ti [nm] ± S.D.		
Design [nm]	Realized [nm]	R_{stamp} [nm] ± S.D	G_{stamp} [nm] ± S.D	H_{stamp} [nm] ± S.D	$r_{implant}$ [nm] ± S.D	$g_{implant}$ [nm] ± S.D	$h_{implant}$ [nm]
1000	1020	550 ± 40	470 ± 48	760 ± 18	460 ± 10	530 ± 11	409
600	599	307 ± 18	292 ± 13	700 ± 20	312 ± 16	285 ± 11	205
300	325	177 ± 6	148 ± 11	368 ± 17	156 ± 10	140 ± 9	193

4.3.2. Ti nanopatterns transfer

First, thermal nanoimprint was performed on a standard silicon wafer to characterize the NIL resist height and profile after imprinting. Silicon with nanoimprint resist can be cleaved and cross-sectional images of the resist profiles were taken by SEM (data not shown). The different stamps in combination with the three selected resist thicknesses of 280 nm (P = 1000 nm), 240 nm (P = 600 nm) and 200 nm (P = 300 nm, P = 200 nm and P = 150 nm) prior to NIL yielded resist nanopattern heights, h_{resist}, of 627 nm, 578 nm and 304 nm (only for P=300), respectively. NIL failed for the two smaller pitches of P = 200 nm and P = 150 nm). A residual layer, characteristic for NIL, could not be observed with the inspection technique applied in this work (the resolution of the SEM is approximately 10 nm). Based on these experimental results for NIL on silicon, we selected only the stamps with P = 1000 nm, P = 600 nm and P = 300 nm for pattern transfer to bulk Ti substrates.

The transfer of the pattern to Ti was conducted within a chlorine-based plasma, which creates volatile $TiCl_4$ and other less volatile Ti chlorides. The gas in the

plasma contained a small amount (2.6 %) of CF_4 gas, which, compared to plasma chemistry based only on Cl_2 / O_2 / Ar, increases the selectivity between the soft-mask and the Ti [14, 16]. After removal of the remaining resist in oxygen plasma, the nanogrooved Ti surfaces were investigated by AFM and FIB-SEM. The smallest lateral ridge dimension that we were able to reliably and reproducibly fabricate was 140 nm at P = 300 nm. The AFM images depicted in Figure 21 illustrate the uniformity of the nanopatterns. The increase in surface area, compared to a flat surface, is 81 % for P =1000 nm, 68 % for P = 600 nm and 128 % for P = 300 nm. One has to bear in mind that the AFM data may be only used as a rough estimation of the gain in surface area, because the AFM tip cannot reach into the grooves and therefore does not give an accurate surface profile. The surface roughness was calculated from AFM measurements on an area of 9 μm^2 resulting in: R_a=116 nm for P =1000, R_a=75 nm for P = 600 and R_a=38 nm for P = 300 nm.

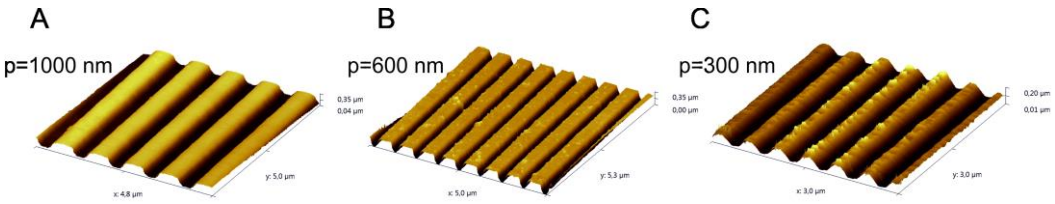

Figure 21. AFM scans of nanostructured Ti surfaces.

To obtain a better understanding of the cross-sectional profiles, we prepared FIB cuts of the nanogrooved Ti surfaces. Figure 22 depicts representative cross-sections of each of the three pitch sizes. The etch times of 72 s, 47 s and 35 s yielded an etch height, h, of 409 nm for P = 1000 nm, 205 nm for P = 600 nm and 193 nm for P = 300 nm, respectively. All dimensional parameters of r, g and h for the three different pitch sizes are summarized and compared to the dimensions of the stamp in Table 6.

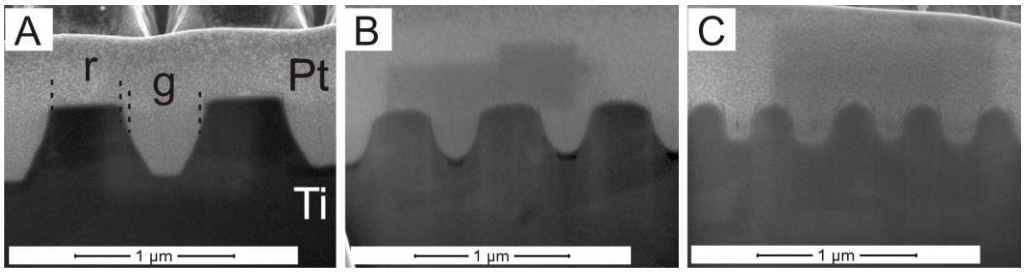

Figure 22. Scanning electron micrographs of nanostructures in Ti at a 52° scan angle. A) 1000 nm pitch B) 600 nm pitch and C) 300 nm pitch. (Cross sections made by Focused Ion Beam milling using Pt as a protective layer.)

We evaluated the lateral dimension of the nanopattern in more detail (left) shows a representative example of a nanogrooved Ti disc of a diameter of 25 mm. The pitch of the nanogrooves is 600 nm. The color impression results from white-light interference with the nanogrooves and already indicates uniform nanopatterns. The disc was cut from the central part of the elliptical exposure area as illustrated in the schematic of the patterned wafer (Figure 23, middle). Top-down SEM images were taken from the five measurement points at the positions indicated in the drawing. The points 2 to 5 are each 1 cm apart from the central point 1 and their r and g values are tabulated (Figure 23, right). The standard deviations have been deducted from repetitive measurements received from SEM images (see Section 4.2.4.2. for further explanation of the measurement method), which are well below 10 % of the average values for r and g.

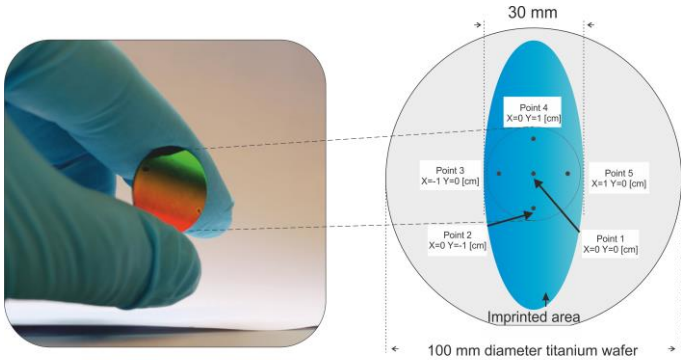

Meas. point	Value. r [nm] ± S.D	Value. g [nm] ± S.D
1	311 ± 17	278 ± 17
2	278 ± 13	314 ± 15
3	299 ± 10	292 ± 13
4	287 ± 14	306 ± 16
5	277 ± 12	309 ± 11

Figure 23. Left: Photograph of a 25 mm diameter Ti disc with nanostructures. Center: Schematic drawing of nanofabricated Ti specimen, showing the imprinted area in blue. Measurements for a uniformity study were taken at the 5 indicated points, located at a mutual distance of 10 mm. Right: Table with values at the 5 different points, originating from SEM image analysis (ImageJ software).

4.3.3. Characterization of the Ti surfaces by XPS

As a reference, the bulk material of one of the Ti discs was analyzed by XPS to determine the composition of the native Ti. After ion beam etching, which removes ca. 90 nm of the surface layer (TiO_2), the analysis showed that the bulk Ti-substrate consists of pure Ti (100 % Ti, with respect to the XPS detection limit). Immediately after nanopatterning in chlorine-based plasma and removal of the resist residue by r.f. oxygen plasma XPS was performed to analyze if contamination originates from this type of process. It was found that the substrates were contaminated with six elements: F, Cl, Al, Ba, Cu and Zn. The measured concentration of these elements is shown in Table 7. It was also found that the Ti $2p_{3/2}$ spectral feature shifted from 453.3 eV to 458.8 eV, a region, which is characteristic for TiO_2. The O1s feature was mostly found in the TiO_2 state. The remaining oxygen can be interpreted to be carbon bound or bound in the other oxides that were present. The $Ba2p_{3/2}$ peak at 780.2 eV refers to barium oxide, the $Cu2p_{3/2}$ peak at 932.3 eV can be also found with characteristic shift in free Cu, Cu_2O or CuCl region, and the Cl2p peak found at 198.5 eV

suggests that Cl is bound in CuCl. Some of these contaminations were expected to be of superficial nature. An additional extensive cleaning process was applied (see Section 4.2.5.) and the XPS measurements were repeated. After cleaning, only the contamination with Zn and Si remained for 12 samples being analyzed and for three of these 12 samples also a significant Al peak remained in the spectrum.

Table 7. XPS elemental analysis results for nanopatterned Ti. Initial composition as obtained from supplier material, removing of the surface layer by sputtering. N/D stands for "not detected".

Element	Initial composition (At. % ± S.D.; n=1, Ion beam sputtered surface)	After RIE etching (At. % ± S.D.; n=10)	After cleaning (At. % ± S.D.; n=12)
Ti	100	Balance	Balance
F	N/D	2.78 ± 0.60	N/D
Cl	N/D	0.41 ± 0.10	N/D
Al	N/D	21.08 ± 0.67	Max 4.03*
Ba	N/D	0.60 ± 0.14	N/D
Cu	N/D	0.42 ± 0.20	N/D
Zn	N/D	0.38 ± 0.11	0.71 ± 0.14
Si	N/D	N/D	1.85 ± 0.53

*detected only on 3 samples

4.3.4. Cytotoxicity assay

A set of nanogrooved 5 mm-diameter Ti discs were exposed to a fibroblast cytotoxicity assay after thorough cleaning as described in section 4.2.5. Figure 24 shows representative images of live/dead stained fibroblast cells. The amount of dead cells (red color) amongst the total amount of observed cells is very low and comparable to the same cytotoxicity assay performed on conventionally roughened samples (e.g., grid blasting). These initial results indicate the suitability of these samples for further *in vivo* experimentation with animals.

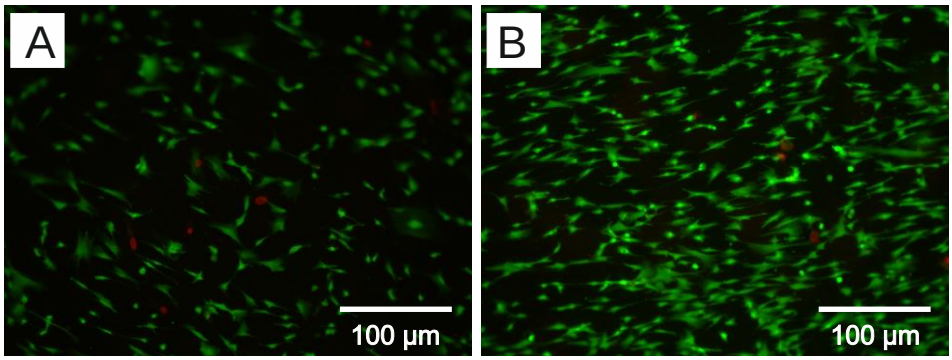

Figure 24. Cytotoxicity study for nanopatterned Ti. Green staining represents viable cells, red staining represents dead cells. Left: structure of 600 nm pitch, right: structure of 300 nm pitch. Scale bar is approximately 100 µm. Note that hardly any dead cells are observed.

4.4. Discussion

We developed a nanofabrication scheme to produce scalable nanogrooved ASTM grade 2 Ti-implants by combining NIL and chlorine-based ICP-RIE.

Standard NIL works with thin, high resolution resist layers on BARC and subsequently using the (non-thermoplastic) BARC after etch-through as a masking layer, which generally works very well with high quality silicon wafers, whereas typically used aspect ratios of the stamps are 1 or even less [23]. During the RIE process, first the native Ti-oxide surface layer has to be removed. Ti-oxide layers are highly etch-resistive in chlorine plasma and are often used as a masking material in RIE [14,15]. Therefore, the transfer of nanopatterns to bulk Ti without additional hard-mask requires a thick soft-mask. The silicon stamps for the three different pitch sizes of 1000 nm, 600 nm and 300 nm, had subsequently an aspect ratio of 1.5, 2.4 and 2.5 respectively. A thick soft-mask process also allows consistent contact between the stamp and the resist layer.

During optimization one needs to take into account specifically the low etch selectivity between the polymer soft-mask and the native Ti oxide layer. Here, the introduction of fluoride compounds into a chlorine-based plasma facilitates TiO_2 etching and allows the nanopattern transfer to the bulk Ti by the applied soft mask process [24].

Furthermore, it has been observed that silicon masters used directly after cryo-DRIE failed to fabricate a thick soft-mask by NIL during the demolding process. Therefore a smoothening step by an unmasked RIE Post-Etch was introduced. This step reduced the sidewall roughness of the stamps and therefore reduced also the friction forces during demolding. Besides that, a smoother surface also presents better conditions for the application of a uniform anti-stiction layer. The Post-Etch also creates a small taper on the highly-vertical nanostructures, which also assists the de-molding process [23].

Variation with respect to the lateral dimensions of ridge and groove may have several causes: interferometric effects in the LIL due to silicon substrate curvature or resist thickness variations, non-uniformity in silicon RIE, bending of either master or Ti substrate during the imprinting process or non-uniformity during RIE pattern transfer to Ti. These variations in the lateral dimensions are relatively small with respect to variations observed in biological responses; we did not investigate these different causes of variations any further. The smallest structure transferred to Ti by NIL was a groove width of 140 ± 9 nm with a selected pitch of 300 nm. Attempts on a structure with a nanogroove pattern with a pitch of 200 nm were unsuccessful (these silicon nanofeatures were actually available with aspect ratios of 3.1 and 3.9 for pitch sizes of 200 and 150 nm, respectively, from our previous study [4]). An increase of the aspect ratio in the stamp and the optimization of the initial resist layer thickness spin-coated on the Ti substrate may improve the resolution of the NIL transfer step on bulk Ti substrates.

Silicon stamps with three different pitch sizes of 1000 nm, 600 nm and 300 nm were successfully transferred to the 100 mm-diameter Ti substrates and

uniformly distributed nanogrooves across an area of at least 4 cm^2 were achieved. These large-area nanogrooved Ti substrates will facilitate the systematic *in vivo* evaluation of nanogrooves, which we consider to have a significant influence on cell behavior based on our *in vitro* study [4]. To accommodate implantology experiments and the preparation of an animal study protocol redundant 5 mm diameter Ti specimens were cut from the nanogrooved Ti substrates and were successfully evaluated for their utility in implantology by a commonly applied cytotoxicity live/dead assay. With respect to parameterization, the roughness parameter R_a is generally used to characterize the various Ti surface treatments [3, 25, 26]. In the case of systematic variations of the topography by highly ordered nanolithographic processes such as for example introduced in this study the values of R_a determined by AFM may give some indication for comparison of different types of surface. The absolute values of these highly regular structures are at the nanoscale and much lower than values received from surfaces treated by established, non-lithographic techniques (see section 3.2). Despite highly regular surfaces having a much lower R_a than the established pre-treated implant surfaces, the influence of this type of artificially created nanotopography on cellular behavior has been considered to be important [27-29]. Therefore, we suggest that using R_a only is not a suitable parameter to compare highly regular nanostructures with structures obtained with other techniques. It is not known at this point, what the actual nanotopographic property is that causes specific cellular responses. A parameter that may be relevant is the gain in surface area. The introduction of regular nanostructures increases the surface area significantly (68-128 %, see section 3.2). In comparison to these values, powder blasting with particles of 9 µm diameter gives only an increase of 31 % and etching for 5 min in 5 % HF increased the available surface area of 24 %. The latter data were obtained from AFM measurements based on a scan area of 9×9 μm^2. With respect to the R_a values received by AFM the AFM tip may not reach completely the bottom of the nanogrooves as mentioned previously (of course, neither would it reach into

narrow pits on randomly distributed surfaces), which suggests that the gain in surface area maybe actually larger than the values received by AFM.

4.5. Conclusions

The clinical goal of any biomaterial surface modification is to deliver a more reliable and better implant. Mechanisms of osseointegration based on nanogroove-tissue interaction can be varied systematically utilizing the technology presented here. A robust and scalable nanofabrication route was developed, ready to obtain three different pitch sizes of 1000 nm, 600 nm and 300 nm on a large area of bulk titanium with a smallest realized groove width of 140 nm The method is based on the in-house fabrication of suitable silicon nanoimprint stamps utilizing laser interference lithography and a dedicated reactive ion etching protocol. Applying these stamps to the repetitive nanopatterning of medical grade bulk Ti using NIL and finally transferring the structure to the polished Ti substrates by chlorine/fluorine-based RIE plasma process will allow a set-of sophisticated implantology experiments. The created nanogrooved Ti surface were characterized by SEM, FIB and AFM techniques and were chemically evaluated with XPS. For the initial biological investigation and preparation of the implantology protocol for animal studies, a live/dead cell cytotoxicity study was carried out and proved that the nanogrooved Ti substrates are suitable for a further set of biological studies either *in vivo* or *in vitro*. The large scalability of the dimensional parameters, r, g and h independently from each other by this nanofabrication route will further facilitate to decipher the factors needed for improved implant performance.

Ethical conduct of research

The authors state that they have obtained appropriate institutional review board approval or have followed the principles outlined in the Declaration of Helsinki for all human or animal experimental investigations. In addition, for

investigations involving human subjects, informed consent has been obtained from the participants involved.

1. Kasemo B., Gold J., Implant surfaces and interface processes. Adv Dent Res., Review., **13**, 8-20 (1999)
2. Dalby M. J., Gadegaard N., Tare R., Andar A., Riehle M. O., Herzyk P., Wilkinson C. D. W., Oreffo R. O. C., The control of human mesenchymal cell differentiation using nanoscale symmetry and disorder. Nat Mater **12**, 997-1003 (2007)
3. Rosales-Leal J I, Rodriguez-Valverde M A, Mazzaglia G, Ramon-Torregrosa P J, Diaz-Rodriguez L, Garcia-Martinez O, Vallecillo-Capilla M, Ruiz C, Cabrerizo-Vilchez M A, Effect of roughness, wettability and morphology of engineered titanium surfaces on osteoblast-like cell adhesion. Colloid Surface A **365**, 222-229 (2010)
4. Lamers E, Walboomers X F, Domanski M, te Riet J, van Delft F C M J M, Luttge R, Winnubst A J A, Gardeniers J G E, Jansen J, The influence of nanoscale grooved substrates on osteoblast behavior and extracellular matrix deposition. Biomaterials **31**, 3307-3316 (2010)
5. Weiner S, Wagner H D. The material bone: Structure mechanical function relations. Annu Rev Mater Sci **28**, 271-298, (1998)
6. Anselme K, Davidson P, Popa A M, Giazzon M, Liley M, Ploux L. The interaction of cells and bacteria with surfaces structured at the nanometre scale. Acta Biomaterialia **6**, 3824-3846 (2010)
7. Bagno A, Di Bello C. Surface treatments and roughness properties of Ti-based biomaterials. Journal of Materials Science: Materials in Medicine **15**, 935-949, (2004)
8. Kasemo B, Gold J. Implant Surfaces and Interface Processes. Advances in Dental Research **13**, 8-20, (1999)
9. Le Guehennec L, Soueidan A, Layrolle P, Amouriq Y. Surface treatments of titanium dental implants for rapid osseointegration. Dent Mater **23**, 844-854 (2007)
10. Linez-Bataillon P, Monchau F, Bigerelle M, Hildebrand H F. In vitro MC3T3 osteoblast adhesion with respect to surface roughness of Ti6Al4V substrates. Biomolecular Engineering **19**, 133-141 (2002)
11. Liu X, Chu P K, Ding C. Surface nano-functionalization of biomaterials. Materials Science and Engineering: Reports **70**, 275-302 (2010)
12. Puckett S D, Taylor E, Raimondo T, Webster T J. The relationship between the nanostructure of titanium surfaces and bacterial attachment. Biomaterials **31**, 706-713 (2010)
13. Parker E R, Rao M P, Turner K L, Meinhart C D, MacDonald N C. Bulk micromachined titanium microneedles. J Microelectromech **16**, 289-295 (2007)
14. Parker E R, Thibeault B J, Aimi M F, Rao M P, MacDonald N C. Inductively coupled plasma etching of bulk titanium for MEMS applications. J Electrochem Soc **152**, C675-C683 (2005)
15. Zhao G, Shu Q, Tian Y, Zhang Y M, Chen J. Wafer level bulk titanium ICP etching using SU8 as an etching mask. J Micromech Microeng **19**, 095006 (2009)

16. Xiao Y B, Kim E H, Kong S M, Park J H, Min B C, Chung C W. Inductively coupled plasma reactive ion etching of titanium thin films using a Cl_2/Ar gas. Vacuum. **85**, 434-438 (2010)
17. Gilmartin S F, Arshak K, Bain D, Lane W A, Collins D, Arshak A McCarthy B, Newcomb S B, Walsh M, Development of a titanium plasma etch process for uncooled titanium nanobolometer fabrication. Microelectron Eng **86**, 971-975 (2009)
18. Galli C, Coen M C, Hauert R, Katanaev V L, Groning P, Schlapbach L. Creation of nanostructures to study the topographical dependency of protein adsorption. Colloid Surface B **26**, 255-267 (2002)
19. Kasemo B, Lausmaa J. Material-Tissue Interfaces: The Role of Surface Properties and Processes. Environmental Health Perspectives **102**, 41-45 (1994)
20. Pypen C M J M, Plenk Jr H, Ebel M F, Svagera R, Wernisch J. Characterization of microblasted and reactive ion etched surfaces on the commercially pure metals niobium, tantalum and titanium. Journal of Materials Science: Materials in Medicine **8**, 781-784 (1997)
21. Luttge R. Massively parallel fabrication of repetitive nanostructures: Nanolithography for nanoarrays. Journal of Physics D: Applied Physics **42**, 123001 (2009)
22. Freshney IR. Culture of Animal Cells: a Manual of Basic Technique. New York: Alan R Liss, Inc., (1987)
23. Schift H. Nanoimprint lithography: An old story in modern times? A review. J Vac Sci Technol B **26**, 458-480 (2008)
24. Fracassi F, Dagostino R. Chemistry of Titanium Dry Etching in Fluorinated and Chlorinated Gases. Pure Appl Chem **64**, 703-707 (1992)
25. Flemming R G, Murphy C J, Abrams G A, Goodman S L, Nealey P F. Effects of synthetic micro- and nano-structured surfaces on cell behavior. Biomaterials **20**, 573-588 (1999)
26. Lee G J, Park K H, Park Y G, Park H K. A quantitative AFM analysis of nano-scale surface roughness in various orthodontic brackets. Micron **41**, 775-782 (2010)
27. Biggs M J P, Richards R G, Dalby M J. Nanotopographical modification: a regulator of cellular function through focal adhesions. Nanomedicine: Nanotechnology, Biology and Medicine **6**, 619-633 (2010)
28. Yim E K F, Pang S W, Leong K W. Synthetic nanostructures inducing differentiation of human mesenchymal stem cells into neuronal lineage. Experimental Cell Research **313**, 1820-1829 (2007)
29. Yin Z, Chen X, Chen J L, Shen W L, Hieu Nguyen T M, Gao L, Ouyang H W, The regulation of tendon stem cell differentiation by the alignment of nanofibers. Biomaterials **31**, 2163-2175 (2010)

5.

INFLUENCE OF RIDGES NANOFABRICATED IN SILICON ON PURIFIED PROTEIN ADSORPTION

Abstract

In this work the interaction of protein moieties with nanoscale ridges machined in a silicon substrate was studied. In addition to surface nanostructure, the silicon surface chemistry was modified to render it hydrophobic or hydrophilic. The influence of factors like nanofeature size, roughness, and surface wettability on the quantity of adsorbed proteins was measured. For this study the ExtraCellular Matrix (ECM) proteins: Bovine Serum Albumin (BSA), Bovine Collagen I (COL-I), and Bovine Fibronectin (FN) were selected. Quantification was conducted using a depletion method with a colorimetric assay and UV-Vis readout. In addition, XPS was used to determine the atomic composition of the surfaces, and HRSEM and HIM were applied to obtain information about the topography of the adsorbed proteins. The results show that hydrophobicity has a direct influence on protein adsorption. Due to the limited accuracy of the applied assay, no significant effect of distinct nanotopographies on the amount of adsorbed protein could be established. On the other hand, some remarkable information about the conformation of adsorbed collagen was obtained.

5.1. Introduction

Proteins in their native state adsorb on the solid – liquid interface [1]. Adsorption is affected by changes in the surface properties, being either chemical modification or changes in surface topography [2-4]. It is known that surfaces carrying nanostructures can influence protein adsorption both in quantity and in quality [5-9]. Furthermore, surface parameters like hydrophobicity and charge play an important role [10-13]. Energy minimization during adsorption processes is followed in most cases by structural perturbations in the adsorbed protein. Depending on the surface characteristics and the (local) curvature of the surface, proteins can bind in native form, flatten or arrange in short-range organized monolayers. This reorganization is caused by restructuring of locally charged and hydrophobic or hydrophilic domains of the protein in contact with the surface and interactions of both chemical and physical nature that might be further influenced by nanotopography [4,14]. In addition, the adsorption mechanism depends on liquid phase characteristics like ionic strength. Finally, proteins of different kind may adsorb in competition depending on conditions and size, which is recognized as the Vroman effect [15]. The system of forces and kinetic processes leading to adsorption of proteins on nanofeatures is not yet fully explored due to the complexity of the interactions. In recent years extensive studies on adsorption phenomena have been conducted, for example work conducted by Vogler et al. brought significant new insights in the interfacial phenomena of protein adsorption [16-19].

In this work we focus on evaluating the influence of regular topographical nanoscale surface features (Figure 25) on the adsorption of a number of selected ECM proteins. We hypothesize that molecular size – surface feature size interaction is a driving force in controlling the amount of adsorbed ECM protein on the nanopatterned surface. To test this hypothesis, we create samples with well-defined topography and surface area, with different nanostructural dimensions with a pitch in the pitch range 150 - 600 nm. Extracellular matrix

proteins chosen for this study are Bovine Serum Albumin (BSA), Bovine Collagen type 1 (COL-I) and Bovine Fibronectin (FN). The substrate material is silicon with a thin oxide layer carrying sub-micrometer ridges on areas of 11 × 11 mm^2. Together with topography we also introduce two distinct surface chemistries: hydrophilic silicon oxide with hydroxyl surface groups (SiO_2–OH), or hydrophobic with surface alkyl groups (SiO_2–CH_3). It is known that a hydrophobic surface enhances protein adsorption by hydrophobic-hydrophobic interactions[10,11,13,20]. Additionally, dependent on the pH, the SiO_2–CH_3 surface net charge can be more positive than –OH terminated surface, which may change charge-charge type interactions.

5.2. Materials and methods

5.2.1. Fabrication of silicon samples

The details of the fabrication process were described in previous chapters (Silicon nanofabrication, chapter 2). In brief, double-side polished (DSP) prime quality 4″ silicon wafers (Okmetic, Finland) were spin-coated with: bottom antireflective layer, deep UV resist (MaN-2403, Microresist Technologies, Germany) and top antireflective layer. The LIL exposures were performed in a home-built Lloyd's mirror interference setup with a laser wavelength of 266 nm. Exposures doses were ranging from 3 mJ cm^{-2} for 1:3 R:G to 8.5 mJ cm^{-2} for 3:1 R:G ratios. Four pitch sizes (P) were defined in LIL: 600 nm, 300 nm, 200 nm, 150 nm. After developing the LIL resist, the pattern was transferred into silicon by a three-step RIE process. A parallel plate RIE step was conducted for BARC etch-through and tuning of the lateral dimensions of the nanoridges (R:G) (PlasmaTherm 790, Unaxis, USA). A Cryo-DRIE process at a temperature of -120°C was used to tune the nanoridges height (H) (Adixen AMS100SE ICP-RIE, Alcatel, France). In the last step, the sidewalls of the ridges (which contain "scallops" typical for Bosch-type etching recipes) were smoothened by etching in parallel plate RIE. Only one side of the Si samples was patterned, the backside was left as it is (polished). Finally, an oxygen

plasma step was conducted for 10 min in 500 W RF plasma with 55 cm^3 min^{-1} O_2 flow (TePla 300E, PVA, Germany) to remove residues of resist.

The nanopatterns consisted of ridges with different dimensional parameters of pitch (P) and ridge to groove (R:G) ratios (Figure 25). The height (H) of the nanostructure was aimed to be identical with pitch (P:H=1:1). The samples were named with following convention: "P nm, X:Y" where: P is pitch value in nm and X:Y is R:G ratio. The value of R:G is not exact mathematical ratio and it is only indicative. The fabricated samples were: 600 nm, 1:1; 300 nm, 1:1; 300 nm, 3:1; 200 nm 1:3; 150 nm 1:1.

Additionally two more sample types were prepared and included in the adsorption experiments: Powder Blasted (PB; prepared in a home-built powder blasting setup, 9 μm alumina powder) and Flat Silicon (Flat)**.** Fabricated silicon samples were cut to a size of 11 × 11 mm^2, with a DAD-321 wafer dicer (Disco, Japan) and cleaned in an isopropanol ultrasonic bath. Similarly, a number of flat untreated silicon samples were prepared with a size of 5.5 × 5.5 mm^2, to determine a reference curve of protein adsorption versus silicon surface area.

All silicon samples were oxidized in dry air at a temperature of 850°C for 1 h.

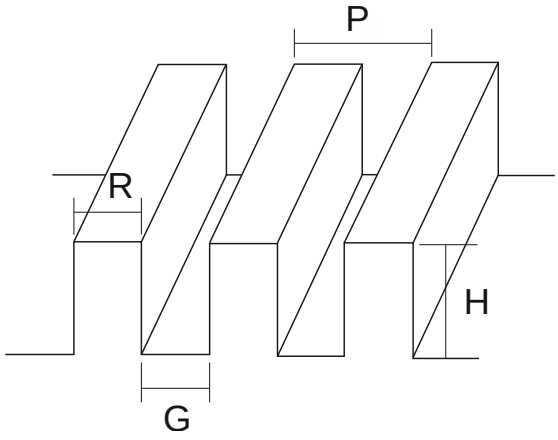

Figure 25. Geometry of nanostructure. Set of parameters is used to describe it: (P) pitch of structure; (R) ridge width; (G) groove width; (H) structure height.

5.2.2. Chemical treatment of surfaces

5.2.2.1. Cleaning

Samples were cleaned in 1.5 ml of 2 % aqueous solution of Hellmanex II (Hellma analytics) at a temperature of 30°C for 2 h, followed by washing with copious amounts of demineralized water with a conductivity of 0.55 µS and immersion in 1.5 ml per sample of freshly prepared 12:2:86 v/v/v $HCl:H_2O_2:H_2O$ for 1 h at 40 °C. Finally, samples were washed with copious amounts of demineralized 0.55 µS water and air dried at 60 °C.

5.2.2.2. CH_3 and OH surface termination

Two series of the 11 × 11 mm^2 surfaces were prepared, with the same nanostructure pitch size and two distinct surface chemistries. One batch was activated with O_2 plasma (referred as SiO_2–OH), a second batch was treated with O_2 plasma and bis(trimethylsilyl)amine (HMDS, Sigma Aldrich) to terminate the surface with methyl (CH_3) groups. Oxygen plasma treatment was conducted in a plasma cleaner (Anadis, Harrick Plasma) at an O_2 flow of 1.8 $cm^3\ min^{-1}$, a pressure of 80 Pa and a forwarded RF power of 29.6 W for 1 h. SiO_2–OH designated samples were left overnight in air and used as such for adsorption experiments.

Directly after O_2 plasma treatment SiO_2–CH_3 designated samples were immersed in pure HMDS and heated to 65°C for 1 h. The samples were transferred to a desiccator, evacuated and kept overnight. Next day the samples were rinsed 3 times with isopropanol, air dried, and used for adsorption experiments. This coating method is well-established for silicon surface hydrophobization[21].

All of the 5.5 × 5.5 mm^2 were treated with HMDS in the same manner.

5.2.3. Surface characterization of SiO_2–CH_3 and SiO_2–OH surfaces

5.2.3.1. Scanning electron microscopy and atomic force microscopy (SEM and AFM) of the silicon samples

SEM images of representative samples were recorded using a high resolution LEO Gemini 1550 FEG-SEM to establish dimensions. Dimensional parameters and thickness of the oxide layer were evaluated using ImageJ software. AFM measurements of powder blasted (PB) sample were obtained with Dimension Icon AFM (Vecco, USA) using Nanosensors NCH probes in TappingMode™ and roughness was estimated with Gwyddion software [22].

5.2.3.2. Ellipsometry

The thickness of the HMDS layer on flat samples with SiO_2–CH_3 and SiO_2–OH surface was determined by ellipsometry using a VASE (J.A. Woollam, USA) instrument. Three incident angles of 65°, 70° and 75° and wavelengths from λ= 250 to 1250 nm were used. Data were processed with WVASE32 software implementing a two layer Cauchy model [23].

5.2.3.3. XPS analysis

Flat samples with SiO_2–CH_3 and SiO_2–OH surfaces were analyzed by XPS (Quantera SXM, Physical Electronics). High resolution spectra were collected for the elements N, C, O and Si using the Al Kα line at 1486.6 eV. A 25 W emission power and 15 kV of acceleration voltage were applied in the analysis. Scanning was done with a 100 μm diameter beam meshing area of 0.3×0.3 mm^2. The binding energies for each spectrum were calibrated based on the aliphatic carbon C1s line at 284.8 eV. The spectra were used for comparison with a simulation model generated by Sessa software to obtain the HMDS layer thickness (DB 100 Simulation of Electron Spectra for Surface Analysis V1.1, NIST, USA). Structural parameters used in the simulation were: HMDS layer consisting of Si with three methyl groups and 38 nm of SiO_2 on the surface of Si.

5.2.3.4. Water contact angle

Contact angles were measured with DI water using an OCA-20 goniometer (Dataphysics, Germany). Two measurements were taken for each of the 6 flat samples for each of the surface types SiO_2–CH_3 and SiO_2–OH.

5.2.4. Protein quantification with depletion method

The depletion method was based on measuring the quantity of protein left in solution after 2 h of incubation of the samples in a low adhesion 24 well plate. This quantity was then determined using a colorimetric Bradford type assay with the Pierce Coomassie Blue assay kit (Thermo Scientific). Final calculation of the adsorbed protein amount ($C_{adsorbed}$) was done by comparing the initial concentration (C_0) with the concentration after incubation of samples (C_{final}), $C_{adsorbed}=C_0-C_{final}$. C_0 was corrected for adsorption on the well walls. The dependence of Optical Density (OD) on protein concentration was described by 2^{nd} order polynomial fits. The data points for creating the calibration curves were collected in each experiment run from 12 known dilutions of protein.

5.2.4.1. Protein solutions

The proteins used in the study were single purified Collagen (COL-I), Fibronectin (FN) and Albumin (BSA) solutions. Relevant properties of the proteins and experimental concentrations are collected in Table 8. Purified proteins were used as received after reconstituting or diluting to concentration of 100 µg ml^{-1} using 0.01 M phosphate buffered saline (120 mM sodium chloride, 2.7 mM potassium chloride, and 10 mM phosphate buffer salts); pH 7.4, at 25 °C. (PBS, Sigma Aldrich). After dilution, the aliquots were kept in 4°C and used within 4 days. Before the experiment, protein aliquots were mixed with buffer to the working concentration (Table 8). Prior to each run of experiment working concentration of protein was quantified using UV absorption spectroscopy with λ=280nm and calculated using extinction coefficients provided by the supplier.

Table 8. Purified proteins used in the study and their characteristics.

Protein	Origin	MW, Structure	Isoelectric point [IEP]	Initial concentration in experiment [μg ml^{-1}]	Calculated size in solution [nm][1]	Measured size adsorbed on SiO_2-CH_3 surface (AFM) [nm]
Albumin (BSA)	Bovines serum, solution	66 kDa, globular	4.9	22.5	3.53	9.7 × 3.7
Collagen (COL-I)	Bovine skin, solution	270 kDa, Dimeric fibrillar	5-7	11.2-15.5	5.65	44 × 3
Fibronectin (FN)	Bovine tendon, solution	440 kDa, Dimeric fibrillar	5.4	17.5-18.8	6.64	51 × 32

[1] Calculated using empirical expression $\mathrm{R} = 1.3 \times R_v;\ R_v = 6.72 \times 10^{-8} MW^{\frac{1}{3}}$

5.2.4.2. Experimental protocol for flat samples - method validation

The 5.5 × 5.5 mm^2 square flat SiO_2–CH_3 samples were inserted in 24 well plates (Costar Ultra-low attachment, ULA, Corning Inc.). Adsorption from single protein solutions was measured on surface areas of 0, 72, 144, 217, 289, and 361 mm^2 that were represented by: empty well, 1, 2, 3, 4 and 5 pieces of SiO_2–CH_3 samples, respectively. Surface area was calculated taking into account top, bottom and the four side surfaces of each 5 × 5 mm^2 silicon sample. Measurement of adsorption was repeated 6 times for each surface area.

This test was performed both for Fibronectin (FN) in a concentration of 17.5 μg ml^{-1} and for Collagen (COL-I) in a concentration of 8 μg ml^{-1}. 300 μL of a single protein solution of known concentration (C_0) was pipetted into each, using an automatic pipette (Multipette Xstream, Eppendorf). Multiwell plates with samples and protein solution were sealed rocked at 37°C (20 rev min^{-1}) for 2 h. After incubation the plates were cooled down and 140 μL of content of each well was transferred to a 96 well plate (UV Star 96 well plates, Greiner Bio One) and mixed with 140 μL Bradford assay working reagent. Readout of

the O.D. was conducted after 10 minutes in a Safire2 (Tecan, Austria) multiplate reader using 1000 readouts for each well and wavelength of λ=592 nm. After the experiment, the samples were cleaned as in paragraph 5.2.2.1. Each experiment was repeated 3 times.

5.2.4.3. XPS analysis of albumin adsorption

Using the same equipment and parameters as above, the adsorption of albumin by XPS was studied. To this end, both CH_3 and OH terminated oxidized silicon samples were incubated in BSA for 2 h as described in the paragraph "experimental protocol for protein adsorption and method validation". The samples were rinsed gently with a large amount of demineralized water and air-dried. According to literature, this procedure does not alter the adsorbed protein layer [24].

The atomic composition of the resulting surfaces was evaluated with XPS as described above. The samples were installed in an XPS holder and spectra were collected on four arbitrarily chosen points of each of 14 SiO_2–CH_3 and SiO_2–OH terminated samples with every type of surface structure. The presence and relative quantities of carbon, nitrogen, silicon and oxygen were calculated from the raw XPS data using CasaXPS software provided by Casa Software Ltd. (Teignmouth, UK). Curve fitting of the spectra was performed by applying a symmetrical Gaussian/Lorentzian (70/30) function. Intensities were calculated from peak areas and corrected using elemental Scofield factors. The used background was Tougaard. In the curve fitting procedure the FWHM of the different contributing peaks were not fixed but fitted as well, however the variation in FWHM was kept within constrain of ±1 eV for all contributions. This does not give a significant change in the relative contribution of a peak to the total signal.

5.2.4.4. Observation of adsorbed proteins by electron and ION microscopies

High resolution electron microscopy (HRSEM) and helium ion microscopy (HIM) were used to observe the topography of proteins adsorbed on nanostructured surfaces. Samples for microscopy were prepared identically as for quantification experiment. Albumin collagen or fibronectin were adsorbed on samples from PBS buffer and subsequently specimens were washed in DI water to remove unbound protein, and air dried. No electron microscopy staining methods were used.

For the SEM observations low electron acceleration voltages were used in order to obtain good contrast on protein-on-silicon samples. Electron accelerations in range up to 1 keV were used and imaging was done in secondary electron mode using in-lens detector.

For the HIM observations helium ions accelerated with 30 keV potential were used. The used equipment was Carl Zeiss SMT Orion Helium Ion Microscope [25] and the images were collected in secondary electron mode.

5.3. Results

5.3.1. Surface characterization of silicon nanostructures

Fabricated nanostructures were in shape of ridges with different pitch size (Table 9). Parameters of the surface features like height (H), ridge size (R), and groove size (G) were measured using SEM. The surface area gain introduced by the nanostructure was calculated for each surface using the relation $\Delta A = \frac{\text{Nanostructure Surface Area}}{\text{Projected Area}} \times 100\%$. Using the ΔA value, the real surface area of each sample type was estimated (A_{sample}). The surface area increase of Powder Blasted samples were estimated from the AFM measurement. Obtained dimensional parameters are summarized in Table 9 and in Figure 26.

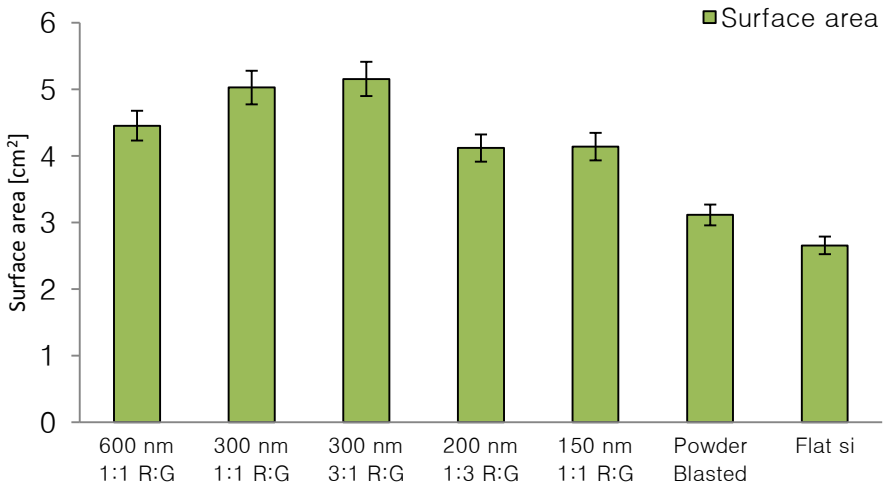

Figure 26. Surface areas of nanostructured silicon samples estimated with SEM image analysis

Table 9. Nanofabricated surfaces used in study and their dimensional characteristics.

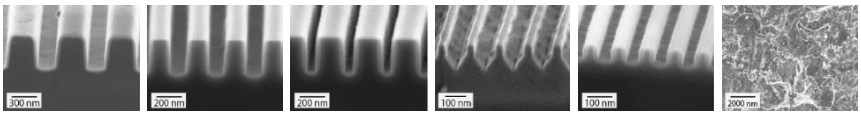

Flat

Pitch [P] type	600 nm	300 nm 1:1	300 nm 3:1	200 nm 1:3	150 nm 1:1	Powder Blasted	Flat Si
Ridge [R]	364	167	225	74	80	-	-
Groove [G]	242	138	75	133	66	-	-
Height [H]	443	292	310	184	94	-	-
Surface area gain (ΔA)[1]	248	296	306	221	222	138	100
Complete surface of sample (A_S)[2] [cm²]	4.45	5.01	5.15	4.11	4.13	3.13	2.65

[1] $\Delta A = \frac{\text{Nanostructure Surface Area}}{\text{Projected Area}} \times 100\%$

[2] Surface area of complete 11 × 11mm² sample including the nanostructure contribution

The ellipsometric measurement on the flat silicon sample with and without HMDS treatment shown that the thickness of the hydrophobic coating with CH_3 termination is 6.5 ± 0.4 Å.

An XPS scan of the surface of SiO_2-CH_3 and SiO_2-OH terminated flat samples and subsequent simulation with SESSA software gave a HDMS layer thickness of 3.8 ± 0.4 Å. The disagreement of this value with the ellipsometric measurement may suggest that the layer is not homogeneous.

The measured water contact angles show that SiO_2-OH terminated samples are hydrophilic with contact angle of 11.6° ± 1.2°. For the SiO_2-CH_3 terminated surface the water contact angle was 106.8° ± 5.8°, which shows that the surface indeed is hydrophobic.

5.3.2. Protein quantification

One possible hypothesis on the influence of nanostructure on the amount of adsorbed proteins is that a higher adsorbed amount may simply be caused by the increase in surface area (see Table 9). To validate this we first calibrated the relation between protein adsorption and surface area, by measuring protein adsorption on increasing numbers of flat oxidized and CH_3 terminated silicon samples of identical size. Calibration curves for both tested proteins (see Figure 27) COL-I and FN are found to be linear, with adjusted R^2 factors of $R_{COL\text{-}I}^2 = 0.97$ and $R_{FN}^2 = 0.99$, respectively.

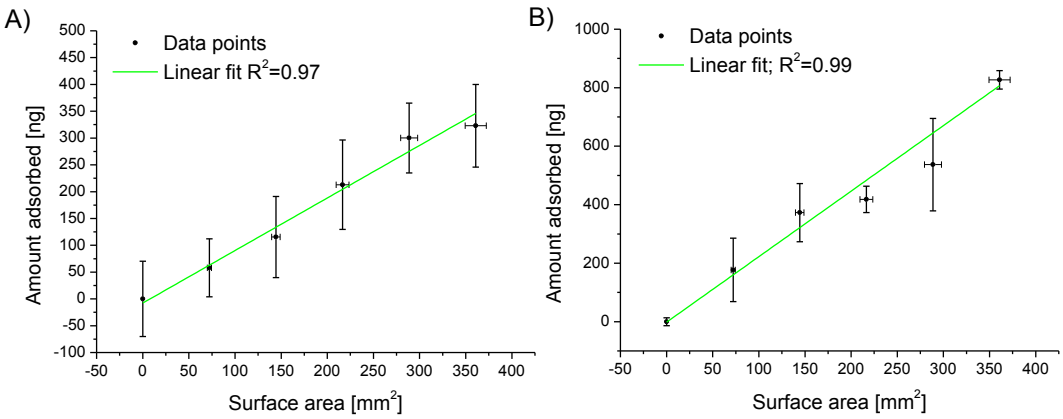

Figure 27. Quantities of adsorbed: a) collagen (COL-I) and b) fibronectin (FN) on flat silicon surface as a function of surface area. N=6 for each point.

Using the depletion method and a Bradford type colorimetric assay, the amounts of adsorbed proteins were quantified on the full range of nanostructured and reference samples. Results of adsorption for the three used proteins are summarized in Figure 28, Figure 29 and Figure 30. The quantities are normalized to 1 cm^2 of projected surface, i.e., the surface gain due to the nanostructures is not included in the surface area at this point.

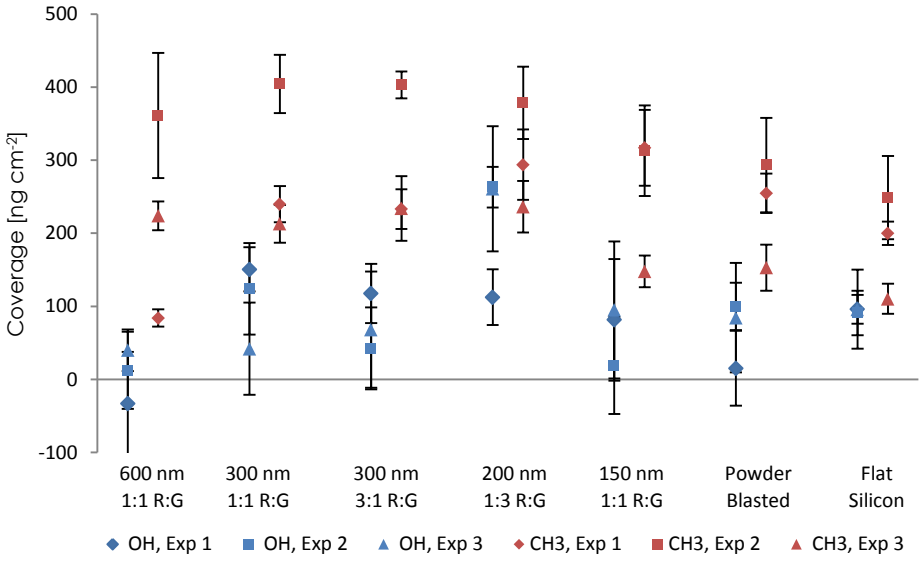

Figure 28. Quantities of adsorbed albumin (BSA) on specific samples with surface modifications; Surface area is a projection area in cm^2; Values of each of the three experiments (Exp 1, 2, 3) plotted with corresponding error (S.D.) from six measurements per experiment.

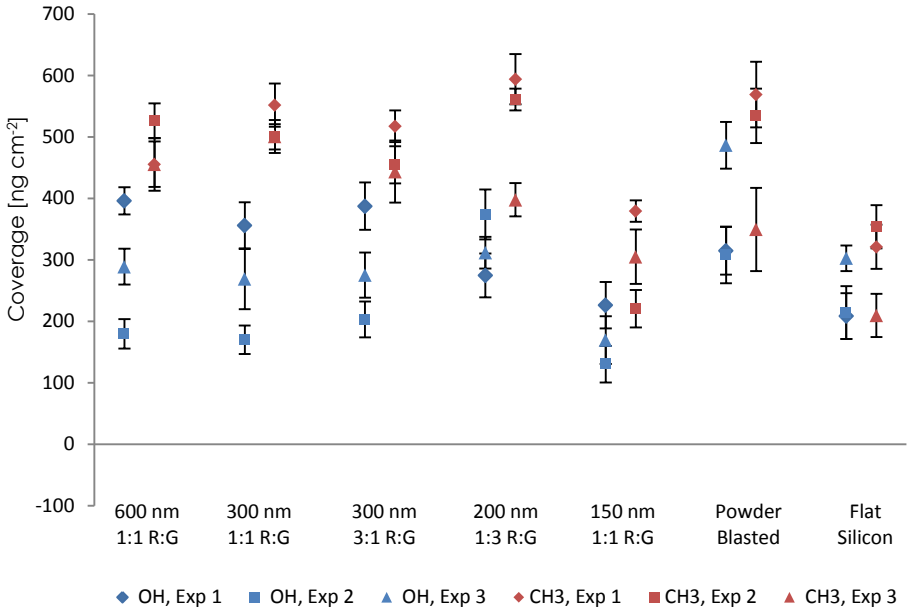

Figure 29. Quantities of adsorbed fibronectin (FN) on specific samples with surface modifications; Surface area is a projection area in cm^2; Values of each of the three experiments (Exp 1, 2, 3) plotted with corresponding error (S.D.) from six measurements per experiment.

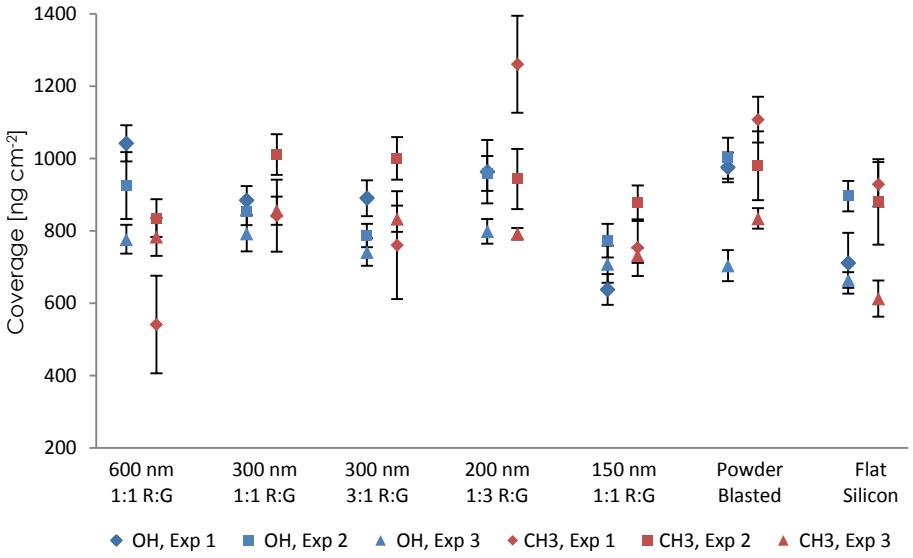

Figure 30. Quantities of adsorbed collagen (COL-I) on specific samples with surface modifications.; Surface area is a projection area in cm^2; Values of each of the three experiments (Exp 1, 2, 3) plotted with corresponding error (S.D.) from six measurements per experiment.

5.3.3. XPS of Albumin adsorbed on SiO_2 –CH_3 and SiO_2–OH surfaces.

The core spectra of C, N, O and Si were averaged from 28 measurement points for each of the Albumin-treated SiO_2–CH_3 and SiO_2–OH surfaces. Some example spectra are shown in Figure 31.

The nitrogen signal N1s at E_b=399.6 eV was detected on all samples, which confirms that albumin is present on all samples, whether they are SiO_2–CH_3 or SiO_2–OH terminated. The core level spectrum of nitrogen, N1s, is symmetric, as is expected for albumin amine or amide groups. The atomic percentages of N, calculated from the spectra of BSA adsorbed on a SiO_2–OH and SiO_2–CH_3 terminated surfaces, were 0.6 ± 0.1 and 5.7 ± 0.3 at. %, respectively, which would correspond with a higher degree of protein adsorption on the SiO_2–CH_3 terminated surface.

Oxygen core spectra gave atomic oxygen percentages of 64 ± 7 at. % and 48 ± 5 at. % for OH and CH_3 terminated surfaces, respectively. The oxygen was found in three forms: OH^-, O^{2-} and possibly also water (see Figure 31).

Silicon spectra show that the majority of silicon (90 ± 10 at. %) is in the form of silicon dioxide. The atomic percentages are 28 ± 3 at. % and 22 ± 2 at. % on SiO_2–OH and SiO_2–CH_3 terminated surfaces.

The C1s spectrum was deconvoluted with contributions corresponding to carbon in three types of bonds. Peak C_I (see Figure 31) at E_b=285.0 eV was assigned to C-C, C=C and C-H bonds, peak C_{II} at E_b=286.4 eV to C-N and C-O single bonds, and the peak at E_b=288.4eV to O=C-O and O=C-N belonging to peptide bonds. This fingerprint is characteristic for adsorbed proteins [26-28]. However, it is common knowledge that the E_b=284.9eV region most likely contains a contribution of carbon contamination. The atomic percentage of carbon for BSA on an OH terminated surfaces was 4 ± 1 at. %, with contributions from C_I of 49 ± 17.0 %, from C_{II} of 37 ± 14 % and from C_{III} of 12 ± 11 %. For BSA adsorbed on SiO_2–CH_3 terminated surfaces the atomic concentration of carbon was 24 ± 5 at. %, with a contribution of 48 ± 19 % for C_I, 28 ± 13 % of C_{II}, and 17 ± 6 % of C_{III}.

The N/C ratio in pure BSA has a value of 0.23. The ratios obtained from the experiments are 0.14 for albumin adsorbed on the OH terminated surfaces and 0.23 for the SiO_2–CH_3 terminated surfaces. The lower value for OH terminated surfaces may be caused by a higher contribution from aliphatic carbon contamination, but it has also to be taken into account that the accuracy of this value is low, because of the quite low atomic percentage of N on these surfaces.

For the above data, in particular from the N core level spectra, we conclude that the amount of adsorbed protein on SiO_2–CH_3 surfaces is significantly higher than that on SiO_2–OH surfaces, which corresponds to the adsorption measurements presented earlier in this chapter.

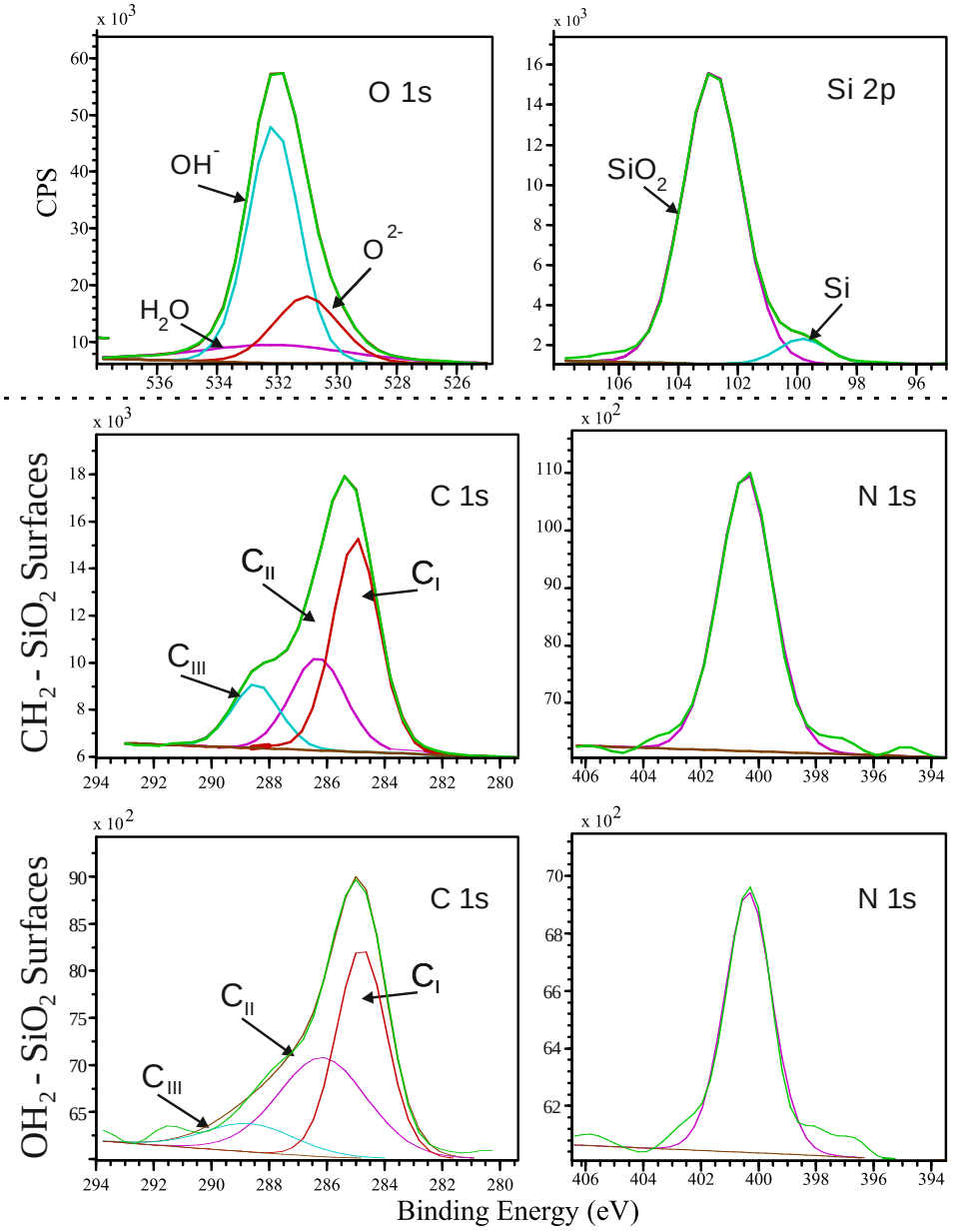

Figure 31. XPS examples for a flat oxidized silicon sample with adsorbed BSA. 28 of such spectra were used to calculate the average composition for all samples. The characteristic core spectra were collected after 2 h incubation of samples in a BSA solution with a concentration of 22.5 μg ml^{-1}, see text. The green lines are the collected core level spectra,

the colored lines are the peak decompositions. The peaks were decomposed using 30/70 Gaussian/Lorentzian fitting and corrected with RSF.

5.3.4. High resolution scanning electron microscopy (HRSEM) and helium ion microscopy (HIM) of proteins

For albumin and fibronectin samples no conclusive results could be obtained from the HRSEM and HIM observations, due to the low contrast between carbon rich protein and silicon surface, which can be clearly seen in Figure 34 C where a scratch on the adsorbed protein surface was made prior to SEM and the image is collected in one scan. Despite the low contrast, the HRSEM and HIM images do not show specific organization of neither albumin nor fibronectin on the ridge-groove structures.

In case of collagen specific self-organization was observed (Figure 33), where the organization is more pronounced on SiO_2–CH_3 surfaces, where it has a characteristic "ladder" structures, whereas on SiO_2–OH the ladder-like structure was observed only in small regions with an area of less than 100×100 nm^2. Possible explanations for the ladder-like structures could be drying effects or the formation of fibers of single or double strand collagen which bridge the nanoridges. To observe the fibers in more detail, HIM was used (see Figure 32). The combination of the reduced probe size and the enhanced secondary electron yield generated by the He ions in this method allows imaging of the protein fibers in very fine detail, with a higher resolution and better Z contrast than achievable with SEM. This is because the interactions of a helium ion beam with a specimen are fundamentally different from those of an electron beam. With HIM the fibers were indeed clearly observed. Image analysis of HIM gave a fiber thickness of 3.3 ± 0.4 nm which corresponds to the thickness of a double strand collagen fiber. However, it also has to be mentioned that the probe size in HIM is typically close to 0.5 nm, so a definitive conclusion of the fiber size and therefore type is somewhat premature, future observations should be conducted in wet environment to reveal the real nature of these features.

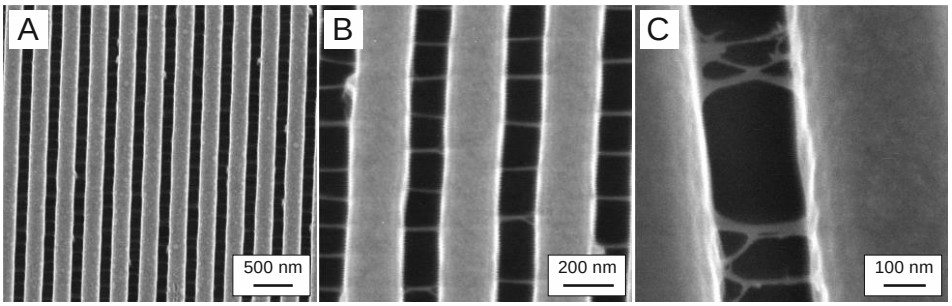

Figure 32. Helium Ion Microscope micrographs of 300 nm pitch SiO_2–CH_3 specimens after adsorption of collagen. The concentration of collagen in PBS was 15.5 μg ml^{-1}, incubation time 2 h. HIM was acquired with a 30 keV He beam. (A) Overview of the structure field of view 5 μm; (B) Distinct collagen fibers bridging the nanoridges, field of view 1 μm; (C) Zoom-in detail of a number of few collagen fibers in-between the nanoridges, field of view 700 nm.

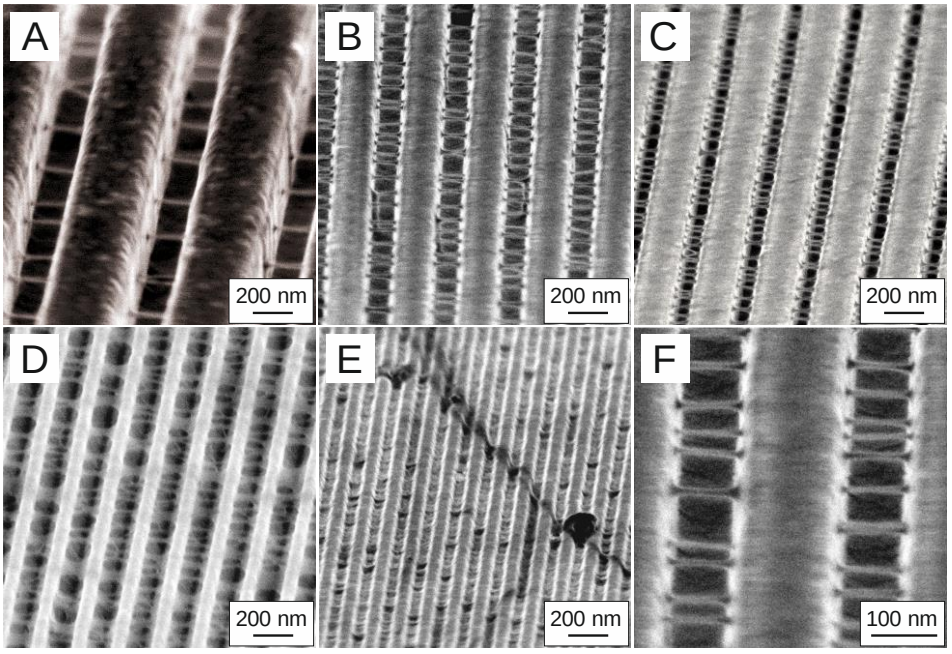

Figure 33. HRSEM micrographs of all 6 types of SiO_2–CH_3 nanostructures used in the collagen adsorption experiments. The self-organized collagen is bridging the grooves of structure for all pitch sizes. The initial concentration of collagen in PBS was 15.5 μg ml^{-1}

(see text for processing details). The shown structures are SiO_2–CH_3 with a pitch of: (A) 600 nm; (B) 300 nm 1:1 R:G; (C) 300 nm 3:1 R:G; (D) 200 nm 1:3 R:G; (E) 150 nm R:G; (F) zoom-in detail on 300 nm 1:1 R:G.

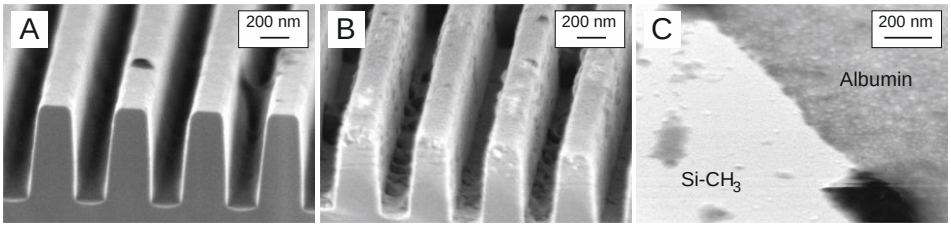

Figure 34. High resolution SEM images of adsorbed albumin, using an albumin concentration of 22.5 μg ml^{-1} for one hour. (A) Albumin on SiO_2-OH surface with pitch 600 nm; (B) Albumin on SiO_2–CH_3 surface with pitch 600 nm; (C) Albumin on flat surface with scratched-away zone (right side of picture). The Z contrast between SiO_2 and carbon-rich protein is noticeable.

5.4. Discussion

Although the error of measurement and the spread in the results is significant, some conclusions about protein adsorption on the tested surfaces, and in particular about differences in adsorption behavior between the three proteins on SiO_2–CH_3 and SiO_2-OH, can still be drawn. For BSA and FN the data show that for most specimens adsorption is significantly more pronounced (by about a factor of 2) on the hydrophobic, compared to the hydrophilic, nanostructured specimens. For the control specimens not carrying nanostructure, the difference however is small, within the error. For COL-I this difference between hydrophobic and hydrophilic surfaces is much smaller, within error, these surfaces show more or less the same behavior.

The accuracy of the method does not allow us to draw direct conclusions about the effect of the distinct nanostructures on protein adsorption. The data indicate that the amount of adsorbed protein is not following the surface area gain

introduced by the nanostructures, which gain can be up to a factor of 3 (see Table 9).

The large spread between adsorption data indicates that the chosen measurement method is not suitable for the available amount of surface area and even less for the surface area gain by nanostructuring. A more sensitive method is required, e.g., a method based on fluorescence [29,30], radiolabelling [12,31,32] or immunolabelling, quartz crystal microbalance and others.

5.5. Conclusions

Additional conclusion that can be drawn is that in case of fibronectin (FN) and albumin (ALB) the adsorption is influenced by nanostructure, however in case of collagen (COL) no significant change of adsorption can be observed on different chemistries and structure types. However, general trend observed is that SiO_2–CH_3 terminated surface adsorbs significantly higher amount of protein than SiO_2–OH, and in case of SiO_2–CH_3 terminated surface the quantity of adsorbed protein is corresponding with available surface area on nanostructured samples. The amounts of adsorbed protein on flat SiO_2–CH_3 and SiO_2–OH surfaces are similar for all protein types. In case of collagen there is no significant difference in adsorption on SiO_2–CH_3 and SiO_2–OH surfaces which may be explained by the fact that collagen self-organizes, as shown in the HIM and HRSEM study.

1 Brash John, L. & Horbett Thomas, A. in *Proteins at Interfaces II* Vol. 602 *ACS Symposium Series* Ch. 1, 1-23 (American Chemical Society, 1995).

2 Somasundaran, P. *Encyclopedia of Surface And Colloid Science*. (CRC Press, 2006).

3 Nel, A. E., Madler, L., Velegol, D., Xia, T., Hoek, E. M. V., Somasundaran, P., Klaessig, F., Castranova, V. & Thompson, M. Understanding biophysicochemical interactions at the nano-bio interface. *Nat Mater* **8**, 543-557 (2009).

4 Lord, M. S., Foss, M. & Besenbacher, F. Influence of nanoscale surface topography on protein adsorption and cellular response. *Nano Today* **5**, 66-78 (2010).

5 Jonsson, U., Ivarsson, B., Lundstrom, I. & Berghem, L. Adsorption Behavior of Fibronectin on Well-Characterized Silica Surfaces. *J Colloid Interf Sci* **90**, 148-163 (1982).

6 Lord, M. S., Cousins, B. G., Doherty, P. J., Whitelock, J. M., Simmons, A., Williams, R. L. & Milthorpe, B. K. The effect of silica nanoparticulate coatings on serum protein adsorption and cellular response. *Biomaterials* **27**, 4856-4862 (2006).

7 Grinnell, F. & Feld, M. K. Fibronectin Adsorption on Hydrophilic and Hydrophobic Surfaces Detected by Antibody-Binding and Analyzed during Cell-Adhesion in Serum-Containing Medium. *Journal of Biological Chemistry* **257**, 4888-4893 (1982).

8 Erickson, H. P. & Carrell, N. A. Fibronectin in Extended and Compact Conformations - Electron-Microscopy and Sedimentation Analysis. *Journal of Biological Chemistry* **258**, 4539-4544 (1983).

9 Feinberg, A. W. & Parker, K. K. Surface-Initiated Assembly of Protein Nanofabrics. *Nano Lett* **10**, 2184-2191 (2010).

10 Haynes, C. A. & Norde, W. Structures and Stabilities of Adsorbed Proteins. *J Colloid Interf Sci* **169**, 313-328, (1995).

11 Wilson, C. J., Clegg, R. E., Leavesley, D. I. & Pearcy, M. J. Mediation of biomaterial-cell interactions by adsorbed proteins: a review. *Tissue Eng* **11**, 1-18, (2005).

12 Kasemo, B. Biological surface science. *Current Opinion in Solid State and Materials Science* **3**, 451-459 (1998).

13 Bergkvist, M., Carlsson, J. & Oscarsson, S. Surface-dependent conformations of human plasma fibronectin adsorbed to silica, mica, and hydrophobic surfaces, studied with use of Atomic Force Microscopy. *Journal of Biomedical Materials Research Part A* **64A**, 349-356 (2003).

14 Lösche, M. Protein monolayers at interfaces. *Current Opinion in Solid State and Materials Science* **2**, 546-556 (1997).

15 Noh, H. & Vogler, E. A. Volumetric interpretation of protein adsorption: competition from mixtures and the Vroman effect. *Biomaterials* **28**, 405-422 (2007).

16 Barnthip, N., Noh, H., Leibner, E. & Vogler, E. A. Volumetric interpretation of protein adsorption: Kinetic consequences of a slowly-concentrating interphase. *Biomaterials* **29**, 3062-3074 (2008).

17 Noh, H., Yohe, S. T. & Vogler, E. A. Volumetric interpretation of protein adsorption: Ion-exchange adsorbent capacity, protein pI, and interaction energetics. *Biomaterials* **29**, 2033-2048 (2008).

18 Barnthip, N., Parhi, P., Golas, A. & Vogler, E. A. Volumetric interpretation of protein adsorption: Kinetics of protein-adsorption competition from binary solution. *Biomaterials* **30**, 6495-6513 (2009).

19 Parhi, P., Golas, A., Barnthip, N., Noh, H. & Vogler, E. A. Volumetric interpretation of protein adsorption: Capacity scaling with adsorbate molecular weight and adsorbent surface energy. *Biomaterials* **30**, 6814-6824 (2009).

20 Dewez, J. L., Lhoest, J. B., Detrait, E., Berger, V., Dupont-Gillain, C. C., Vincent, L. M., Schneider, Y. J., Bertrand, P. & Rouxhet, P. G. Adhesion of mammalian cells to polymer surfaces: from physical chemistry of surfaces to selective adhesion on defined patterns. *Biomaterials* **19**, 1441-1445 (1998).

21 Hertl, W. & Hair, M. L. Reaction of hexamethyldisilazane with silica. *Journal of Physical Chemistry* **75**, 2181-2185 (1971).

22 Klapetek, P., Nečas, D. & Anderson, C. <http://gwyddion.net/> (Accesed June 2011).

23 Othman, M. T., Lubguban, J. A., Lubguban, A. A., Gangopadhyay, S., Miller, R. D., Volksen, W. & Kim, H.-C. Characterization of porous low-k films using variable angle spectroscopic ellipsometry. *Journal of Applied Physics* **99**, 083503 (2006).

24 Imamura, K., Shimomura, M., Nagai, S., Akamatsu, M. & Nakanishi, K. Adsorption characteristics of various proteins to a titanium surface. *Journal of Bioscience and Bioengineering* **106** (2008).

25 Ward, B. W., Notte, J. A. & Economou, N. P. 6 edn, 2871-2874 (AVS).

26 Azioune, A., Siroti, F., Tanguy, J., Jouini, M., Chehimi, M. M., Miksa, B. & Slomkowski, S. Interactions and conformational changes of human serum albumin at the surface of electrochemically synthesized thin polypyrrole films. *Electrochim Acta* **50**, 1661-1667 (2005).

27 Tidwell, C. D., Castner, D. G., Golledge, S. L., Ratner, B. D., Meyer, K., Hagenhoff, B. & Benninghoven, A. Static time-of-flight secondary ion mass spectrometry and x-ray photoelectron spectroscopy characterization of adsorbed albumin and fibronectin films. *Surf Interface Anal* **31**, 724-733 (2001).

28 Molder, J. F., Stickle, W. F., Sobol, P. E. & D., B. K. *Handbook of X-ray Photoelectron Spectroscopy*. (Perkin-Elmer Corporation, Eden Prairie, 1992).

29 Li, N. & Ho, C.-M. Patterning Functional Proteins with High Selectivity for Biosensor Applications. *Journal of the Association for Laboratory Automation* **13**, 237-242 (2008).

30 Mooney, J. F., Hunt, A. J., McIntosh, J. R., Liberko, C. A., Walba, D. M. & Rogers, C. T. Patterning of functional antibodies and other proteins by photolithography of silane monolayers. *Proc Natl Acad Sci U S A* **93**, 12287-12291 (1996).

31 Barrias, C. C., Martins, M. C. L., Almeida-Porada, G., Barbosa, M. A. & Granja, P. L. The correlation between the adsorption of adhesive proteins and cell behaviour on hydroxyl-methyl mixed self-assembled monolayers. *Biomaterials* **30**, 307-316 (2009).

32 Unsworth, L. D., Sheardown, H. & Brash, J. L. Polyethylene oxide surfaces of variable chain density by chemisorption of PEO-thiol on gold: Adsorption of proteins from plasma studied by radiolabelling and immunoblotting. *Biomaterials* **26**, 5927-5933 (2005).

6.

THE INFLUENCE OF NANOSCALE GROOVED SUBSTRATES ON OSTEOBLAST BEHAVIOR AND EXTRACELLULAR MATRIX DEPOSITION[2]

Abstract

To fight bone diseases characterized by poor bone quality like osteoporosis and osteoarthritis, as well as in reconstructive surgery, there is a need for a new generation of implantable biomaterials. It is envisioned that implant surfaces can be improved by mimicking the natural extracellular matrix of bone tissue, which is a highly organized nano-composite. In this study we aimed to get a better understanding of osteoblast response to nanometric grooved substrates varying in height, width and spacing. A throughput screening biochip was created using electron beam lithography. Subsequently, uniform large-scale nanogrooved substrates were created using laser interference lithography and reactive ion etching. Results showed that osteoblasts were responsive to nanopatterns down to 75 nm in width and 33 nm in depth. SEM and TEM studies showed that an osteoblast-driven calcium phosphate (CaP) mineralization was observed to follow the surface pattern dimensions.

[2] This chapter is based on paper published in Biomaterials Volume 31, Issue 12, April 2010, Pages 3307-3316.

Strikingly, aligned mineralization was found on even smaller nanopatterns of 50 nm in width and 17 nm in depth. A single cell based approach for real time PCR demonstrated that osteoblast-specific gene expression was increased on nanopatterns relative to a smooth control. The results indicate that nanogrooves can be a very promising tool to direct the bone response at the interface between an implant and the bone tissue.

6.1. Introduction

The use of implants has become a common treatment for end stage destructive joint diseases like osteoporosis, osteoarthritis and bone tumors. These bone diseases are characterized by poor bone quality, decreased bone formation or increased bone resorption. Current therapy includes the replacement of damaged tissue by the installation of an implant. To increase the lifespan of implants in these compromised patients, there is a need for a new generation of implantable biomaterials, for which it is supposed that improvement of initial bone tissue response should lead to long-term implant stability [1]. This initial response depends on several factors, but most important are the interface interactions between bone tissue and the biomaterial surface. Key parameters are surface wettability and surface topography [2]. Cells are known to be very sensitive to the surface topographical environment and recognize surface topographical alterations, which subsequently can induce changes in the cytoskeleton, cell shape and differentiation[3]. Besides this cellular effect, surface nanostructure can serve as a template to control the initiation and growth of apatite crystals, the major building block of bone tissue [4]. In this context it is envisioned that one approach to improve interface interactions between implants and the surrounding bone tissue is by mimicking the natural extracellular matrix (ECM) of bone tissue in order to stimulate osteoblast adhesion, proliferation and differentiation. The natural bone ECM is a highly organized nanocomposite, consisting of molecules like collagen type-1 and hydroxyapatite [5,6]. Collagen type-I forms fibrils with an interfibrillar spacing of 68 nm and 35 nm depth. The

hydroxyapatite crystals are embedded in these fibrils [6] and have an average size of 50 × 25 × 4 nm^3. The bone surface has an average roughness value (R_a) of 32 nm [7]. Many groups have already verified the effect of mimicking the bone surface nanoroughness using various biomaterials [7-18] and showed a beneficial effect of nano-roughness on osteoblast proliferation [8,9,13,14]. However in all these studies, nanometric surface structures were formed by random processes like self-organization via polymer demixing, colloidal lithography, acid etching or grinding [11,12,16]. The response of osteoblasts to ordered textures has also been reported, but merely on a micrometer (i.e. > 1 μm) or sub-micrometer topography (i.e. 1 μm > 100 nm) [19-21]. It is shown that cells are especially responsive to groove/ridge patterns and on such surfaces aligned as well as migrated along the groove direction. Also ECM formation [22] and mineral deposition has been shown to be promoted along such sub-micrometer grooves [21]. However, so far most studies focused on the cell response to grooves with only one dimension (either depth or width) in the nanometer scale (i.e. 1–100 nm), while leaving the other dimension always at micron or just submicron-scale, i.e. considerably larger than the natural bone ECM [20,21,23,24].

In this paper, we report on the response of osteoblast-like cells to grooved substrates nanometric in all dimensions. Several aspects of the cellular response were studied, i.e., (1) adjustment of the shape of osteoblasts and the position of focal adhesions, (2) the interface between osteoblast-like cells and substrates, and (3) gene expression profiles.

6.2. Materials and methods

6.2.1. Substrates

A silicon biochip containing 50 different nanometric patterns was generated using electron beam lithography (EBL) as described by Loesberg et al. [25] employing Hydrogen Silsesquioxane resist, as described by van Delft et al. [26,27]. The field patterns consisted of squares of 500 × 500 μm containing patterns

with nanogroove-to-ridge ratios of 1:1, 1:3 and 3:1. As a control for cellular orientation, silicon substrates with microgrooves (depth of 0.25 μm and a pitch of 2 μm [28]), as well as smooth substrates were used. All silicon substrates were used as templates for the production of polystyrene (PS; Acros, Geel, Belgium) replicates for cell culture [28].

6.2.2. Large scale uniform nanogrooved substrates created with laser interference lithography

After screening of the biochip, also large scale, uniformly nanogrooved silicon wafers were created using laser interference lithography (LIL). A setup was used based on the Lloyd's interferometer, where a regular pattern was produced by interference of an incident laser beam and a mirror reflected beam [29]. The period of the interference pattern, and thus of the grating recorded in the resist layer on the substrate, is given by the equation: $P = \lambda / (2 \sin \theta)$ where the period (P) is determined by the wavelength (λ) of the beam source and the angle (θ) at which two coherent beams are interfering. With a 266 nm light source, periods of 150 nm up to 1000 nm were produced [30]. An optimized antireflective photoresist layer was spin coated on a silicon wafer. After illumination and development of the resist layer, the grating was transferred to the substrate by a reactive ion etching process using a Plasmatherm 790 system (Unaxis, Utrecht, The Netherlands). An optimized method of reactive ion etching using parameters giving anisotropic etch profiles in nanoscale was used. SF_6:O_2 plasma chemistry gave well defined structures transferred on silicon. Using this setup, highly regular patterns were produced over areas of about 2 × 2 cm^2.

6.2.3. Polystyrene replicas

For the reproduction of the PS replicas, 0.5 g PS dissolved in 3 mL chloroform was casted onto a 3″ silicon wafer and the chloroform was evaporated. PS rings (2.0 cm) were glued to substrates using a small amount of casting solution to create cell culture dishes. Substrates received a radiofrequency glow-discharge

(RFGD; Harrick, Ossining, USA) treatment for 5 min at 10^{-2} mbar for sterilization and to improve wettability.

6.2.4. Atomic force microscopy (AFM)

Surface topography was quantitatively evaluated using a Dimension atomic force microscope (AFM; Dimension 3100, Veeco, Santa Barbara, CA). Tapping in ambient air was performed with 118 μm long silicon cantilevers (NW-AR5T-NCHR, NanoWorld AG, Wetzlar, Germany) with average nominal resonant frequencies of 317 kHz and average nominal spring constants of 30 N m^{-1}. This type of AFM probe has a high aspect ratio (7:1) portion of the tip with a nominal length of >2 μm and a half-cone angle of <5°. Nominal radius of curvature of the AFM probe tip was less than 10 nm. The probes are especially suited to characterize the manufactured nanogrooves.

Height images of each field/sample were captured in ambient air at 50 % humidity at a tapping frequency of 266.4 kHz. The analyzed field was scanned at a scan rate of 0.5 Hz and 512 scanning lines. Nanoscope imaging software (version 6.13r1, Veeco) was used to analyze the resulting images. Surface roughness, root mean squared (RMS, nm) and depth (nm) were obtained and averaged for three random fields per substrate.

6.2.5. Cell culture

Osteoblast-like cells were obtained as described before [31]. Briefly, femurs of 40–43 day old male Wistar WU rats (local approval number DEC 2004156). The femurs were washed three times in alpha Minimal Essential Medium (αMEM; Gibco, Invitrogen Corp., Paisley, Scotland) with 0.5 mg mL^{-1} gentamycin and 3 μg mL^{-1} fungizone. The epiphyses were removed and the diaphyses were flushed out cell culture medium containing 10 % fetal calf serum (Gibco), 50 μg mL^{-1} ascorbic acid (Sigma–Aldrych, Zwijndrecht, the Netherlands), 10 mm Na-β-glycerophosphate (Sigma), 10^{-8} M dexametasone (Sigma) and 50 μg mL^{-1}gentamycin (Gibco).

After one day medium was refreshed to remove non-adherent cells. After 7 days of primary culture, cells were detached with trypsin/EDTA (0.25 % w/v trypsin/0.02 % EDTA) and seeded onto the substrates at 10^4 cells cm^{-2}.

6.2.6. Cellular orientation

At 24 h, cells were washed in PBS and fixed for 10 min in 3 % formaldehyde (PFA; Sigma–Aldrych) and 0.02 % glutaraldehyde (Acros) in PBS. Cells were permeabilized in 1 % Triton X100 (Koch, Colnbrook, England) in PBS for 5 min and subsequently incubated with PBS containing 5 % BSA (Sigma) for 30 min to block aspecific epitopes. Actin filaments of cells were fluorescently stained with Alexa-fluor 568 conjugated phalloidin (1:200 Molecular probes, Invitrogen Corp., Paisley, Scotland) diluted in PBS containing 1 % BSA and 0.1 % Tween-20 (Merck, Schuchardt, Germany). The specimens were examined using an Olympus FV1000 confocal laser scanning microscope (CLSM, Olympus, Center Valley, USA).

Orientation of osteoblast-like cells on grooved substrates was examined by taking photographs of cells and determining the angle relative to the line direction. The images were analysed with ImageJ software (Image J, La Jolla, USA). Inclusion criteria for cells were: the cell was not in contact with other cells and the cell was not in contact with the image perimeter. Statistical analysis was performed using SPSS for Windows (SPSS14.0, Chicago, USA).

6.2.7. Immunofluorescence staining

After 24 h, osteoblast-like cells were washed 3 times in PBS and fixed for 10 min in 3 % PFA and 0.02 % glutaraldehyde in PBS and permeabilized in 1 % Triton X100 in PBS for 5 min. Cells were then incubated in PBS containing 5 % BSA for 30 min to block aspecific epitopes. α-Vinculin labelling was performed overnight with mouse monoclonal primary antibodies (1:500; Sigma) in PBS containing 1 % BSA and 0.1 % Tween-20. This incubation step was followed by incubation with goat anti-mouse secondary antibody Alexa-fluor 488 conjugated IgG (1:200; Molecular Probes, Invitrogen), Alexa-fluor 568

conjugated phalloidin for F-actin fluorescence (1:200; Molecular probes) and DAPI staining for nucleic UV-visualization (1:2500) diluted in PBS containing 1 % BSA and 0.1 % Tween-20 for 2 h at room temperature. Finally, the specimens were examined with an Olympus FV1000 CLSM.

6.2.8. Transmission electron microscopy (TEM)

Osteoblast-like cells were cultured for 12 and 16 days and subsequently washed in PBS, fixed in 2 % glutaraldehyde in 0.1 M sodium-cacodylate for 5 min and washed in 0.1 M sodium-cacodylate. Subsequently cells were post-fixed in 1 % OsO_4 for 60 min and dehydrated in a graded series of ethanol (5 min in 70 %, 80 %, 90 %, 96 %, 100 % ethanol and finally 100 % filtered ethanol). The patterned areas were then cut into pieces and embedded in epoxy resin (Electron Microscopy Sciences, Hatfield, USA). The specimens were first incubated overnight in a mixture of 1:1 Epoxy resin : EtOH 100 %, washed three times in pure epoxy resin and then incubated overnight in pure epoxy resin. The epoxy resin was polymerized at 65 °C. After polymerization ultrathin sections of approximately 130 nm thickness were cut for TEM analysis using a diamond knife (Diatome) and collected on 100 mesh grids (Electron microscopy sciences, Hatfield, USA). After drying, sections were stained in uranyl acetate for 30 min and subsequently in lead citrate for 10 min. Sections were examined with a JEOL TEM 1010 (Nieuw Vennep, the Netherlands). The electron dense areas observed with TEM, were further analyzed using EDX-TEM analysis (FEI, Eindhoven, The Netherlands).

6.2.9. Scanning electron microscopy (SEM)

At 3, 8 and 16 days, cells were washed in PBS, fixed for 5 min in 2 % glutaraldehyde in 0.1 M sodium-cacodylate and washed for 5 min in 0.1 M sodium-cacodylate. Fixed cells were dehydrated in a graded series of ethanol (5 min in 70 %, 80 %, 90 %, 96 %, 100 % ethanol and finally 100 % water free ethanol) and dried to air in tetramethylsilane. The specimens were sputter-coated with gold (10 nm) and examined with a Jeol 6310 SEM.

6.2.10. RNA isolation and reverse transcriptase PCR

Cells were cultured for 12 h, 48 h and 5 days, washed 3 times in PBS and subsequently excised from nanogrooved substrates of 1000 nm, 300 nm and 150 nm groove pitch. Since cells were seeded at such a low density, conventional reverse transcriptase and QPCR was replaced by a single-cell based approach as described by Shieh et al. [32]. mRNA isolation was performed using the Absolutely RNA® Nanoprep kit (Stratagene, La Jolla, USA) according to manufacturer's protocol. Briefly, the cells were lysed in 100 µL of lysis buffer containing 0.7 µL of β-mercaptoethanol. Subsequently 100 µL EtOH 70 % was added, thoroughly mixed and transferred into an RNA-binding nano-spin cup. The sample was centrifuged at 12000 × *g* for 60 s, the filtrate was discarded and 300 µL of low-salt wash buffer was added. The sample was centrifuged and the filtrate was removed. 15 µL of DNase-solution (2.5 µL RNase-Free DNase-I mixed with 12.5 µL DNase digestion buffer) was added to the sample and incubated for 15 min at 37 °C. 300 µL of high-salt wash buffer was added to and subsequently centrifuged at 12000 × *g* for 1 min. The filtrate was discarded, 300 µL low-salt wash buffer was added to the spin-cup and centrifuged. 8 µL of Elution buffer was added to the sample and incubated for 2 min at room temperature. The sample was collected by centrifugation at 12000 × *g* for 5 min.

After obtaining the mRNA, a first strand reverse transcriptase PCR was performed using the Superscript™ III First-strand Synthesis System for RT-PCR (Invitrogen) according to manufacturer's protocol. The collected 8 µL of mRNA was incubated with 1 µL of dNTPs (1 mM end concentration), 0.5 µL random hexamers and 0.5 µL oligo $(dT)_{20}$ primers (both 0.5 µM end concentration) for 5 min at 65 °C to anneal the primers to the mRNA. The following components were subsequently added: 2 µL 10 × reaction buffer, 4 µL 25 mm $MgCl_2$, 2 µL 0.1 M DTT, 1 µL RNaseOUT (40 U μL^{-1}) and 1 µL superscript III RT (200 U μL^{-1}). The reaction mix was incubated for 10 min at 25 °C for further primer annealing, 50 min at 50 °C for reverse transcription and

5 min at 85 °C to terminate the reaction. Then 1 μL RNase H was added to the tube and incubated for 20 min at 37 °C for RNA digestion. This solution was stored at −20 °C until further use.

6.2.11. Real time PCR

The cDNA will then be amplified and specific gene expression is quantified in a real-time PCR. For this reaction, 12.5 μL master mix, 2 μL DNA, 3 μL primer mix (1.5 μL forward primer and 1.5 μL reverse primer are mixed) and 7.5 μL DEPC. Subsequently the PCR is performed in a Real-Time PCR reaction apparatus with the desired temperatures. The used primers were from β1-integrin, β3-integrin, collagen type-I, alkaline phosphatase (ALP), osteocalcin (OCN), osteopontin (OPN) and β-actin (sequences are given in Table 10. Overview of the sequences of the used primers.). The expression of the tested genes was calculated via the $2^{-\Delta\Delta Ct}$ method [33] relative to smooth controls. Statistical analysis was performed using SPSS for Windows (SPSS 14).

Table 10. Overview of the sequences of the used primers.

Primer	Sequence
Col-I	F5′-AACCCGAGGTATGCTTGATCT-3′
	R5′-CCAGTTCTTCATTGCATTGC-3′
ALP	F5′-GGGACTGGTACTCGGATAACGA-3′
	R5′-CTGATATGCGATGTCCTTGCA-3′
Cbfα1	F5′-GCCACACTTTCCACACTCTC-3′
	R5′-CACTTCTGCTTCTTCGTTCTC-3′
OCN	F5′-CGGCCCTGAGTCTGACAAA-3′
	R5′-GCCGGAGTCTGTTCACTACCTT-3′
BSP	F5′-TCCTCCTCTGAAACGGTTTCC-3′
	R5′-GGAACTATCGCCGTCTCCATT-3′
β-Actin	F5′-TTCAACACCCCAGCCATGT-3′
	R5′-TGTGGTACGACCAGAGGCATAC-3′
Int α1	F5′-AGCTGGACATAGTCATCGTC-3′
	R5′-AGTTGTCATGCGATTCTCCG-3′
Int β1	F5′-AATGTTTCAGTGCAGAGCC-3′
	R5′-TTGGGATGATGTCGGGAC-3′

GapdH	F5′-TCCTGCACCACCAACTGCTT-3′
	R5′-GAGGGGCCATCCACAGTCTT-3′

6.3. Results

6.3.1. Substrates

Biochip templates and PS replicates were routinely checked by atomic force microscopy (AFM) (Figure 35 a, b) and scanning electron microscopy (SEM) (Figure 35 c, d). The dimensions are summarized in Table 11.

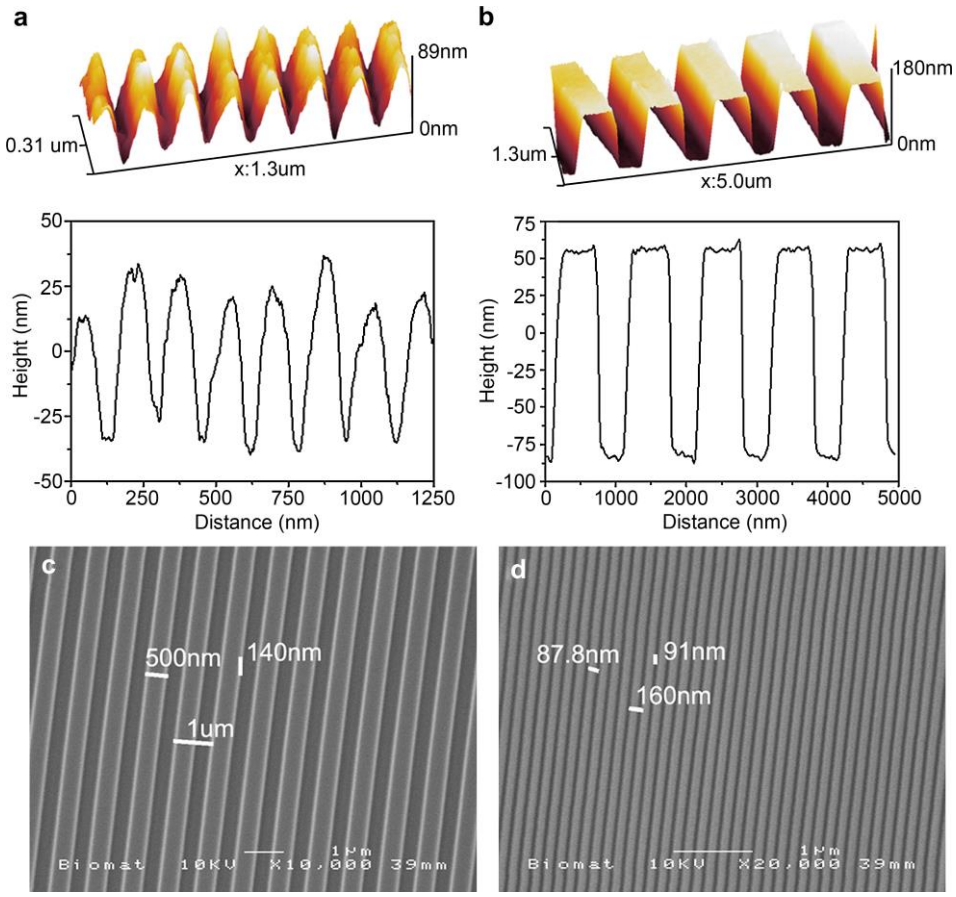

Figure 35. Three-dimensional (3D) AFM topography image and height profile of silicon wafers with groove dimensions of (a) a width of 300 nm and a depth of 158 nm. 3D AFM

topography image and height profile of a PS-substrate with (b) a width of 500 nm and a depth of 153 nm. SEM graphs of PS-substrates with a width of (c) 500 nm and (d) 80 nm.

Table 11. Feature dimensions of topographically patterned substrata.

E-beam derived biochip		
Pitch (nm)	Depth (nm + SE)	Roughness (nm ± SE)
1000	153.3 ± 2.7	69.1 ± 1.0
600	158.0 ± 3.2	64.4 ± 0.7
400	149.2 ± 1.2	53.9 ± 1.8
300	119.9 ± 2.6	36.7 ± 1.3
200	77.4 ± 4.1	22.0 ± 0.5
160	51.9 ± 3.4	15.3 ± 0.3
100	17.2 ± 3.5	9.2 ± 0.7
80	15.3 ± 1.9	8.7 ± 0.9
60	11.6 ± 1.1	8.3 ± 0.1
40	10.9 ± 1.1	6.6 ± 0.4
2000	353.9 ± 8.2	163.3 ± 10.5
LIL-derived substrates		
1000	158 ± 10	
600	122.3 ± 10	
300	48.6 ± 1.8	31
200	51.8 ± 2.7	27
150	32.7 ± 2.0	18

Similar large-scale nanotextures of 2 × 2 cm^2 were produced using laser interference lithography (LIL) followed by reactive ion etching (RIE). This technique was applied to facilitate both qualitative and quantitative *in vitro* studies. The LIL-derived silicon substrates and the PS replicates were analyzed using AFM and SEM (PS replicates are shown in Figure 36 and a list of dimensions is given in Table 11)

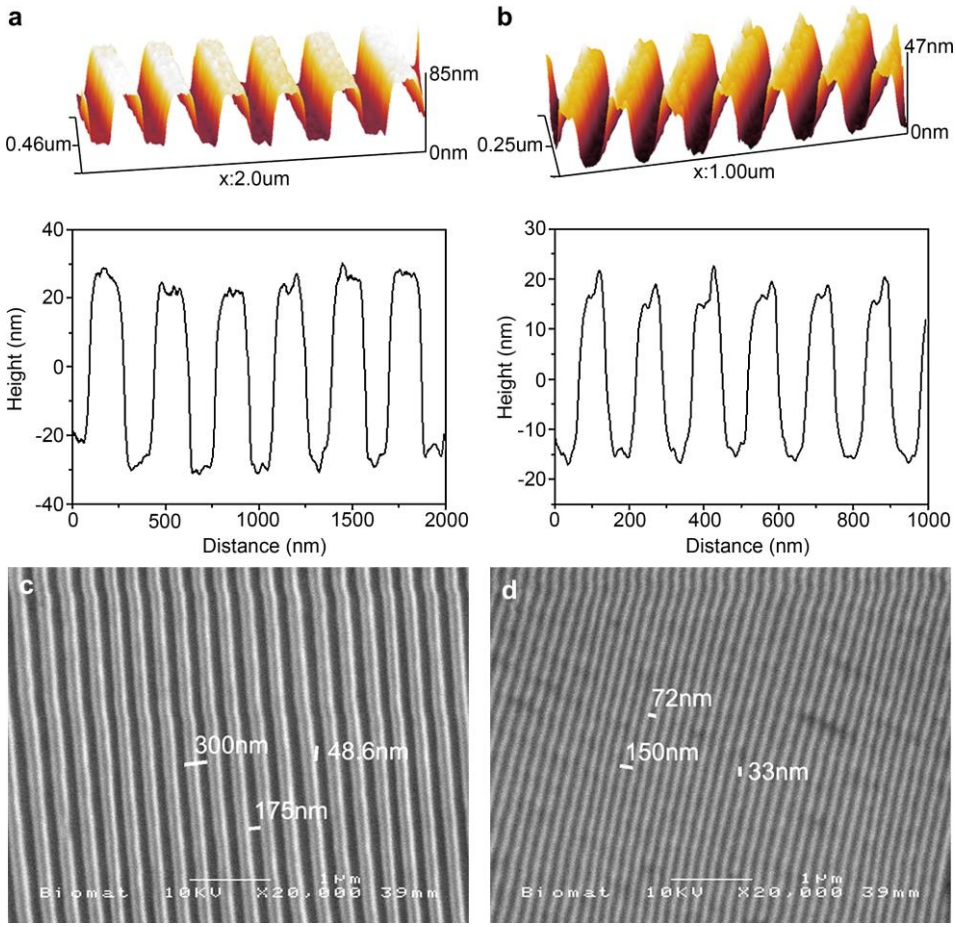

Figure 36. 3D AFM topography image and height profiles of LIL-derived PS-substrates with a width of (a) 150 nm (49 nm depth) and (b) 75 nm (33 nm depth). SEM graphs of substrates with a width of (c) 150 nm and (d) 75 nm.

6.3.2. Cellular orientation

The studied groove/ridge patterns had an evident effect on osteoblast morphology, and were found to induce alignment of the osteoblast cell shape and internal F-actin filaments (Figure 37 a). On textures with sizes equivalent to the natural bone ECM (i.e. a groove width of 150 – 75 nm and depth down to 33 nm; region between red lines in Figure 37 c) a clear interaction between the grooves and cells resulting in alignment was found, while on dimensions with a

width of 50 nm and a 17 nm depth or smaller (Figure 37 b) cells did spread randomly. An analysis of the alignment is shown quantitatively in a Box–Whisker plot (Figure 37 c). Alignment of osteoblasts on the LIL-derived substrates was similar to the corresponding biochip dimensions (Figure 37 c, asterisks).

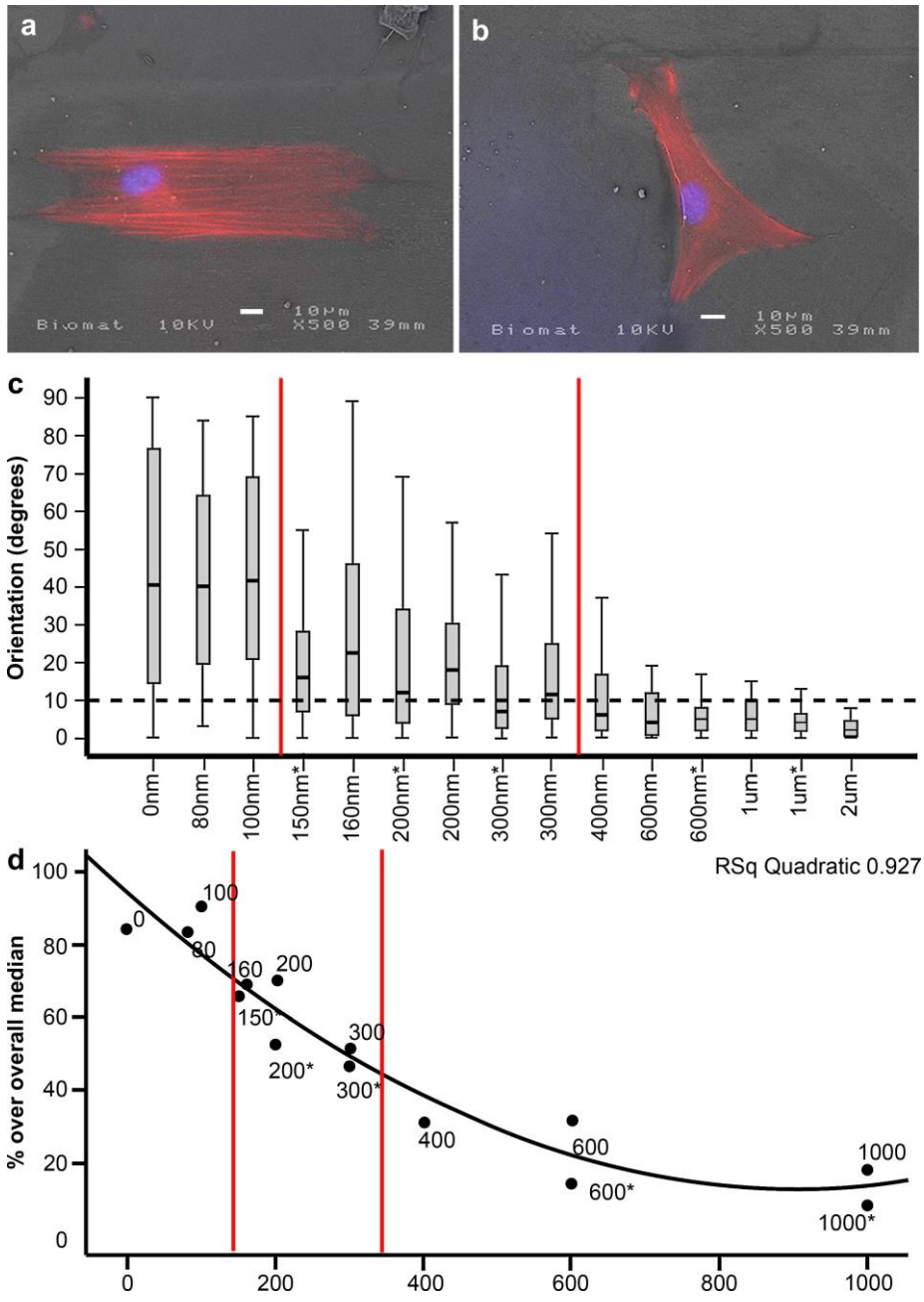

Figure 37. Cell alignment of osteoblast-like cells to grooved substrates (overlay fluorescence and SEM image). Cells were stained for F-actin (red) and the nucleus (DAPI): (a) with a width of 150 nm (120 nm depth) and (b) a width of 50 nm (17 nm depth). (c) A

Box-Whisker plot showing the cellular alignment to the nanogrooves (a median of 45° is random orientation). The median is marked in the box and the box-corners indicate the 25th to 75th percentiles. Note that cells start to align to nanopatterns from a minimal groove width of 75 nm (33 nm depth). The overall median orientation is 10° (dotted line). Asterisks represent the LIL-derived substrates. (d) Scatter plot of percentage of osteoblasts on the grooved patterns that are higher than the average median of 10°. The trend analysis demonstrates a groove dependent decrease of cellular orientation (R^2 of trendline is 0.93). The regions between the red lines are indicating the pattern sizes that are considered equivalent in size to the ECM.

A trend analysis of deviation of osteoblast alignment from the average median of all data (10°, red line in Figure 37 c) in Figure 37 d showed that: (1) cells aligned to sub micrometer grooves, and (2) osteoblast alignment gradually decreased with decreasing groove widths (p-value < 0.01). This phenomenon was persistent down to a groove width of 75 nm and depth of 33 nm. Below this point cells did not morphologically recognize surface topography anymore. This dimension can therefore be considered a threshold point for morphological nanopattern recognition by osteoblasts.

6.3.3. Focal adhesions

It was observed that focal adhesions were mainly oriented to the groove direction on groove widths down to 150 nm (and 120 nm depth) (Figure 38 a, b), whereas focal adhesions were oriented randomly on surfaces with a groove width of less than 50 nm (and depth of 17 nm) (Figure 38 c). In agreement with cellular alignment, a decreasing groove pitch resulted in decreased focal adhesion alignment (Figure 38 b). Higher magnification imaging revealed that the aligned focal adhesions tended to reside on top of the ridges (Figure 38 d).

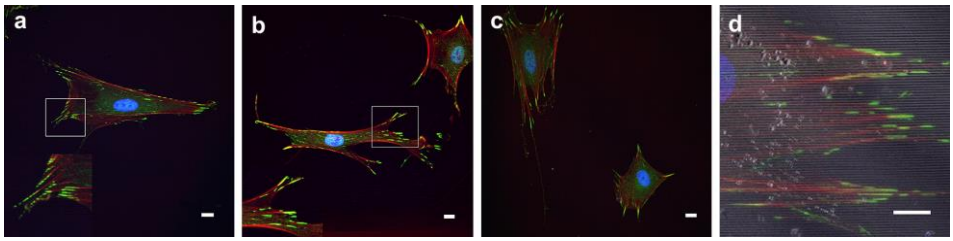

Figure 38. Immunofluorescence micrograph of osteoblast-like cells cultured on nanogrooved substrates. Focal adhesions (α-vinculin, green) on a groove width of (a) 500 nm (153 nm depth) were mostly aligned with the groove direction, whereas alignment of focal adhesions to a groove width of (b) 150 nm (120 nm depth) had diminished and was random on a groove width of (c) 50 nm (17 nm depth). (d) An overlay of a fluorescent micrograph with a light micrograph. α-Vinculin staining on a width of 300 nm (158 nm depth) shows that focal adhesions mainly reside on top of the ridges. Green, vinculin; red, F-actin; blue, nuclei. Bars: 10 μm.

6.3.4. Transmission and scanning electron microscopy

TEM images demonstrated that cells descended into grooves (Figure 39 b). The electron dense material deposited in between the grooves at the interface between cells and substrate surface (asterisks in Figure 39 a and c) was analyzed with energy dispersive X-ray analysis (EDX) and confirmed to be calcium and phosphorous (asterisks in Figure 39, EDX in Figure 39 d). Additional electron dense areas (arrowheads in Figure 39) as seen in TEM were found to consist of CaP and proteins (mainly collagen, arrows in Figure 39) which corresponds to the formation of an extracellular mineralized matrix. Comparison of TEM sections at 12 and 16 days demonstrated that cell bodies in time are gradually driven away from the interface by a mineralized ECM; after 12 days of culture, osteoblasts resided inside the nanogrooves and only a small amount of CaP was shown to be deposited on the bottom of the grooves below the cells (Figure 39 b). However, after 16 days the interface consisted of a thick extracellular mineralized matrix layer produced by osteoblasts covering the ridges (Figure 39 c).

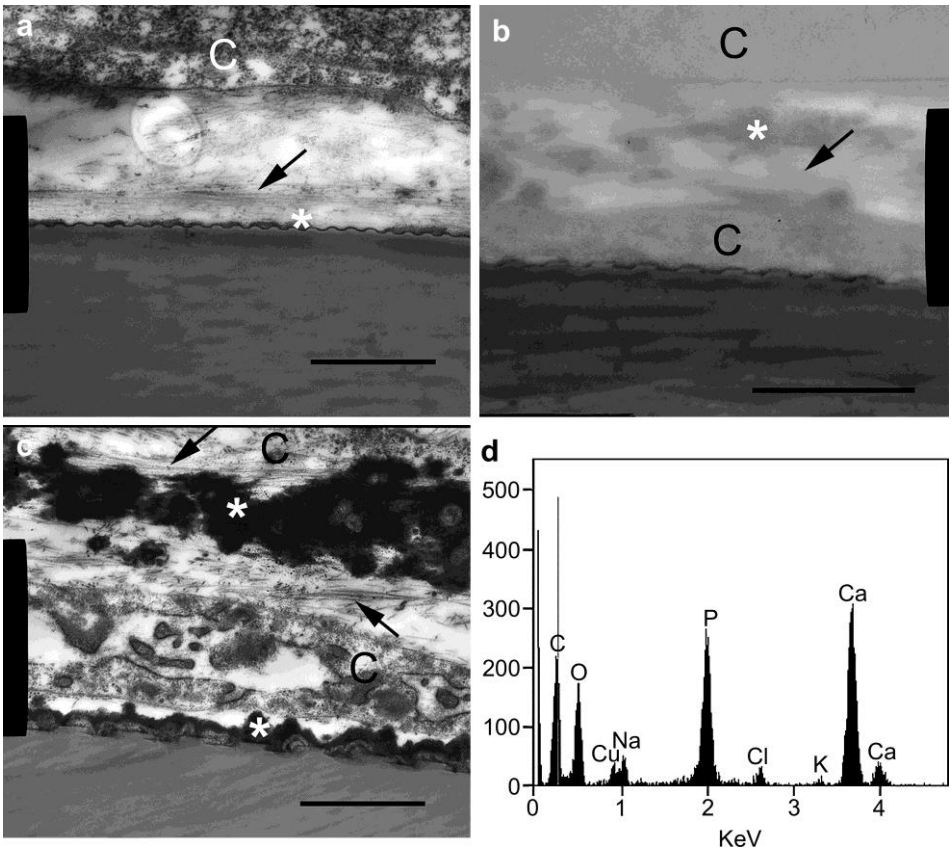

Figure 39. TEM images of osteoblast-like cells cultured for 12 (a, b) or 16 days (c) on grooved substrates with groove widths of respectively a. 75 nm (33 nm depth), b. 150 nm (49 nm depth) and c. 300 nm (122 nm depth). An electron dense area is formed in the interface between cells and substrate (asterisks in (a) and (c)). In the intercellular regions a mineralized ECM is formed by the presence of CaP (arrowheads) and collagen-I (arrows). In b. is shown that osteoblast-like cell bodies descend into 150 nm wide grooves. (d). Elemental analysis in the interface (asterisks in (a), (c)) shows that the electron dense area is indeed mineralized ECM, i.e. rich in calcium and phosphate (phosphor). C: Cell body. Scale bars represent 1 μm.

Further SEM analysis demonstrated that the CaP was deposited in an aligned mode after 8 days of culture (Figure 40). Strikingly, whereas osteoblasts did not

align to a groove width below 75 nm (and 33 nm depth), CaP deposition aligned even down to a groove width of 50 nm (and 17 nm depth) (Figure 40).

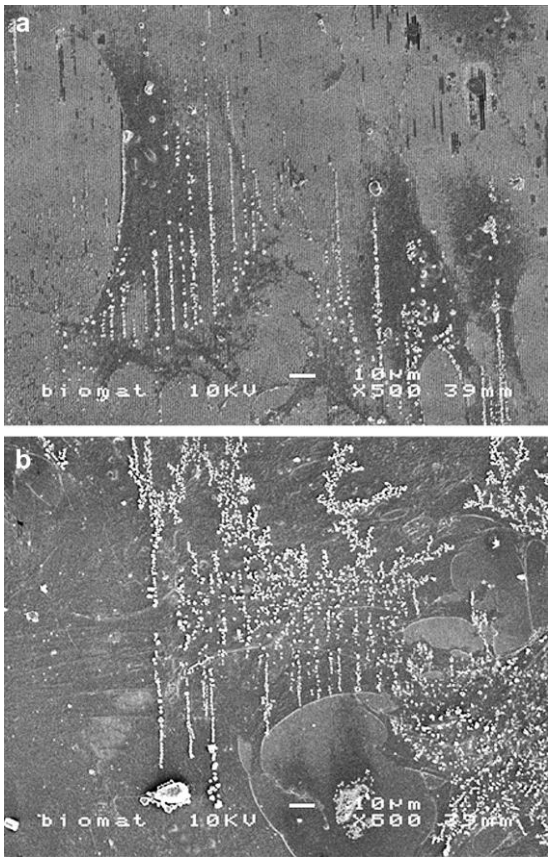

Figure 40. SEM images of osteoblast-like cells cultured for 8 days on grooved substrates. Osteoblast-like cells on a groove width of (a) 500 nm (153 nm) deposited CaP in an aligned fashion at the interface between cells and the substrate. Aligned CaP deposition at the interface was also observed at a groove width of (b) 50 nm (17 nm depth).

6.3.5. Real-time quantitative PCR analysis

The genes studied in the real-time quantitative (Q)PCR were coding for the four bone differentiation markers, (i.e. alkaline phosphatase (ALP), osteocalcin (OCN), bone sialoprotein (BSP) and the Cbfa1/Runx2 transcription factor (Cbfa1)), the major ECM protein collagen type-1 (Col-I) as well as the α-1 and

β-1 chains of the integrins, which are responsible for cell-substrate adhesion of cells. Relative gene expression was normalized to the household β-actin gene expression.

The expression of the tested genes was measured relative to smooth controls at three different time points (t = 1, 3 and 6 days) on three different groove pitches (p = 1000 nm, 3000 nm and 150 nm) for cells obtained from three different rats is shown in Table S1. The results demonstrated large differences in response to grooved relative to smooth substrates between the individual rats. Statistical analysis confirmed these differences (two-way Anova, $p < 0.05$, except for integrin-1β). However, data also demonstrated a clear pattern favoring the grooved substrates (Figure 41). In order to confirm this pattern, a ranking analysis was performed on the expression of the osteoblast specific markers (ALP, OCN, BSP, Col-I and Cbfa1) between the four surfaces at three time points (Figure 41). The analysis confirmed that expression of osteoblast-specific genes at day three and day six were increased on the grooved substrates compared to the smooth control (Friedman-test, $p < 0.05$). Moreover, the analysis indicated that a 500 nm groove width (158 nm depth) was more inductive for osteoblast differentiation than 150 and 75 nm widths (49 nm and 33 nm) respectively.

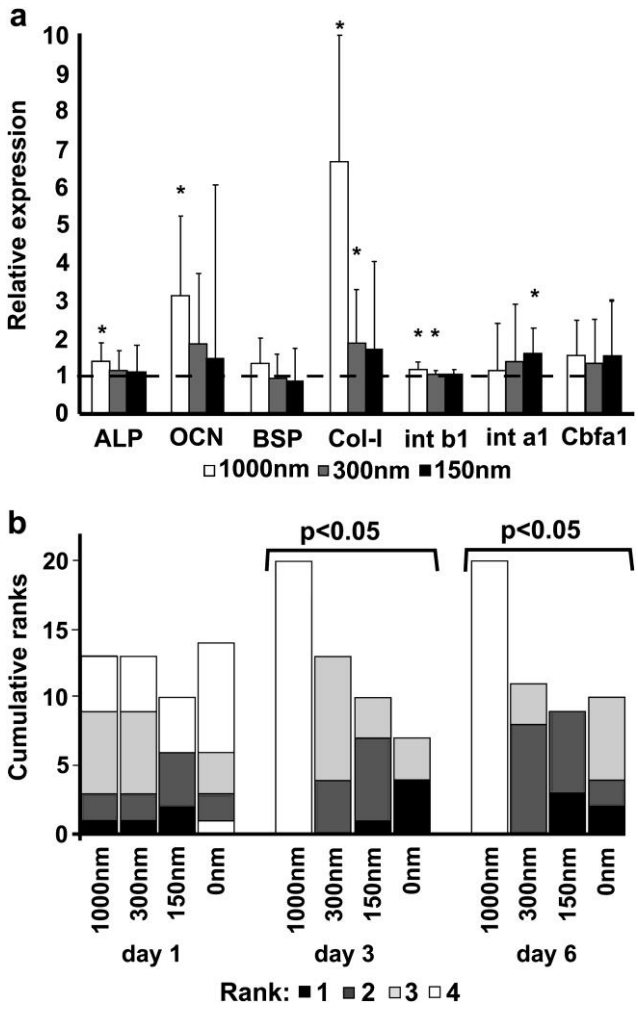

Figure 41. Influence of surface topography on gene expression. (a) Effects of the groove dimensions on gene expression of ALP, OCN, BSP, Col-I, Cbfa1 and the Int α-1 and β-1 by osteoblast-like cells relative to the smooth substrate. Data are expressed as $2^{-\Delta\Delta Ct}$ and range, n = 3. Values were normalized to β-actin and relative to smooth substrates. Asterisks: significant difference ($p < 0.05$). (b) Cumulative ranking of osteoblast-specific genes (ALP, OCN, BSP, Col-I and Cbfa1) expressed at three time points (day 1, 3 and 6). The difference in expression of each gene between the four substrates was ranked 1 (lowest expression) to 4 (highest expression) for each time point. The column heights represent the osteoblast-specific gene expression relative to the other groove dimensions.

6.4. Discussion

The aim of this study was to understand the morphological and differentiation response of osteoblasts to nanogrooved substrates. In order to achieve this, osteoblast response to these grooves was first assessed by performing an alignment analysis. The current study shows that osteoblasts are responsive to grooves with a nanoscale in all dimensions (groove and ridge width and depth). Zhu et al. [21] and more recently, Yang et al. [20] reported that bone cells aligned to nanogrooves down to respectively 150 nm width and 70 nm in depth or 90 nm width and 300 nm in depth. However, in both studies the actual groove spacing or depth were sub-micrometer and thus not very representative of the natural bone ECM [6]. In the current study, grooved substrates were used which in all dimensions were nanometric, including substrates in the range of natural bone ECM (75 nm groove width and 33 nm depth), to determine the response of osteoblasts in terms of alignment and morphology. Osteoblast response to nanopatterns was first screened using the biochip. From the results of this study, interesting groove dimensions were determined and nanogrooved substrates with a large area were created using laser interference lithography (LIL) and subsequent reactive ion etching (RIE). The major advantage of LIL over other techniques like electron beam lithography and ion beam lithography is the high patterning speed and significantly greater area [29,34]. This step is necessary as only upscaling of production techniques will enable the production of actual orthopedic and dental implants, and later *in vivo* validation of the current experimental results.

The results from investigations on the cell and cell-substrate interface demonstrate that osteoblast-like cells align to grooves approximating the natural extracellular bone matrix. In this context, focal adhesions are important for the specific recognition and response to the patterns as already described for micrometer ridges [35]. Focal adhesions are associated with the tips of actin filaments, serve to adhere the cell to the ECM proteins and are able to sense the surrounding of the cell [36]. As early as 1979, Ohara and Buck [37] hypothesized

that cells cannot align to surface features if focal adhesions cannot sense grooves with an excessive pitch (which is the sum of groove width and ridge width). The results presented in the current study demonstrated that both focal adhesion and cellular alignment decreased similarly with a decreasing groove pitch. Corroborating with the Ohara and Buck theory, these findings implicate that cells cannot align to grooves with a too small pitch because the patterns are not recognized by their focal adhesions.

Scanning and transmission EM studies demonstrated that the ECM mineral CaP is deposited in between the grooves by osteoblasts in an aligned fashion. This finding corroborates with the *in vivo* situation, where hydroxyapatite crystals deposited by osteoblasts are embedded in the spaces between highly organized collagen-I fibrils of similar dimensions as the grooves [6]. Possibly the osteoblasts recognize the nanogrooved substrate as a natural ECM environment and respond accordingly by the production of an organized ECM. Accordingly, a standardized nano-structured implant surface topography can be important for the formation of an organized bone ECM with high strength starting at the interface between the implant surface and bone tissue. *In vivo* studies are needed to validate whether indeed such an organized extracellular bone matrix is formed.

Alternatively, nanogrooved substrates can serve as a model system *in vitro* for obtaining a better fundamental insight into the initial osteoblasts response to the natural ECM. Recently, Pouget et al. [4] demonstrated that calcium carbonate crystals with a critical size of 70 nm are formed under the control of a negatively charged template. In accordance with this study, nanogrooves might serve as a template (nucleation points) to study structured calcium phosphate mineralization. TEM observations in the current study demonstrated that the amount of CaP deposited by the osteoblasts in between the grooves is increasing. However, the nucleation state of these CaP particles at these and later time points still has to be determined.

Further, the results demonstrated that osteoblast gene expression was highly influenced by individual rat differences. Several studies already demonstrated the advantageous influence of aspecific surface nano-roughness on osteoblast-like gene expression [38-41]. The rank analysis on the gene expression confirmed that a statistically significant upregulation also exists for the ordered nanotextures. Grooved surfaces, and in particular 500 nm wide grooves, are advantageous for osteoblast differentiation. Ponader et al. [39] and Yang et al. [41] demonstrated that gene expression on rough substrates relative to polished controls decreased from day three to seven during incubation. In agreement with these studies, the nanogrooved substrates seem to be specifically effective in the very first days of osteoblast-specific gene expression, which suggests that nanotextures can steer initial osteoblast differentiation.

6.5. Conclusions

In summary, this study proved by using several microscopic techniques and single cell Q-PCR that nanogrooves have a profound influence on osteoblast behavior. Osteoblasts are responsive to nanopatterns down to 75 nm in width and 33 nm in depth. Nanotexture-driven mineral deposition is induced and responsive to even smaller nanopatterns of 50 nm in width and 17 nm in depth. In addition, gene expression of osteoblast specific markers (ALP, OCN, BSP, Col-I and Cbfa1) is upregulated by nanogrooves. The results indicate that nanogrooves can be a very promising tool to direct the bone response at the interface between an implant and the bone tissue, which can benefit the installation of implants in compromised patients.

Acknowledgements

We thank Dr. E.M. Bronkhorst for statistical analyses. Scanning electron microscopy, transmission electron microscopy and confocal laser scanning microscopy were performed at the Microscope Imaging Centre (MIC) of the Nijmegen Centre for Molecular Life Sciences (NCMLS).

Appendix

Table S1. Effects of groove pitch (p) and time (t) on relative gene expression of alkaline phosphatase (ALP), osteocalcin (OCN), bone sialoprotein (BSP), collagen type-I, transcription factor Cbfa1 and the integrins α-1 and β-1 by osteoblast-like cells. For the study, osteoblasts derived from three rats were used (r1-3). Data are expressed as $2^{-\Delta\Delta Ct}$ and corresponding range, n = 3. Values were normalized to β-actin and relative to smooth substrates. Significantly different samples are marked in bold and boxes are made grey ($p < 0.05$).

r/t/p	ALP	OCN	BSP	Cbfa1	Col-I	int b-1	int a-1
r1/d1/1000 nm	0,90 (0,40-2,02)	0,73 (0,35-1,54)	0,95 (0,33-2,78)	1,48 (0,62-3,56)	3,11 (0,25-2,78)	1,02 (0,33-3,14)	1,35 (0,80-2,26)
r1/d1/1000 nm	0,66 (0,32-1,35)	0,58 (0,24-1,39)	0,51 (0,24-1,10)	1,45 (0,74-2,84)	1,58 (0,58-1,10)	0,70 (0,22-2,23)	0,84 (0,27-2,60)
r1/d1/300n m	0,74 (0,69-0,79)	0,87 (0,38-1,96)	0,56 (0,10-3,31)	1,32 (0,34-5,11)	1,05 (0,10-10,87)	0,93 (0,31-2,76)	1,98 (0,61-6,44)
r1/d3/1000 nm	1,42 (0,71-2,86)	2,06 (0,24-17,40)	1,57 (0,43-5,76)	1,10 (0,11-11,28)	79,06 (62,31-95,21)	1,41 (0,65-3,06)	2,77
r1/d3/300n m	1,41 (1,08-1,86)	1,34 (0,45-4,02)	1,12 (0,60-2,10)	1,96 (1,14-3,36)	18,05 (7,91-41,22)	1,00 (0,85-1,19)	2,27 (0,74-7,00)
r1/d3/150n m	1,28 (0,58-2,81)	2,07 (0,03-68,40)	0,85 (0,63-1,14)	1,03	24,44 (0,84-53,23)	1,00 (0,82-1,22)	1,56
r1/d6/1000 nm	0,95 (0,81-1,11)	0,77 (0,26-2,24)	0,86 (0,33-2,21)	0,150 (0,61-0,92)	1,33 (0,88-2,00)	0,77 (0,65-0,91)	0,53 (0,29-0,99)
r1/d6/300n m	0,74 (0,41-1,30)	0,34 (0,03-3,85)	0,49 (0,29-0,81)	0,35 (0,22-0,58)	0,78 (0,30-2,03)	0,82 (0,57-1,17)	0,52 (0,13-2,09)
r1/d6/150n m	1,03 (0,65-2,00)	0,28 (0,03-2,64)	0,59 (0,09-3,80)	0,49 (0,15-1,60)	0,53 (0,16-1,74)	0,97 (0,43-2,20)	0,66 (0,51-0,86)
r2/d1/1000 nm	0,49 (0,37-0,63)	0,37 (0,19-0,150)	0,48 (0,18-1,28)	0,42 (0,17-1,03)	0,98 (0,64-1,50)	1,06 (0,48-2,35)	1,33 (0,06-29,45)
r2/d1/300n m	0,39 (0,14-1,09)	0,31	0,29 (0,18-0,48)	1,14 (0,14-9,60)	0,36 (0,17-0,150)	0,90 (0,89-0,91)	2,00 (0,10-38,52)
r2/d1/150n m	0,16 (0,09-0,27)	1,34	0,41 (0,31-0,54)	n/a	1,65 (0,29-9,28)	0,60 (0,39-0,92)	0,98 (0,04-22,21)
r2/d3/1000 nm	0,50 (0,41-0,61)	1,15 (0,26-11,56)	0,26 (0,13-0,54)	1,03	2,99 (0,20-47,3)	0,60 (0,44-0,83)	3,06 (0,25-36,88)
r2/d3/300n m	0,55 (0,26-1,18)	1,11 (0,19-6,58)	0,37 (0,13-1,05)	1,36 (0,17-10,74)	0,36 (0,08-1,58)	0,74 (0,45-1,23)	4,63 (2,66-8,08)
r2/d3/150n m	0,20(0,14-0,28)	0,07 (0,00-2,47)	0,10 (0,08-0,13)	0,31 (0,22-0,44)	0,26 (0,09-0,74)	0,65 (0,33-1,28)	3,40 (2,35-4,92)
r2/d6/1000 nm	0,74(0,52-1,05)	0,85 (0,23-3,08)	0,97 (0,54-1,74)	0,65 (0,32-1,31)	1,08 (0,34-3,47)	0,68 (0,22-2,15)	0,65 (0,24-1,72)
r2/d6/300n m	0,59 (0,20-1,76)	0,10 (0,03-0,40)	0,84 (0,45-1,58)	0,150 (0,55-1,03)	0,49 (0,33-0,73)	1,44 (0,99-2,10)	2,03 (2,03-2,50)
r2/d6/150n m	0,92 (0,51-1,68)	0,41 (0,26-0,66)	1,38 (0,83-2,32)	0,80 (0,53-1,20)	0,68 (0,46-0,99)	1,15 (0,41-3,25)	0,95 (0,43-2,12)

r3/d1/1000 nm	0,86 (0,47-1,59)	0,73 (0,28-1,90)	0,87 (0,65-1,16)	4,04	1,58 (0,77-3,26)	0,93 (0,51-1,71)	0,84 (0,24-2,95)
r3/d1/300n m	1,80 (0,76-4,24)	2,58 (0,150-8,84)	0,91 (0,57-1,44)	1,93	4,60 (0,42-48,18)	0,87 (0,47-1,61)	1,16 (0,17-7,98)
r3/d1/150n m	2,00 (0,73-5,45)	1,96 (1,42-2,71)	1,23 (0,95-1,60)	n/a	0,80 (0,32-2,01)	0,98 (0,67-1,44)	0,69 (0,17-2,77)
r3/d3/1000 nm	3,62 (1,28-10,22)	5,88 (2,76-12,50)	5,22 (3,02-9,00)	2,82 (1,59-4,99)	3,25 (1,13-9,35)	0,73(0,38-1,39)	0,3 (0,06-1,78)
r3/d3/300n m	1,95 (0,45-8,51)	3,01 (0,25-36,15)	1,93 (0,25-15,01)	1,08 (0,25-4,72)	2,38 (0,54-10,45)	0,63 (0,45-0,87)	0,28 (0,02-5,14)
r3/d3/150n m	4,44 (2,35-8,39)	6,31 (1,48-26,90)	7,18 (3,19-16,17)	5,29 (3,30-8,48)	2,08 (0,28-15,45)	0,89 (0,35-2,24)	0,76 (0,18-3,29)
r3/d6/1000 nm	2,62 (1,19-5,77)	1,81 (0,53-6,16)	2,31 (0,93-5,70)	1,93 (0,85-4,39)	6,94 (2,29-21,01)	0,97 (0,58-1,61)	0,19 (0,05-0,76)
r3/d6/300n m	2,25 (1,89-2,68)	2,24 (1,74-2,90)	2,62 (1,69-4,06)	2,86 (1,95-4,20)	3,83 (2,24-6,53)	1,02 (0,59-1,78)	0,43 (0,26-0,70)
r3/d6/150n m	1,81 (0,64-5,14)	1,15 (0,23-5,72)	1,38 (0,41-4,72	1,45 (0,35-5,97)	1,64 (0,22-12,20)	1,63 (1,38-1,92)	0,52 (0,11-2,45)

1 Stevens, M. M. & George, J. H. Exploring and engineering the cell surface interface. *Science* **310**, 1135-1138 (2005).

2 Kasemo, B. & Gold, J. Implant surfaces and interface processes. *Advances in dental research* **13**, 8-20 (1999).

3 Curtis, A. & Wilkinson, C. Topographical control of cells. *Biomaterials* **18**, 1573-1583 (1997).

4 Pouget, E. M., Bomans, P. H. H., Goos, J. A. C. M., Frederik, P. M., De With, G. & Sommerdijk, N. A. J. M. The initial stages of template-controlled CaCO3 formation revealed by Cryo-TEM. *Science* **323**, 1455-1458 (2009).

5 Blokhuis, T. J., Termaat, M. F., Den Boer, F. C., Patka, P., Bakker, F. C. & Haarman, H. J. T. M. Properties of calcium phosphate ceramics in relation to their in vivo behavior. *Journal of Trauma - Injury, Infection and Critical Care* **48**, 179-186 (2000).

6 Weiner, S. & Wagner, H. D. The material bone: Structure-mechanical function relations. *Annual Review of Materials Science* **28**, 271-298 (1998).

7 Palin, E., Liu, H. & Webster, T. J. Mimicking the nanofeatures of bone increases bone-forming cell adhesion and proliferation. *Nanotechnology* **16**, 1828-1835 (2005).

8 Anderson, J. M. Host reactions to biomaterials and their evaluation. *Biomaterials Science: An Introduction to Materials in Medicine*, 165-173 (1996).

9 Dalby, M. J., McCloy, D., Robertson, M., Agheli, H., Sutherland, D., Affrossman, S. & Oreffo, R. O. C. Osteoprogenitor response to semi-ordered and random nanotopographies. *Biomaterials* **27**, 2980-2987 (2006).

10 Dalby, M. J., McCloy, D., Robertson, M., Wilkinson, C. D. W. & Oreffo, R. O. C. Osteoprogenitor response to defined topographies with nanoscale depths. *Biomaterials* **27**, 1306-1315 (2006).

11 De Oliveira, P. T., Zalzal, S. F., Beloti, M. M., Rosa, A. L. & Nanci, A. Enhancement of in vitro osteogenesis on titanium by chemically produced nanotopography. *Journal of Biomedical Materials Research - Part A* **80**, 554-564 (2007).

12 Tambasco De Oliveira, P. & Nanci, A. Nanotexturing of titanium-based surfaces upregulates expression of bone sialoprotein and osteopontin by cultured osteogenic cells. *Biomaterials* **25**, 403-413 (2004).

13 Hansen, J. C., Yul Lim, J., Xu, L. C., Siedlecki, C. A., Mauger, D. T. & Donahue, H. J. Effect of surface nanoscale topography on elastic modulus of individual osteoblastic cells as determined by atomic force microscopy. *Journal of Biomechanics* **40**, 2865-2871 (2007).

14 Lim, J. Y., Hansen, J. C., Siedlecki, C. A., Hengstebeck, R. W., Cheng, J., Winogard, N. & Donahue, H. J. Osteoblast adhesion on poly(L-lactic acid)/polystyrene demixed thin film blends: Effect of Nanotopography, surface chemistry, and wettability. *Biomacromolecules* **6**, 3319-3327 (2005).

15 Wan, Y., Wang, Y., Liu, Z., Qu, X., Han, B., Bei, J. & Wang, S. Adhesion and proliferation of OCT-1 osteoblast-like cells on micro- and nano-scale topography structured poly(L-lactide). *Biomaterials* **26**, 4453-4459 (2005).

16 Webster, T. J., Ergun, C., Doremus, R. H., Siegel, R. W. & Bizios, R. Enhanced functions of osteoblasts on nanophase ceramics. *Biomaterials* **21**, 1803-1810 (2000).

17 Webster, T. J. & Smith, T. A. Increased osteoblast function on PLGA composites containing nanophase titania. *Journal of Biomedical Materials Research - Part A* **74**, 677-686 (2005).

18 Zhu, X., Chen, J., Scheideler, L., Reichl, R. & Geis-Gerstorfer, J. Effects of topography and composition of titanium surface oxides on osteoblast responses. *Biomaterials* **25**, 4087-4103 (2004).

19 Lenhert, S., Meier, M. B., Meyer, U., Chi, L. & Wiesmann, H. P. Osteoblast alignment, elongation and migration on grooved polystyrene surfaces patterned by Langmuir-Blodgett lithography. *Biomaterials* **26**, 563-570 (2005).

20 Yang, J. Y., Ting, Y. C., Lai, J. Y., Liu, H. L., Fang, H. W. & Tsai, W. B. Quantitative analysis of osteoblast-like cells (MG63) morphology on nanogrooved substrata with various groove and ridge dimensions. *J Biomed Mater Res A* **90**, 629-640 (2008).

21 Zhu, B., Lu, Q., Yin, J., Hu, J. & Wang, Z. Alignment of osteoblast-like cells and cell-produced collagen matrix induced by nanogrooves. *Tissue Engineering* **11**, 825-834 (2005).

22 Matsuzaka, K., Walboomers, X. F., De Ruijter, J. E. & Jansen, J. A. The effect of poly-L-lactic acid with parallel surface micro on groove on osteoblast-like cells in vitro. *Biomaterials* **20**, 1293-1301 (1999).

23 Teixeira, A. I., Abrams, G. A., Bertics, P. J., Murphy, C. J. & Nealey, P. F. Epithelial contact guidance on well-defined micro- and nanostructured substrates. *Journal of Cell Science* **116**, 1881-1892 (2003).

24 Teixeira, A. I., McKie, G. A., Foley, J. D., Bertics, P. J., Nealey, P. F. & Murphy, C. J. The effect of environmental factors on the response of human corneal epithelial cells to nanoscale substrate topography. *Biomaterials* **27**, 3945-3954 (2006).

25 Loesberg, W. A., te Riet, J., van Delft, F. C. M. J. M., Schön, P., Figdor, C. G., Speller, S., van Loon, J. J. W. A., Walboomers, X. F. & Jansen, J. A. The threshold at which substrate nanogroove dimensions may influence fibroblast alignment and adhesion. *Biomaterials* **28**, 3944-3951 (2007).

26 van Delft, F. C. M. J. M., van den Heuvel, F. C., Loesberg, W. A., te Riet, J., Schön, P., Figdor, C. G., Speller, S., van Loon, J. J. W. A., Walboomers, X. F. & Jansen, J. A. Manufacturing substrate nano-grooves for studying cell alignment and adhesion. *Microelectronic Engineering* **85**, 1362-1366 (2008).

27 Van Delft, F. C. M. J. M., Weterings, J. P., Van Langen-Suurling, A. K. & Romijn, H. Hydrogen silsesquioxane/novolak bilayer resist for high aspect ratio

nanoscale electron-beam lithography. *Journal of Vacuum Science and Technology B: Microelectronics and Nanometer Structures* **18**, 3419-3423 (2000).

28 Walboomers, X. F., Croes, H. J. E., Ginsel, L. A. & Jansen, J. A. Growth behavior of fibroblasts on microgrooved polystyrene. *Biomaterials* **19**, 1861-1868 (1998).

29 Van Soest, F. J., Van Wolferen, H. A. G. M., Hoekstra, H. J. W. M., De Ridder, R. M., Wörhoff, K. & Lambeck, P. V. Laser interference lithography with highly accurate interferometric alignment. *Japanese Journal of Applied Physics, Part 1: Regular Papers and Short Notes and Review Papers* **44**, 6568-6570 (2005).

30 Luttge, R., Van Wolferen, H. A. G. M. & Abelmann, L. Laser interferometric nanolithography using a new positive chemical amplified resist. *Journal of Vacuum Science and Technology B: Microelectronics and Nanometer Structures* **25**, 2476-2480 (2007).

31 Maniatopoulos, C., Sodek, J. & Melcher, A. H. Bone formation in vitro by stromal cells obtained from bone marrow of young adult rats. *Cell and Tissue Research* **254**, 317-330 (1988).

32 Shieh, A. C. & Athanasiou, K. A. Dynamic compression of single cells. *Osteoarthritis and Cartilage* **15**, 328-334 (2007).

33 Livak, K. J. & Schmittgen, T. D. Analysis of relative gene expression data using real-time quantitative PCR and the 2-ΔΔCT method. *Methods* **25**, 402-408 (2001).

34 Curtis, A. S. G., Casey, B., Gallagher, J. O., Pasqui, D., Wood, M. A. & Wilkinson, C. D. W. Substratum nanotopography and the adhesion of biological cells. Are symmetry or regularity of nanotopography important? *Biophysical Chemistry* **94**, 275-283 (2001).

35 Den Braber, E. T., Jansen, H. V., De Boer, M. J., Croes, H. J. E., Elwenspoek, M., Ginsel, L. A. & Jansen, J. A. Scanning electron microscopic, transmission electron microscopic, and confocal laser scanning microscopic observation of fibroblasts cultured on microgrooved surfaces of bulk titanium substrata. *Journal of Biomedical Materials Research* **40**, 425-433 (1998).

36 Wozniak, M. A., Modzelewska, K., Kwong, L. & Keely, P. J. Focal adhesion regulation of cell behavior. *Biochimica et Biophysica Acta - Molecular Cell Research* **1692**, 103-119 (2004).

37 Ohara, P. T. & Buck, R. C. Contact guidance in vitro. A light, transmission, and scanning electron microscopic study. *Experimental Cell Research* **121**, 235-249 (1979).

38 Kubo, K., Att, W., Yamada, M., Ohmi, K., Tsukimura, N. & Suzuki, T. Microtopography of titanium suppresses osteoblastic differentiation but enhances chondroblastic differentiation of rat femoral periosteum-derived cells. *J Biomed Mater Res A* (2008).

39 Ponader, S., Vairaktaris, E., Heinl, P., Wilmowsky, C. V., Rottmair, A., Körner, C., Singer, R. F., Holst, S., Schlegel, K. A., Neukam, F. W. & Nkenke, E. Effects of

topographical surface modifications of electron beam melted Ti-6Al-4V titanium on human fetal osteoblasts. *Journal of Biomedical Materials Research - Part A* **84**, 1111-1119 (2008).

40 Tsai, S. W., Chen, C. C., Chen, P. L. & Hsu, F. Y. Influence of topography of nanofibrils of three-dimensional collagen gel beads on the phenotype, proliferation, and maturation of osteoblasts. *J Biomed Mater Res A* (2008).

41 Yang, X. f., Chen, Y., Yang, F., He, F. M. & Zhao, S. f. Enhanced initial adhesion of osteoblast-like cells on an anatase-structured titania surface formed by H_2O_2/HCl solution and heat treatment. *Dental Materials* **25**, 473-480 (2009).

7.

CONCLUSIONS AND OUTLOOKS

7.1. Conclusions: how far we have reached?

The main scope of the work conducted in this thesis was to design and manufacture large area nanostructured biomaterial surfaces. The secondary target of the work was exploration of the influence of the nanostructures on protein adsorption and cell behavior. The gained experience and results brought us to the following conclusions:

- Many different nanofabrication techniques are suitable for the delivery of *in vitro* and *in vivo* test surfaces. All the available techniques however focus mostly on planar surfaces, where real world biomaterials consist always of curved surfaces.
- In the interaction between a nanopatterned surface and albumin and fibronectin the quantity of adsorbed protein, is not proportional to available surface area for –OH terminated nanostructured silicon surfaces, whereas for flat non-nanostructured surfaces the trend between available surface area and amount of adsorbed protein is linear. For nanostructured surfaces modified with $–CH_3$ surface groups the trends surface area – quantity of adsorbed protein are linear with the available surface area emerging from the nanostructure. Collagen, both on SiO_2–OH surfaces and SiO_2–CH_3 terminated surfaces, does not follow the same trends. Moreover, in HRSEM and HIM observations distinct self-organization of collagen fibers was observed on the surface of nanogrooved substrates.
- Different cell lines respond in significantly distinct manner to different size surface nanofeatures. The first observation is that cells always align to the long axis of ridge-groove structure. Depending on the cell size the threshold below which cells do not align is located somewhere around 150 nm pitch. Together with alignment, significant changes in cells functioning were observed. The surface topography influences gene expression by osteoblasts, with significant up regulation of

Collagen type I primer. Finally, mineral phase deposition is induced and aligned by the nanopatterns.

- In studies, in which the influence of topographical stimuli is to be measured and quantified one has to make sure that the chosen technique of patterning delivers a consistent result at the nanoscale. In other words, meeting the requirements of biology asks for large area surfaces with scalable nanostructures and a high fidelity in control of critical dimensions on the scale of substrate, i.e. a large area of at least a few cm^2.

The last conclusive remark must be that, knowing how important the influence of surface topography and surface chemistry is, a person designing novel biomaterials has to take into account the synergistic effect of both on biomaterial surface – body interactions. Deciphering the cues that influence the cells *in vitro* and *in vivo* requires particular insight and characterization of physicochemistry of large-scale substrates.

7.2. Future scope: where can we go from here?

A number of fabrication techniques need further development to meet the requirements of industrial fabrication of nanopatterned biomaterial surfaces. Creating nanopatterns on bioimplants is limited when lithographic techniques are used since these techniques are meant to pattern ultra-flat planar surfaces commonly used in nanofabrication. With pattern generation methods presented in this work – Laser Interference Lithography, UV lithography or Nanoimprint lithography, due to fundamentals of their functioning only one method can promise pattern transfer on non-planar surfaces: Nanoimprint lithography. Recent developments in this technique facilitate imprints on surfaces with low curvature radius, and thus are promising for pattern transfer on real biomedical implants [1].

In the methods proposed here, after rough calculation of costs invested in materials, work and facilities the value of a single 5 mm titanium disc with a nanostructure on one side is estimated at ca. 200 euro. This is a high price from the mass scale production perspective. Minimization of costs can be achieved in large scale production but also with introduction of less complicated fabrication methods. The proposed route of LIL-NIL-RIE minimizes already the amount of involved fabrication steps.

We have presented that nano-grooved surfaces are indeed bioactive, inducing certain behaviors in *in vitro* models. Further development of nanostructured implants has to be followed with suitable *in vivo* research with well-defined materials, like the ones constituted in this work. The technology platform proposed in this work is not only limited to biomaterial surfaces. Replications like NIL and solvent casting might be utilized for replication of nanostructure into cell scaffolds where bioactivity can be used for delivering new surfaces for tissue engineering and regenerative medicine. The observed trend in biomaterial research is focusing on biomaterial surface driven interactions[2]. The so-called third generation biomaterials[3] can be indeed materials utilizing topographical modification to induce certain bioactivity in the body. The recent progress in the development of material surfaces stimulating cell gene activation[4] is an interesting and worth exploring. We have observed in our research that indeed the nanoridges with distinct size can stimulate up or down regulation of certain gene expression in cells. Further studies of this phenomenon should be addressed.

1 Ji, R., Hornung, M., Verschuuren, M. A., van de Laar, R., van Eekelen, J., Plachetka, U., Moeller, M. & Moormann, C. UV enhanced substrate conformal imprint lithography (UV-SCIL) technique for photonic crystals patterning in LED manufacturing. Microelectronic Engineering **87**, 11.134, (2009)

2 Leeuwenburgh, S. C. G., Jansen, J. A., Malda, J., Dhert, W. A., Rouwkema, J., van Blitterswijk, C. A., Kirkpatrick, C. J. & Williams, D. F. Trends in biomaterials research: An analysis of the scientific programme of the World Biomaterials Congress 2008. *Biomaterials* **29**, 3047-3052 (2008).

3 Hench, L. L. & Polak, J. M. Third-generation biomedical materials. *Science* **295**, 1014+1016-1017 (2002).

4 Hench, L. L. & Thompson, I. Twenty-first century challenges for biomaterials. *Journal of The Royal Society Interface* (2010).

Process 1. A. LIL delivered low aspect nanostructures in silicon (Positive resist)

Step	Process		Comment
1	Substrate selection: Silicon	Supplier: Okmetic ; Single side polished; Thickness 525 ± 25 µm; Orientation {100}; Diameter: 4 inch, ~100 mm; P-doped, resistivity 5-10 Ωcm^{-1}.	
2	Standard cleaning of silicon wafer	Equipment and consumables: HNO_3 100 % Selectipur : MERCK 100453; HNO_3 69 % VLSI : MERCK 116445; Process: Immerse in HNO_3 100 % 1st beaker, 5 min, RT, no agitation; Immerse in HNO_3 100 % 2nd beaker, 5 min, RT, no agitation; Quick dump rinse in DI <0.1µS; Immerse in HNO_3 69 %, 10 min, 95°C, no agitation; Quick dump rinse in DI <0.1µS; Spin dry 3000 rpm with nitrogen blow.	Clean semitool spin rinse dryer might be also used for final rinse and drying
3	Resist spin coating	Equipment and consumables: Bottom antireflective coating (BARC), DUV30-J6 (Brewer Science); Positive tone resist, PEK 500 (Sumitomo Chemical); Top antireflective coating (TARC), Aquatar AQ6 (AZ Electronic Materials); Flatbed post bake hot plates set at 90°C, 110°C and 205°C; Sister Semiconductor Opticoat (SSE ST22+) spin coater; Automatic pipette and 2.5 cm^3 tips; Process: BARC: Pipette 1.5 cm^3 BARC, spin 2000 RPM with closed cover for 45 s, post bake for 30 s at 90°C followed by 90 s at 205 °C; Resist: Pipette 1.5 cm^3 resist, spin 2000 RPM with open cover for 45 s, post bake for 90 s at 110°C; TARC: Pipette 1.5 cm^3 TARC, spin 2000 RPM with open cover for 45 s, no post bake.	Take care that the chuck and cover don't carry leftovers of previously used resists

4	Laser Interference Lithography	Equipment and consumables: 75% v/v OPD4262 in water (Fuji-film Electronic Materials); Flatbed hot plates set to 105°C; Fourth harmonic continuous-wave yttrium aluminum garnet laser MBD 266 system with self-constructed Lloyd's mirror interference setup, Newport optical table. Process: Intensity of the light measured in front of Lloyd's mirror I=55 mW cm^{-2}. Exposure angles and times: P= 1um, θ =7.64° t=20 s ; P=600 nm, θ =12.80° t=20.3 s; P=300 nm, θ =26.32° t=22.1 s; P=200 nm, θ =41.68° t=28 s; P=150 nm, θ =62.45° t=43 s; Post exposure bake (PEB): 90 s at 105°C; Development for 60 s.	
5	Reactive Ion Etching	Equipment and consumables: Plasmatherm 790 Reactive Ion Etcher (Unaxis). Process: Temperature 10°C for all steps; BARC etch through: Pressure 18 mTorr; O_2 flow: 8 sccm; Power 280 W ; Etch time: 18 s. Silicon Etch: Pressure 30 mtorr; SF_6 flow 30 sccm; O_2 5 sccm; Power 375 W; Times: P= 1um T = 54 s; P=600 nm T = 40 s; P=300 nm T = 21 s; P=200 nm T = 18 s; P=150 nm T = 14 s.	Beware of condensation on chilled-down vacuum chamber.
6	Resist strip	Equipment and consumables: Tepla 300E (PVA Tepla) barrel etcher 2.45 GHz. Process:	

		Oxygen flow 55 sscm; Pressure 1.3 mbarr; Power 500 W; Time 10 min.	

Process 1. B LIL delivered high aspect nanostructures in silicon for NIL lithography (Negative resist).

Step	Process		Comment
1	Substrate selection: Silicon	Supplier: Okmetic ; Single side polished; Thickness 525 ± 25 μm; Orientation {100}; Diameter: 4 inch, ~100 mm; P-doped, resistivity 5-10 Ω cm^{-1}.	
2	Standard cleaning of silicon wafer	Equipment and consumables: HNO_3 100 % Selectipur: MERCK 100453; HNO_3 69 % VLSI: MERCK 116445. Process: Immerse in HNO_3 100 % 1st beaker, 5 min, RT, no agitation; Immerse in HNO_3 100 % 2nd beaker, 5 min, RT, no agitation; Quick dump rinse in DI <0.1μS; Immerse in HNO_3 69 %, 10 min, 95°C, no agitation; Quick dump rinse in DI <0.1μS; Spin dry 3000 rpm with nitrogen blow.	Clean semitool spin rinse dryer might be also used for final rinse and drying
3	Resist spin coating	Equipment and consumables: Bottom antireflective coating (BARC), DUV30-J6 (Brewer Science); Negative tone resist MaN-2403 Microresist GmbH; Top antireflective coating (TARC), Aquatar AQ6 (AZ Electronic Materials); Flatbed post bake hot plates set at 90°C, 110°C and 180°C; Sister Semiconductor Opticoat (SSE ST22+) spin coater; Automatic pipette and 2.5 cm^3 tips; Process: BARC: Pipette 1.5 cm^3 BARC, spin 2000 RPM with closed cover for 45 s, post bake	Take care that the chuck and cover don't carry leftovers of previously used resists

		for 30 s at 90°C followed by 90 s at 180°C; Resist: Pipette 1.5 cm^3 resist, spin 2000 RPM with closed cover for 45 s, post bake for 90 s at 110°C; TARC: Pipette 1.5 cm^3 TARC, spin 2000 RPM with closed cover for 45 s, no post bake.	
4	Laser Interference Lithography	Equipment and consumables: 75 % v/v OPD4262 in water (Fuji-film Electronic Materials); Fourth harmonic continuous-wave yttrium aluminum garnet laser MBD 266 system with self-constructed Lloyd's mirror interference setup, Newport optical table. Process: For different pitch size different time and Intensity were used; Intensity of the light measured in front of Lloyd's mirror I=175 mW cm^{-2}; Exposure time dependent on desired R:G ratio and Pitch size of the structure (as presented in chapter 2 of the thesis); Development for 45 s ; No post bake.	
5	Reactive Ion Etching	Equipment and consumables: Plasmatherm 790 Reactive Ion Etcher (Unaxis). Process: BARC etch through : Temperature 10°C; Pressure 18 mTorr; O_2 flow: 8 sccm; Power 280 W ; Etch time : 18 s.	Beware of condensation on chilled-down vacuum chamber.
6	Deep Reactive Ion Etching	Equipment and consumables: Alcatel Adixen AMS 100SE Inductively Coupled Reactive Ion Etching. Process: Temperature -120°C, helium back cooling; Pressure 12 Pa; Etch gas SF_6 flow 50 sccm; Deposition gas C_4F_8 flow 40 sccm; Power 500 W ICP, 50 W CCP; Etch/deposition alternating process (BOSCH type);	The etch time defines depth of groove in the structure, maximum AR ~20.

		Etch time: depends on desired structure depth, etch rate ~1 μm min^{-1}.	
7	Reactive Ion Etching for sidewall smoothening	Equipment and consumables: Plasmatherm 790 Reactive Ion Etcher (Unaxis). Process: BARC etch through : Temperature 15°C; Pressure 30 mTorr; SF_6 flow 30 sccm; O_2 flow: 5 sccm; Power 375 W ; Times: P= 1000 nm T = 60 s; P=600 nm T = 40 s; P=300 nm T = 22 s; P=200 nm T = 20 s; P=150 nm T = 17 s.	This step smoothens the sidewalls of nanostructure after BOSCH process
8	Resist strip	Equipment and consumables: Tepla 300E barrel etcher 2.45 GHz. Process: Oxygen flow 55 sscm; Pressure 1.3 mbarr; Power 500 W; Time 10 min.	
9	FDTS anti-sticking layer deposition	Equipment and consumables: Furnace set at 80°C, vacuum pump, desiccator, (1H,1H,2H,2H)-perfluorodecyltrichlorosilane (FDTS, Sigma Aldrich). Process: Wafers carrying nanostructure are pre baked for 3 min in 80°C and transferred to desiccator, 1 cm^3 of liquid FDTS is placed in the same desiccator in reservoir and system is vacuumed and left for 1 h on vacuum.	The best results are obtained if wafers are still hot. FDTS can be placed in small vial next to the wafers.

Process 2. UV-lithography defined molds for tape casting

Step	Process		Comment
1	Substrate selection: Silicon	Supplier: Okmetic ; Single side polished; Thickness 525 ± 25 μm;	

		Orientation {100}; Diameter: 4 inch, ~100 mm; P-doped, resistivity 5-10 Ω cm^{-1}.	
2	Standard cleaning of silicon wafer	Equipment and consumables: HNO_3 100 % Selectipur: MERCK 100453; HNO_3 69 % VLSI: MERCK 116445; Process: Immerse in HNO_3 100 % 1st beaker, 5 min, RT, no agitation; Immerse in HNO_3 100 % 2nd beaker, 5 min, RT, no agitation; Quick dump rinse in DI <0.1µS; Immerse in HNO_3 69 %, 10 min, 95°C, no agitation; Quick dump rinse in DI <0.1µS; Spin dry 3000 rpm with nitrogen blow.	Clean semitool spin rinse dryer might be also used for final rinse and drying
3	Resist spin coating	Equipment and consumables: Suss Micro Tech Spinner (Delta 20); Hotplate 95°C; Olin 907-17 Resist; Spin speed 4000 RPM; Spinning time 20 s; Prebake 60 s.	
4	UV lithography	Equipment and consumables: EVG 20 (Electronic Vision Group) mask aligner; OPD4262 developer(Fuji-film Electronic Materials); Hotplate 120°C; Chromium on glass mask. Process: Hg lamp 12 mW cm^{-2}; Exposure time 6 s; Development for 45 s; Quick dump rinse <0.1µS; Post exposure bake for 60 s at 120°C.	Development split in two steps 30 s and 15 s in two separate beakers
5	Deep Reactive Ion Etching	Equipment and consumables: Alcatel Adixen AMS 100SE Inductively Coupled Reactive Ion Etching. Process: Temperature 10°C, helium back cooling; APC 15 %; Etch gas SF_6 flow 400 sccm;	

		Deposition gas C_4F_8 flow 10 sccm; Power 2500 W ICP, 10 W CCP; Etch/deposition alternating process (BOSCH type); Etch time 2 min.	
6	Resist strip	Equipment and consumables: Tepla 300E barrel etcher 2.45 GHz. Process: Oxygen flow 55 sscm; Pressure 1.3 mbarr; Power 500 W; Time 10 min.	
7	Plasma enhanced fluorocarbon deposition	Equipment and consumables: Alcatel Adixen AMS 100SE Inductively Coupled Reactive Ion Etching. Process: Temperature 20°C, helium back cooling; APC 50 %; Deposition gas C_4F_8 flow 300 sccm ; Power 200 W ICP, 80 W CCP; Deposition time 1 min.	Deposition of fluorocarbon was validated by water contact angle measurement.
8	Metal sputtering	Equipment and consumables: Plasma sputtering equipment, Sputterke TCO. Process: Argon flow 80 sccm; Power 200 W; Sputter pressure 6.6 e^{-3} mbarr; Ti target for presputtering as adhesive layer (10 s), subsequently gold target for gold deposition (2 min).	

Process 3. NIL lithography and titanium reactive ion etching

Step	Process		Comment
1	Substrate selection: Titanium	Supplier: Bimotech metals ASTM B265 Grade 2 Titanium discs; Thickness 800 ± 50 µm; Polycrystalline material ; Diameter: 4 inch, ~100 mm; Not polished, unannealed titanium.	
2	Chemical -	Equipment and consumables:	Prevent drying of

	mechanical polishing	Mecapol E460 CMP; Rodel CR IC1000-A2 polishing pad; Cabot SemiSperse 25, 1:1 H_2O diluted slurry; Cleaning station, Micro Automation Inc. 2006. Process: Pad rotation speed 55 rpm; head rotation speed 55 rpm; Force on back of wafer 1.3 kN cm^{-2}; Time: 15 min; Pad temperature ~35 °C. After polishing transfer wafer to cleaning station and run 2 standard cleaning processes.	polishing slurry on wafer, keep wafers in DI water after polishing.
3	Resist spin coating	Equipment and consumables: Sister Semiconductor Opticoat (SSE ST22+) spin coater; Hotplate 140 °C; MR-I 8020 thermal imprint resist (Microresist, Germany). Process: Approx. 1 cm^3 resist per wafer; spin acceleration 500 RPM/s ; spin time 45 s; spin velocities: P=1000 nm 1500 RPM; P=600 nm 2000 RPM; P=300 nm 3000 RPM; P=200 nm 3000 RPM;	Take care that the chuck and cover don't carry leftovers of previously used resists.
4	Thermal Nanoimprint Lithography	Equipment and consumables: Eitre 6 Nanoimprint Tool (Obducat); Silicon masters prepared in process 1 B. Process: temperature 165 °C; time 120 s; pressure 40 bar; release temp 100 °C.	Separate wafers immediately after removing from nanoimprint tool.
5	Chlorine plasma reactive ion etching	Equipment and consumables: Oxford 100 ICP 180 dry etching tool (Oxford Instruments). Process: Cl_2 flow 33 sccm; CF_4 flow 2.3 sccm;	Before etching run 3 min process on dummy wafer to condition the chamber. Observe plasma

		Ar flow 50 sccm; O_2 flow 2 sccm; ICP power 1200 W; CCP power of 100 W; ACP 100 %; Temperature 40°C, helium back cooling.	during etching – flickering might occur causing faulty run.
6	Resist strip	Equipment and consumables: Tepla 300E barrel etcher 2.45 GHz. Process: Oxygen flow 55 sscm; Pressure 1.3 mbarr; Power 500 W; Time 10 min.	

Process 4. LIL defined silicon samples for protein affinity studies fabrication

Step	Process		Comment
1	Substrate selection: Silicon	Supplier: Okmetic; Double side polished; Thickness ± 500 µm; Orientation {100}; Diameter: 4 inch, ~100 mm; P-doped, resistivity 5-10 Ω cm^{-1};	
2	Standard cleaning of silicon wafer	Equipment and consumables: HNO_3 100 % Selectipur: MERCK 100453; HNO_3 69 % VLSI: MERCK 116445. Process: Immerse in HNO_3 100 % 1st beaker, 5 min, RT, no agitation; Immerse in HNO_3 100 % 2nd beaker, 5 min, RT, no agitation; Quick dump rinse in DI <0.1µS; Immerse in HNO_3 69 %, 10 min, 95°C, no agitation; Quick dump rinse in DI <0.1µS; Spin dry 3000 rpm with nitrogen blow.	Clean semitool spin rinse dryer might be also used for final rinse and drying
3	Resist spin coating	Equipment and consumables: Bottom antireflective coating (BARC), DUV30-J6 (Brewer Science); Negative tone resist MaN-2403 Microresist GmbH; Top antireflective coating (TARC), Aquatar	Take care that the chuck and cover don't carry leftovers of previously used resists

		AQ6 (AZ Electronic Materials); Flatbed post bake hot plates set at 90°C, 110°C and 180°C; Sister Semiconductor Opticoat (SSE ST22+) spin coater; Automatic pipette and 2.5 cm^3 tips; Process: BARC: Pipette 1.5 cm^3 BARC, spin 2000 RPM with closed cover for 45 s, post bake for 30 s at 90°C followed by 90 s at 180°C; Resist: Pipette 1.5 cm^3 resist, spin 2000 RPM with closed cover for 45 s, post bake for 90 s at 110°C; TARC: Pipette 1.5 cm^3 TARC, spin 2000 RPM with closed cover for 45 s, no post bake. For P=150 nm BARC spin at 3000 RPM and resist spin at 2500 RPM gives best result.	
4	Laser Interference Lithography	Equipment and consumables: 75 % v/v OPD4262 in water (Fuji-film Electronic Materials); Fourth harmonic continuous-wave yttrium aluminum garnet laser MBD 266 system with self-constructed Lloyd's mirror interference setup, Newport optical table. Process: For different pitch size different time and intensity were used depending on final R:G ratio and pitch size (see figure 7 chapter 2); Intensity of the light measured in front of Lloyd's mirror I=180 mW cm^{-2}; Development for 45 s for P=200 nm – 1000 nm; 35 s for P<200 nm; No post bake.	
5	Reactive Ion Etching	Equipment and consumables: Plasmatherm 790 Reactive Ion Etcher (Unaxis) Process: Temperature 15°C; Pressure 30 mTorr; SF_6 flow 30 sccm; O_2 flow: 5 sccm; Power 375 W; For all pitch size etch time 12 s.	Beware of condensation on chilled-down vacuum chamber.
6	Deep Reactive	Equipment and consumables:	The etch time

	Ion Etching	Alcatel Adixen AMS 100SE Inductively Coupled Reactive Ion Etching. Process: Temperature -120°C, helium back cooling; Pressure 12 Pa; Etch gas SF_6 flow 50 sccm; Deposition gas C_4F_8 flow 40 sccm; Power 500 W ICP, 50 W CCP; Etch/deposition alternating process (BOSCH type); Etch time: P=600 nm T=70.2 s; P=300 nm T=46.8 s; P=200 nm T= 20.6 s; P=150 nm T= 19.5 s.	defines depth of groove in the structure
7	Reactive Ion Etching for sidewall smoothening	Equipment and consumables: Plasmatherm 790 Reactive Ion Etcher (Unaxis). Process: Temperature 15°C. BARC etch through : Pressure 30 mTorr; SF_6 flow 30 sccm; O_2 flow: 5 sccm; Power 375 W ; Etch time: P=600 nm T=54 s; P=300 nm T=33 s; P=200 nm T= 19 s; P=150 nm T= 12 s.	This step smoothens the sidewalls of nanostructure after BOSCH process
8	Resist strip	Equipment and consumables: Tepla 300E barrel etcher 2.45 GHz. Process: Oxygen flow 55 sscm; Pressure 1.3 mbarr; Power 500 W; Time 10 min.	
9	Dry Oxidation	Equipment and consumables: Multipurpose furnace. Process: Oxygen flow 15 sccm; Temperature 860°C; Time 1 h	

		Ramping: no.	

Summary

The hypothesis of the research in this thesis is that nanofeatures on the surface of an implant enhance biofunctionality. This thesis introduces several approaches to micro and nanopatterning which are well-known in the MEMS and NEMS fields in order to deliver dimensionally scalable nanostructures suited for the investigation of nanofeature – bio moiety interactions. Micro– and nanoengineering of materials like ceramics, polymers, silicon and titanium is presented here with the goal to obtain surfaces with enhanced biocompatibility and potential bioactivity. The work conducted was part of the STW project NanoSurf, in which extensive studies on interactions between the nanofabricated surfaces of materials for biomedical applications and bio moieties in *in vitro* and *in vivo* experiments were conducted.

In the first part of the work, micro structuring of ceramic materials utilizing tape casting and micromolding techniques was found to be a useful method of delivering micropatterned bioceramics. Further, a novel nanofabrication method for ridges and grooves on biomaterials delivered highly ordered nanoscale patterns, scalable in all spatial dimensions from a few tens of nm's up to several micrometers. To obtain the nanofeatures on biomaterial surfaces, first Laser Interference Lithography was employed to define patterns in resist on silicon. Next, the structures were transferred into silicon with multiple reactive ion etching (RIE) steps. Finally, the surface nanofeatures were reproduced into polymers and used for *in vitro* studies or copied by means of Nanoimprint lithography (NIL) onto biomedical grade titanium and etched with optimized chlorinated plasma reactive ion etching (RIE) process. Nanogratings with smallest ridge and groove sizes in the order of 75 nm in silicon and 150 nm in biomedical grade titanium were produced. The parallel nanopatterning methods presented here are fast, highly reproducible and capable of delivering large uniformly patterned cell seeding areas of up to 5 cm^2. By the very nature of

designing a fabrication process, deviations of targeted feature dimensions on the surface exist. We characterize the deviations and present strategies to optimize the dimensions for the variety of biological assays required to proof the nanostructure-cell interaction hypothesis.

In the biological research, first the nanofabricated surfaces were explored in interaction with ECM proteins. It was found that the protein adsorption in presence of regular surface nanostructure in most cass is a direct function of available surface area, while surface chemistry plays a large role in the interaction. Finally, the nanostructures were replicated in polystyrene slabs and a series of experiment with osteoblasts were performed, showing characteristic reactions of cells on distinct surface features i.e. upregulation of gene expression, alignment of the cell body and focal adhesions to the nanostructure.

As a conclusion, it can be said that the set of optimized fabrication routes presented here provides well-defined modified biomaterial surfaces very suitable for parametric studies and further statistical research in implantology.

Samenvatting

De hoofdstelling in dit proefschrift is dat nanostructuren op het oppervlak van een implantaat de biofunctionaliteit ervan verbeteren. Deze thesis introduceert een aantal benaderingen die gebruik maken van micro- en nano-patronneringstechnieken die reeds bekend zijn uit de MEMS en NEMS vakgebieden. Hier worden ze gebruikt om dimensionaal-schaalbare nanostructuren te verschaffen voor onderzoek naar nanostructuur-biologische eenheid interacties. Micro en nanostructurering van materialen zoals keramiek, polymeren, silicon en titanium worden hier gepresenteerd om materialen te verkrijgen met een verbeterde biocompatibiliteit en potentiele bioactiviteit. Het werk hier uitgevoerd was onderdeel van het STW-project NanoSurf, waarin uitgebreide studies zijn uitgevoerd naar de interactie van nanogestructureerde oppervlakken van materialen voor biomedische applicaties met biologische structuren, zowel via *in vitro* als *in vivo* experimenten.

Allereerst is dicrostructurering van keramische materialen met behulp van *tape casting* en *micromolding* bekeken. Vervolgens leverde een nieuwe nanofabricatiemethode voor richels en groeven op biomaterialen een zeer geordend nanoschaalpatroon, schaalbaar in alle ruimtelijke dimensies op oppervlaktes tot 5 cm^2. Om nanostructuren op een biomateriaaloppervlak te genereren werd laser interferentie lithografie gebruikt waarmee eerst patronen werden gedefinieerd in een fotogevoelig polymeer op silicium. Vervolgens werd het patroon overgebracht in silicium met verschillende *reactieve-ionen-ets* (RIE) stappen. Tenslotte werden de oppervlaktestructuren gereproduceerd in polymeren en gebruikt voor *in vitro* studies of alternatief gekopieerd door middel van nanoimprint lithografie (NIL) op titanium van biomedische kwaliteit en geëtst met een geoptimaliseerd chloor-RIE-proces. Nanoroosters met kleinste richel- en groef dimensies in de grootteorde van typisch 75 nm en 150 nm zijn in repectievelijk silicium en biomedisch titanium gereproduceerd. De hier

gepresenteerde parallelle nanopatroneringsmethoden zijn snel, zeer reproduceerbaar en in staat grote gebieden met uniforme patronen tot 5 cm^2 voor celkweek te leveren. Door de aard van het ontwerp van het fabricageproces bestaan er aanzienlijke dimensionele afwijkingen, waarbij vooral de verhouding van de richel en groef belangrijk zijn. We hebben deze afwijkingen gekarakteriseerd en presenteren strategiën om de dimensies te optimaliseren voor een verscheidenheid aan biologische tests die nodig zijn om de nanostructuur-cel interactie hypothese te bezwijzen.

Ten eerste werden de nanogefabriceerde oppervlakken onderzocht op hun interactie met ECM-eiwitten. Gevonden is dat de eiwitadsorbtie in de aanwezigheid van een regelmatige nanostructuur oppervlakte in de meeste gevallen een directe functie van het beschikbare oppervlak is, terwijl ook de oppervlakte chemie een grote rol speelt. Tot slot zijn de nanostructuren gerepliceerd in polystryreenplaatjes en zijn er series van experimenten met osteoblasten uitgevoerd, waarbij karakteristieke reacties van deze cellen op de verschillende oppervlaktestructuren is waargenomen, zoals een verhoogde expressie van bepaalde genen, een uitlijning van de cellichamen op de structuren, en specifieke focale adhesie van de cellen aan de nanostructuur.

Als eindconclusie van dit proefschrift kan worden gesteld dat de set van geoptimaliseerde fabricageroutes die hier zijn gepresenteerd voor het oppervlaktestructureren van biomaterialen op de nanoschaal goedgedefinieerde oppervlakten leveren voor parametrische studies en verder statistisch onderzoek op het gebied van de implantologie.

Acknowledgements

The thesis you are holding in your hand, dear reader, describes results of work I have conducted to obtain a PhD degree in the Mesoscale Chemical Systems group of prof Han Gardeniers. No doubt that this could not be achieved without significant contribution of my fantastic supervisors and colleagues. I would like to express my gratitude to prof. Han Gardeniers for giving me an opportunity to develop myself in his group. I greatly appreciated your direct and precise help and guidance during our discussions. I would like to thank dr Regina Luttge a lot for giving me many, many lessons, being a demanding supervisor and showing me how a grown up and self-standing scientist should function. Especially I would like to thank you for the time you spent on discussion with me, I have learned a lot from it. Dr Louis Winnubst, thank you a lot for the support and expertise, especially at the beginning of my work as PhD student.

My colleagues, the whole MCS group, amazing scientists and people, I have enjoyed the time with you a lot. MCS is a unique creation with many interdisciplinary specialists but also great people for both scientific discussion and quality party time. Great mixture, not so common, and obviously very successful.

Henk van Wolferen from TST group, I am so much grateful for your development and optimization of the LIL technique that is a very important part of this work.

My collaborators dr Walboomers and prof. Jansen from UMC St Radboud in Nijmegen, thank you for the Nanosurf project and for the excellent and fruitful collaboration. Edwin great thanks for all experiments on my surfaces and great contribution to my thesis.

My friends that I have spent most time with Nikolay, David, Wojtek and Piotr, thanks for handling my bad jokes and peculiar attitude. Nikolay and Piotr also thanks for agreeing to be my paranymphs.

Finally, and personally the most important, my family and my girlfriend Laura. ¡Gracias por siempre ayudarme y apoyarme!

Kochani rodzice, gigantyczne dzięki za wszystko, za całą pomoc, inspiracje oraz cierpliwość dla mnie!

Maciej Domański